

RICE UNIVERSITY

**Influence of climate-modulated flooding on
fluvial morphodynamics and stratigraphy**

by

Eric A. Barefoot

A THESIS SUBMITTED
IN PARTIAL FULFILLMENT OF THE
REQUIREMENTS FOR THE DEGREE

Doctor of Philosophy

APPROVED, THESIS COMMITTEE:

Jeffrey A. Nittrouer, Chair
Assistant Professor of Earth,
Environmental and Planetary Sciences

Mark A. Torres
Assistant Professor of Earth,
Environmental and Planetary Sciences

Kirsten L. Siebach
Assistant Professor of Earth,
Environmental and Planetary Sciences

Thomas E. X. Miller
Associate Professor of Ecology and
Evolutionary Biology

Kyle M. Straub
Associate Professor of Earth and
Environmental Sciences
TULANE UNIVERSITY

HOUSTON, TEXAS
APRIL 2021

ABSTRACT

Influence of climate-modulated flooding on
fluvial morphodynamics and stratigraphy

by

Eric A. Barefoot

Contemporary climate change is expected to exacerbate river flooding in the future, but the potential impacts on alluvial landscapes remain ambiguous. There are two main sources of natural observations to bolster this understanding: modern rivers and fluvial stratigraphy. Observations from modern rivers directly connect floods and landscape evolution, but because the data span at maximum a few centuries, the temporal scope is insufficient to constrain the impact of future changes in flood frequency and magnitude. On the other hand, the stratigraphic record is synoptic in scope, but stochastic erosion and deposition render the record incomplete, and thus limit the precision of paleoenvironmental reconstructions.

This dissertation sharpens interpretations of the geologic record by improving the process-based understanding of fluvial morphodynamics influenced by flooding, particularly by focusing on how changes in flooding intensity manifest in alluvial strata. Two main strategies are used. In the first, a stratigraphic study characterizes the signature of enhanced flooding during an abrupt warming episode in the geologic past, and in the second, experiments were conducted whereby a scaled fan delta was subjected to artificial floods while process responses were observed, and the resulting stratigraphy analyzed.

Both the stratigraphic and experimental studies point to the importance of

the balance between lateral and downstream sediment transport. It is shown that extreme flooding destabilizes channel banks, and promotes lateral sediment dispersal and floodplain reworking, whereas a total absence of flooding restricts sediment exchange across channel margins and directs sediment downstream. However, incremental increases in flooding do not always result in enhanced sediment exchange. Moderate amounts of flooding act to stabilize channels rather than destabilize them, because sediment delivered to channel margins during floods builds levees that confine flow and limit lateral sediment dispersal in favor of downstream transport. In this way, climate-modulated changes in flooding alter the spatiotemporal distribution of sediment, which is a crucial control enhancing or diminishing the taphonomic potential of paleoclimate records through time. Thus, levee-construction processes are the lynchpin governing fluvial responses to flooding at the basin scale, and are essential for reconstructing past environmental change as well as characterizing future threats to riparian communities.

Acknowledgments

If ever evidence is needed to show that research is a team effort, let me present to you this document. I owe the successful completion of this thesis to a large and dedicated team, the vital importance of which has been brought into sharp focus over the past year. One-fifth of the time I spend reading, experimenting, analyzing, and writing for this dissertation elapsed during the COVID-19 pandemic. The isolation of this year, the most challenging in my memory, has taught me to cherish the collaboration and fellowship that came so easily before.

This past year, I have mostly worked alone. It is a poor substitute for office 230B that I used to share with Drs. Brandee Carlson, Tian Dong, and Andrew Moodie. Every day, we distracted each other from our work with conversation and friendship, and on Friday afternoons, we descended on Valhalla to hammer out proposals, decide on field plans, or just talk science. No doubt, those casual conversations and “distractions” were the seeds of new ideas and worth their weight in gold.

The central ideas of this dissertation were born in conversation. Quite a few were held while standing on dusty hillsides in western Colorado swatting tiny biting flies. I am deeply grateful for the days I got to spend in the Piceance Basin with my colleagues and friends, Dr. Chenliang Wu, Dr. Brady Foreman, Dr. Rob Mahon, and Sam Zapp, who were a joy to argue with about rocks on the road to an outcrop, or after a cerbeza while the grill fired up. That said, I think the trip to the Piceance I will cherish most will be the one I took with my dad, who is an *excellent* field assistant.

It’s not just in the wilderness that you get good science done though. I miss chatting over morning coffee with Dr. Rob Mahon, who kindly hosted me in a spare room at his house for no less than six months while I ran the experiments that form

the core of this dissertation. Those experiments were conducted at Tulane University, and it is not an understatement to say that this dissertation would not exist without the help and support of my mentor, Dr. Kyle Straub. Kyle let me wreak havoc in his lab for six months, and for that and his mentorship, I am very grateful.

This year, I have learned that every moment to spend with people is a gift, and that as I pass this milestone, I owe a debt of gratitude to an army of my supporters, some of whom I have singled out below.

My gratitude to my advisor, Jeff, runs deep. I have learned so many things from your example and leadership.

My gratitude to my labmates is vast. Brandee, you taught me about strength; Andrew, you taught me about grit; Tian, you taught me how to be joyful; Chen, you taught me about kindness.

My gratitude to my family is profound. You have empowered me to go out and explore, and I hope I have become the son you envisioned.

My gratitude to Patrick grows every day. Because of your love and support, my heart is full.

My gratitude for Valhalla is central to my time at Rice; that's where I made my friends.

My gratitude for my many dear friends is almost too great to express. Without you, I would have gone insane long ago.

I also have a good dog, who never made it easier, but always made it better. 🍃

Thank you all.



Table of Contents

Abstract	ii
Acknowledgments	iv
Table of Contents	ix
Illustrations	xi
Tables	xii
1 Introduction	1
2 Flooding in the Stratigraphic Record	10
2.1 Fluvial response to the PETM	11
2.2 The Wasatch Formation, Piceance Basin, USA	13
2.3 Paleohydraulic reconstruction techniques	16
2.4 Results	19
2.5 Channel mobility from intensified flooding	19
2.6 Summary	23
3 Non-monotonic Fluvial Response to Changes in Flooding Intensity	24
3.1 Theoretical background and approach	25
3.2 Methods	29
3.2.1 Experimental design	29
3.2.2 Data collected	32
3.2.3 Channel mobility	34
3.2.4 Sediment dispersal	35
3.2.5 Delta-floodplain morphology	38
3.3 Results	41
3.3.1 Channel mobility	41
3.3.2 Sediment dispersal	41
3.3.3 Channel and delta floodplain morphology	48
3.3.4 Levee breach abundance	49

3.4	Floods and basin-scale morphodynamics	50
3.5	Summary	56
4	Paleoclimate Bias due to Transitions in Flooding	58
4.1	Reconstructing climate from strata	59
4.2	Methods	62
4.2.1	Experimental design	62
4.2.2	Data collected	64
4.2.3	Quantifying stratigraphic bias	65
4.2.4	Quantifying sedimentation statistics and autogenic dynamics	67
4.3	Results	68
4.3.1	Stratigraphic preservation bias	68
4.3.2	Sedimentation statistics	71
4.3.3	Surface roughness and sediment dispersal	73
4.4	Discussion	76
4.4.1	Hysteresis in fluvial response	78
4.4.2	Climate event duration and fluvial disequilibrium	80
4.4.3	Stratigraphic bias during climate events	81
4.4.4	Implications for interpreting Eocene hyperthermal events	82
4.5	Summary	83
5	Conclusion	86
	Bibliography	90
A	Statistical Models	102
A.1	Flooding in the Stratigraphic Record	102
A.1.1	Kruskal-Wallis test	102
A.1.2	χ^2 test for proportions	103
A.2	Non-monotonic Fluvial Response to Changes in Flooding Intensity	104
A.2.1	Restricted maximum likelihood estimation for channel mobility	104
A.2.2	Evaluating differences in sediment dispersal patterns	105

A.2.3	Evaluating differences in channel abundance in stratigraphy	106
A.2.4	Evaluating differences in floodplain relief	107
A.2.5	Evaluating differences in floodplain slope	108
A.2.6	Evaluating differences in shoreline rugosity	108
A.2.7	Evaluating differences in channel width	109
A.2.8	Evaluating differences in channel depth	110
A.2.9	Evaluating differences in channel slope	111
A.2.10	Evaluating differences in levee breach abundance	111
A.3	Paleoclimate Bias due to Transitions in Flooding	112
A.3.1	Evaluating bias in preserved transition duration	112
A.3.2	Evaluating the average sediment accumulation rate during transitions	114
A.3.3	Evaluating the variability in sediment accumulation rate during transitions	115
A.3.4	Evaluating the impact of sedimentation rate and steadiness on preservation bias	116

Illustrations

2.1	Map of study location: Piceance Basin, Colorado, USA	14
2.2	Example paleohydraulic interpretations from Wasatch Formation outcrops	18
2.3	Estimates of key paleohydraulic parameters before, during, and after the PETM in the Wasatch Formation	21
3.1	Example null model for fluvial system evolution across a gradient of flooding intensity	27
3.2	Diagram of experimental apparatus	29
3.3	Flood pulse design	31
3.4	Channel mask construction method	33
3.5	Method for extracting channel geometries from topographic data	38
3.6	Extracting floodplain relief using detrended topography	40
3.7	Estimates of normalized channel overlap decay	42
3.8	Isopach maps and stratigraphic cuts for each level of flooding intensity	43
3.9	Channel abundance maps and stratigraphic sections for each level of flooding intensity	45
3.10	Channel and floodplain grain size distributions; distribution in the strata	46
3.11	Stratigraphic completeness for each level of flooding intensity	47
3.12	Channel geometry at each level of flooding intensity	48
3.13	Non-monotonic scaling of delta morphology with flooding intensity	49
3.14	Levee breach abundance as a function of flood intensity	49
3.15	Mechanics of channel evolution under low- and high-intensity flooding	52
4.1	Experimental design to examine effect of transitions in flood intensity	62
4.2	Example of uneven temporal sampling in stratigraphy	66
4.3	Flooding transitions reconstructed from core ensembles	69
4.4	Bias when reconstructing the duration flooding transitions	70
4.5	Mean accumulation rate during flooding transitions	71

4.6	Standard deviation of accumulation rate during flooding transitions .	71
4.7	Trends in preservation bias with the mean sedimentation rate	72
4.8	Delta topset roughness throughout experiment	73
4.9	Surface roughness following transitions, relative to equilibrium values	74
4.10	Paired maps of detrended topography and isopachs of post-transition deposition	75
4.11	Areal extent and thickness variability of sedimentation after flooding transitions	76
4.12	Illustration of sediment repaving strategies following a flooding transi- tion	78

Tables

2.1	Paleohydraulic reconstruction estimates comprising the PETM; estimated from the Wasatch Formation, Piceance Basin	20
3.1	Delta Basin run parameters—gradient of flooding intensity	30
3.2	Modeled estimates for observed delta parameters	50
4.1	Delta Basin run parameters—transitions in flood intensity	64
A.1	Estimated parameters for channel mobility	104
A.2	Posterior parameter estimates for Sadler exponent	106
A.3	Posterior parameter estimates for channel abundance	107
A.4	Posterior parameter estimates for floodplain relief	107
A.5	Posterior parameter estimates for floodplain slope	108
A.6	Posterior parameter estimates for shoreline rugosity	109
A.7	Posterior parameter estimates for channel width	110
A.8	Posterior parameter estimates for channel depth	110
A.9	Posterior parameter estimates for channel slope	111
A.10	Posterior parameter estimates for levee breach abundance	112
A.11	Posterior parameter estimates for preservation bias	113
A.12	Posterior parameter estimates for average sediment accumulation rate	115
A.13	Posterior parameter estimates for the standard deviation of sediment accumulation rate	116
A.14	Posterior parameter estimates for the standard deviation of sediment accumulation rate	118

Chapter 1

Introduction

All rivers flood. Equal parts feast and famine, floods are responsible for water, sediment, and nutrient exchange between streams and riparian ecosystems (Mertes 1997), providing rich ecological benefits (Junk et al. 1989). On the other hand, floods are destructive and costly, accounting for approximately 40% of economic damage from natural disasters, and killing or displacing millions of people in the latter half of the 20th century alone (Pielke and Downton 2000).

Broadly speaking, floods are best understood in a probabilistic sense. The notion of a 10-year, 100-year, or 500-year flood zone is underpinned by the fact that while floods do not recur periodically, the odds that a flood of a given magnitude will occur in a given year follows a predictable scaling (e.g. Langbein 1949). Central to flood hazard planning, this idea suffers from two key shortcomings (Kirby and Moss 1987). The first is that historical records of river discharge only span at maximum a few centuries (Gilvear and Winterbottom 1992). Since discharge statistics often follow power-law scaling, this short observation window is insufficient to correctly characterize the odds of extreme events (Smith et al. 2018).

The second issue is that contemporary climate change is projected to affect the global hydrological cycle via changes to atmospheric circulation (e.g. Trenberth 2011). The simplest version of this prediction states that rising global temperatures will increase the saturation vapor pressure of air in the troposphere, thus promoting evaporation in arid regions and intensifying precipitation in humid regions (Held and Soden 2006). This general *wet-gets-wetter, dry-gets-drier* trend of regional precipitation response is borne out in ensemble global circulation models (Dai 2006), and in this condition, the statistics of river discharge will also change in the future, limiting

the predictive power of existing observations for constraining flood hazard.

Atmospheric processes are not the only factor governing future flood risk. Topography also controls flood hazard across the river network (O'Connor and Costa 2004), and regional impacts will differ depending on context. For example, powerful storms that generate intense rainfall can cause local flooding (Smith et al. 2001), but distributed rainfall over a large catchment can accumulate through the river network to cause catastrophic flooding downstream (Quinn et al. 2019). Nonetheless, predictions of intensified storms (Trenberth et al. 2003), shifting monsoons (Wang and Ding 2006), and the loss of snowpack (Gergel et al. 2017) imply that in many regions of the world, flooding is likely to intensify in the future (Singh et al. 2013).

Flood hazard projections in the long term are further complicated by the fact that rivers are dynamic landscape features that incise, shoal, widen, and narrow to adjust channel dimensions and produce an equilibrium geometry (Parker 1978). Furthermore, rivers migrate laterally across the landscape by eroding cut banks and building point bars (Hickin and Nanson 1984), and avulse by abruptly jumping and relocating channels to new locations on the floodplain (Allen 1978; Slingerland and Smith 2004). This behavior threatens the sustainability of riparian communities, since bank erosion can undermine foundations of critical infrastructure, and avulsion can threaten settlements far from the river banks (Haque and Zaman 1989).

River relocation and changes in river channel geometry also affect the capacity of the channel to convey water, which in turn modifies flood statistics. To accurately constrain future flood risk over the the coming decades to centuries, a theoretical description of river response to a change in the distribution of runoff events is needed. However, such a description is mathematically elusive (Pickup and Rieger 1979), because alluvial systems are complex, and comprise a nested hierarchy of processes that act on a wide range of spatial and temporal scales (Paola et al. 2018; Ganti et al.

2020).

Instead, the prevailing strategy is to summarize the hydrograph by a single, characteristic steady discharge. It is asserted that given enough time, the characteristic discharge broadly produces the same equilibrium landscape features as a variable hydrograph (Howard 1982). Wolman and Miller (1960) is a classic example of this approach, demonstrating that as sediment transport events increase in magnitude, their frequency diminishes such that the product of frequency and magnitude achieves a maximum efficacy at some intermediate value. This led Wolman and Miller to assert that the maximum frequency-magnitude product determines the average characteristics of the fluvial channel, especially its equilibrium dimensions. Called the *effective discharge*, this formulation of the representative steady discharge is one of several approaches to characterizing the long-term morphodynamic evolution of river channels (Blom et al. 2017).

The concept of an equivalent steady discharge is applied in tandem with an *intermittency* factor, such that the effective discharge is only active for a brief time (Paola et al. 1992). While this approach reproduces many of the broad features produced by landscape evolution, it is also clear that any given formulation for a characteristic steady discharge reproduces some aspects of the fluvial system, while failing to capture others (Prins and Vries 1971). For example, floods are required to generate certain delta-lobe switching dynamics (Ganti et al. 2016). Flooding also enhances channel mobility relative to an equivalent steady discharge (Esposito et al. 2018) and variable hydrographs produce unique bedform stratigraphy (Leary and Ganti 2020). These examples serve to show that collapsing the integrated history of flow to a single characteristic value fundamentally oversimplifies the impact of variable discharge on the landscape form (Prins 1969; Pickup and Rieger 1979).

Efforts to extend the equivalent steady discharge to explicitly encompass vari-

able flow into predictions of equilibrium channel geometry (Blom et al. 2017) and landscape evolution (Naito and Parker 2019), however, are hindered by a lack of observations to validate the predictions and guide future modeling. There are three main sources of data that can be used for this purpose: (1) observations of modern rivers, (2) stratigraphic evidence, and (3) sedimentary experiments. Using observations from modern rivers, morphodynamics can be characterized and compared to theory. If the goal is to constrain fluvial evolution in engineered channels over decadal time-scales, observations from modern rivers may suffice (Blom et al. 2017). However, observations of modern rivers span only a few centuries (Kirby and Moss 1987; Gilvear and Winterbottom 1992), and are inadequate for long-term projections of climate change, because they do not integrate over the full range of response timescales for alluvial landscapes (Howard 1982). To overcome this, channel dynamics can be reconstructed through time by examining deposits that record fluvial dynamics during past episodes of climate change (Ethridge and Schumm 1977; Foreman et al. 2012; Trampus et al. 2014; Lynds et al. 2014). Interpretations of the stratigraphic record, however, are hindered by difficulty constraining boundary conditions with precision (Trampus et al. 2017), and the fragmentary nature of the strata itself (Sadler 1981). Linking these two temporal scales, sedimentary experiments provide an analogue for sedimentary systems (Paola et al. 2009), and support hypothesis testing based on observations from both modern fluvial environments and the stratigraphic record.

The stratigraphic record is particularly important in the context of forecasting, because contemporary climate change is not a singular event in Earth history, and valuable insights can be gleaned from similar episodes in the geologic past, where large-scale CO₂ release into the atmosphere was paired with rapid atmospheric warming (Zachos et al. 2001). Sedimentary rocks deposited during these periods record environmental conditions through both sedimentary structures (Foreman et al. 2012; Kraus et al. 2015), as well as biogeochemical markers, or proxies, hosted in the sed-

iments (e.g. Zachos et al. 1993). These archives form the backbone of paleoenvironmental reconstructions older than ~ 1 -2 million years before present, when more readily datable records like ice cores are unavailable.

Throughout this dissertation, the Paleocene-Eocene Thermal Maximum (PETM; ~ 56 Ma) is used as an example of these extreme climate events. Widely considered to be one of the best geologic analogues for contemporary climate warming (McInerney and Wing 2011), the PETM is the most severe climate perturbation known in the Cenozoic Era (Zachos et al. 2008). Identified in strata by a negative carbon isotope excursion (CIE: Kennett and Stott 1991), the PETM typically coincides with drastic changes in sedimentology that are interpreted to be the result of enhanced hydrological cycling that impacted landscape dynamics (for a detailed description, see § 2.1). However, key aspects of the PETM remain murky. For example, estimates of the total duration of the event lack precision (Kirtland Turner 2018), and sedimentological evidence can be ambiguous, such that multiple candidate mechanisms can explain the observed fluvial response to climate (Foreman 2014).

The stratigraphic record is, moreover, a notoriously unfaithful recorder of paleoclimate conditions (Straub et al. 2020; Sadler 1981). Sedimentary systems are characterized by unsteady sedimentation because of autogenic landscape dynamics, that is, localized patterns of sediment transport that arise simply due to the interaction of landscape elements and water flow (e.g. Hajek and Straub 2017). When the locus of morphodynamic activity is in a given geographic location, sediment can accumulate, but when the locus shifts away, no deposition can occur during the hiatus, and temporal gaps—i.e. disconformities—enter the stratigraphic record (Sadler 1981; Tipper 2015), and obscure the record of climate events (Trampush and Hajek 2017). These uncertainties make it challenging to connect environmental conditions during the PETM with contemporary change, and limit the usefulness of the PETM as an analogue.

A clear description of surface processes due to variable flow is a critical missing link needed to clarify reconstructions of the geologic past, understand present-day landscape evolution, and forecast impacts of future change. The central goal of this dissertation is to advance this mission by providing new interpretations for fluvial landscape response to the PETM, characterizing surface process changes due to variable flow, and identifying how changing surface processes can modulate the resolution of the stratigraphic record.

In Chapter 2, I investigate the impact of enhanced flooding on fluvial morphodynamics during the PETM. Intensified storms and flooding during the PETM are thought to have resulted in mass mobilization of sediment from hillslopes (Lyons et al. 2019) that propagated downstream, impacting fluvial dynamics (Pujalte et al. 2015; Chen et al. 2018), and eventually flushing into terminal marine basins (Slotnick et al. 2012), termed a *global system-clearing event* (Foreman et al. 2012). The evidence for this consensus revolves on observations of high accumulation rates of terrigenous mud in marginal marine strata (John et al. 2008), and increased concentration of sand in terrestrial fluvial strata (Foreman 2014). Theoretical fluvial basin-filling models predict that when sediment supply increases in a fluvial sedimentary system, deposition of sand and mud is displaced in the down-dip direction (Paola et al. 1992). This assertion implies that if future global warming also intensifies storms and monsoons, hillslope sediment stripping and fluvial perturbations might occur in many regions of the world: a dire prediction. In this chapter, I show that the assertion of enhanced sediment flux is not supported by available data, and that observed sedimentological patterns (proximal accumulation of sand, and distal accumulation of mud) can be explained by changes in flooding intensity alone. As a result, this chapter suggests that while the impacts on river floodplains may have been severe during the PETM, enhanced sediment supply need not be the cause of the observed landscape response during the PETM. Moreover, these findings also highlight that our understanding of

landscape response to changes in flooding is incomplete.

Detailed mechanisms of landscape change are challenging to resolve in the stratigraphic record, so in Chapters 3 and 4, I employ a complementary approach, where interpretations from the strata are used to motivate sedimentary experiments, and test hypotheses about fluvial landscape evolution as a result of flooding. Using a characteristic steady discharge to describe channel dynamics implies that changes in channel mobility, sediment dispersal, and landscape morphology will be monotonic with incremental increases in flooding intensity (e.g. Blom et al. 2017; Naito and Parker 2019). In Chapter 3, I test theoretical predictions of landscape response across a gradient of flooding conditions using experimental fan deltas. The deltas evolved in response to three levels of flooding intensity, while the equivalent steady discharge was the same for each delta. Observations of channel mobility, sediment dispersal, and landscape morphology show a non-monotonic trend as a function of flooding intensity, in contradiction with expectations. I show that for these experiments, levee-building processes generates non-monotonicity by stabilizing channels at moderate flooding intensities, but destabilizing channels when flooding is either intense or absent. This counterintuitive result suggests that in the stratigraphic record, increased flooding may lead to diverging landscape responses, and implies that future change may depend on the current system state.

Chapter 3 compares between three discrete stages of an experiment, but during a climate event like the PETM, flooding conditions transition from one state to another over the duration of the event. For example, as is described in Chapter 2, the onset of the PETM in the Piceance Basin is distinguished by an abrupt shift from low-intensity to high-intensity flooding. In Chapter 4, I explore this process, focusing on two aspects of flooding transitions: (1) the *abruptness* of the transition, and (2) the *sign* of the transition, where transitions from low to high-intensity flooding are termed *positive* and high-to-low transitions are termed *negative*.

Using the same apparatus as in Chapter 3, I conducted a fan delta experiment that toggled between two levels of flooding intensity, and where the duration of each transition was controlled. The evolution of the surface topography during and after each transition was documented, as were sediment dispersal patterns. In this chapter, I show that following transitions, landscapes are in disequilibrium with the flood regime, and that abrupt transitions induce more severe disequilibrium than gradual ones.

To reestablish equilibrium, the sedimentary system must deposit and erode sediment to reproduce equilibrium topography. There are two end-member strategies. One employs erosion to *rework* the surface and replace it with new sediment, thus establishing equilibrium topography. The other end-member relies purely on deposition to *repave* the surface without any incision. In this chapter, I show that because repaving is the dominant strategy in this experimental apparatus, the recovery pathway exhibits hysteresis. Reestablishing equilibrium following positive transitions requires a different spatial allocation of sediment than after negative transitions.

In Chapter 4, I further investigate how the changing dispersal patterns of sediment during flooding transitions affect the preservation of biogeochemical proxies in the strata. Since the distribution of sediment and hiatuses in the sedimentary record controls the fidelity of paleoclimate proxy records in the strata (Foreman and Straub 2017; Trampush and Hajek 2017), it is reasonable to expect that changing sediment dispersal due to transitions in flooding is bound to impact the fidelity of paleoclimate records. I examine the practical resolution of stratigraphic sections taken from the experimental stratigraphy and demonstrate that due to sediment localization during negative (high-to-low) transitions, the perceived duration of the climate event is compressed relative to the true duration. In contrast, during positive transitions, sediment is widely distributed, so the perceived duration of climate events is dilated.

This dissertation characterizes the impact of climate-modulated changes in hydrograph variability on fluvial landscape evolution, and its signature in the stratigraphic record via analysis of field outcrops and sedimentary experiments. These observations and insights lay the groundwork for new advances in understanding the full complexity of landscape evolution under variable flow. Further, by establishing the resulting impact on the fidelity of the stratigraphic record, this dissertation provides a framework for quantifying uncertainty and sampling bias in paleoclimate data. These contributions illuminate Earth history during abrupt climate change, and also sharpen predictions for future climate change.

Chapter 2

Flooding in the Stratigraphic Record

Abstract

The Paleocene-Eocene Thermal Maximum (PETM) was the most extreme example of an abrupt climate perturbation in the Cenozoic, and is widely discussed as the best past analogue for contemporary climate change. Anomalous accumulation of terrigenous mud in marginal shelf environments and concentration of sand in terrestrial deposits during the PETM are both used to infer an increase in fluvial sediment flux. A corresponding increase in runoff or river slope is required to transport this additional sediment. However, in many locations, evidence for changes in fluvial slope is weak or missing entirely, and geochemical proxies and climate models indicate that while runoff variability may have increased, mean annual precipitation was unaffected. Here we explore whether changes in river morphodynamics under variable-discharge conditions could have contributed to increased fluvial sand concentration during the PETM. Using field observations, we reconstructed channel paleohydraulics, paleo-mobility, and avulsion behavior for the Wasatch Formation (Paleocene-Eocene, Piceance Basin, Colorado, USA). Our data provide no evidence for changes in fluvial slope or channel depths during the PETM, and moreover no evidence for enhanced sediment discharge. Our data do show evidence of increased fluvial bar reworking and advection of sediment to the floodplain during channel avulsion. These results are consistent with experimental studies showing that sediment storage in alluvial basins is sensitive to discharge variability. High discharge variability increases channel mobility, which results in floodplain reworking that retains coarse sediment while remobilizing and exporting fine sediment through the alluvial system. This mech-

anism explains net export of fine sediment to continental shelves without invoking sustained increases in sediment and water discharge.

2.1 Fluvial response to the PETM

Global climate change is predicted to impact the hydrological cycle, threatening communities and infrastructure situated on river corridors (e.g Dankers and Feyen 2008). The hazards posed by modern climate change can be understood by reconstructing hydrological conditions in past climate-change events using sedimentological and biogeochemical proxies (e.g. Slotnick et al. 2012). The Paleocene Eocene Thermal Maximum (PETM) is the most severe climate perturbation known in the Cenozoic Era (Zachos et al. 2008), and is considered one of the best geologic analogues for contemporary climate warming (McInerney and Wing 2011). First identified in marine isotope records, the PETM is marked by a negative 2–5‰ carbon isotope excursion (CIE) in marine $\delta^{13}\text{C}$ records (Kennett and Stott 1991; Zachos et al. 2001). Requiring a sharp increase in the carbon content of the atmosphere, the CIE is connected to the rapid injection of ^{13}C -depleted carbon followed by a recovery period where isotopically light carbon was recycled from surface carbon reservoirs (Dickens et al. 1995). Substantial global warming is associated with the carbon injection, where temperatures increased by 5–8°C in as little as 5 ka (Zachos et al. 2001; Kirtland Turner 2018). During the ~200 ka recovery, temperatures decreased from peak values, settling on a new, higher mean annual temperature (Zachos et al. 2001). The climatic perturbation and carbon isotope signature are attributed to a diverse suite of causes, including the destabilization of methane hydrates on the continental shelves (Dickens et al. 1995), eruption of large igneous provinces (Thomas and Shackleton 1996), and enhanced soil carbon respiration in thawing permafrost (DeConto et al. 2012), among others.

Regardless of the cause, the climate implications of the PETM are significant.

The PETM is the first and most prominent hyperthermal episode of the early Eocene, a period distinguished by warm temperatures and elevated carbon content in the atmosphere (Zachos et al. 2001). Based on paleoclimate data and global circulation modeling results, it is suggested that ice-free conditions and warmer temperatures during the early Eocene generated a shallower latitudinal temperature gradient (Bijl et al. 2009). Against this backdrop of an already warmer climate, the PETM aberration altered hydrology (Carmichael et al. 2017), sedimentology (John et al. 2008), and chemical cycling (Ravizza et al. 2001), significantly impacting global ecosystems. The impact of the PETM on the biosphere is observed in the sudden evolution of so-called “excursion taxa” in the marine environment (Stassen et al. 2012; Kelly et al. 1998), dwarfing of land animals (D’Ambrosia et al. 2017; Smith et al. 2009), and vegetation community overturn (Wing and Currano 2013).

In tandem with ecological changes, the PETM often coincides with drastic changes in sedimentology that are interpreted to be the result of significant climate-driven changes to landscape dynamics. For example, large volumes of terrigenous clay in marginal marine PETM sections (e.g. John et al. 2008) are attributed to elevated sediment flux from continents as a result of (1) enhanced hillslope weathering and mobilization (Lyons et al. 2019), and/or (2) large-scale sediment-transport “system-clearing” events (Jerolmack and Paola 2010; Foreman et al. 2012). Both scenarios necessitate enhanced sediment transport capacity to drive sediment flux.

Studies from terrestrial basins assert that the signature of enhanced transport capacity and hillslope supply is evident in fluvial PETM deposits, which are generally channel-dominated and enriched in sand relative to surrounding Paleocene and Eocene strata (e.g. Pujalte et al. 2015). In particular, paleo-channel depth (Foreman et al. 2012) and slope reconstructions (Chen et al. 2018), are interpreted to indicate that channel-forming water discharge increased because of enhanced intra-annual runoff variability. However, the paleohydraulic techniques used to estimate these parameters

carry substantial uncertainties (Trampush et al., 2014), and the connection between enhanced runoff variability during the PETM and an overall increase in sediment transport capacity or supply is unclear.

Moreover, even without adjustments in sediment supply, water discharge variability itself can have significant impacts on fluvial morphodynamics and sediment storage in alluvial deposits (Leary and Ganti 2020). For example, Esposito et al. (2018) showed experimentally that intense flooding caused channels to migrate and avulse rapidly, as compared to channels that were supplied the same volume of water and sediment at a constant rate. High channel mobility led to floodplain reworking, and resulted in preferential preservation of channel facies in the strata. In this way, changes in time-averaged water and sediment flux are not needed to affect basin architecture, and if evidence for enhanced mobility exists in the absence of change in channel geometry, a change in sediment flux cannot be inferred.

Here, we evaluate the relative merit of two hypotheses. The null hypothesis is that enhanced runoff variability accelerated channel mobility during the PETM, without a concomitant increase in sediment supply. The alternative is that enhanced sediment supply combined with enhanced runoff variability is responsible for observed alluvial stacking patterns during the PETM. Using the example of the Piceance Basin, USA, we collect the evidence required to falsify and reject the null hypothesis, including by estimating of paleochannel depth and slope, estimating relative changes in channel mobility, and characterizing the nature of avulsions.

2.2 The Wasatch Formation, Piceance Basin, USA

The Wasatch Formation (Paleocene-Eocene, Piceance Basin Colorado, USA; Figure 2.1) is a more than 500 m-thick conformable succession of fluvial sediments within

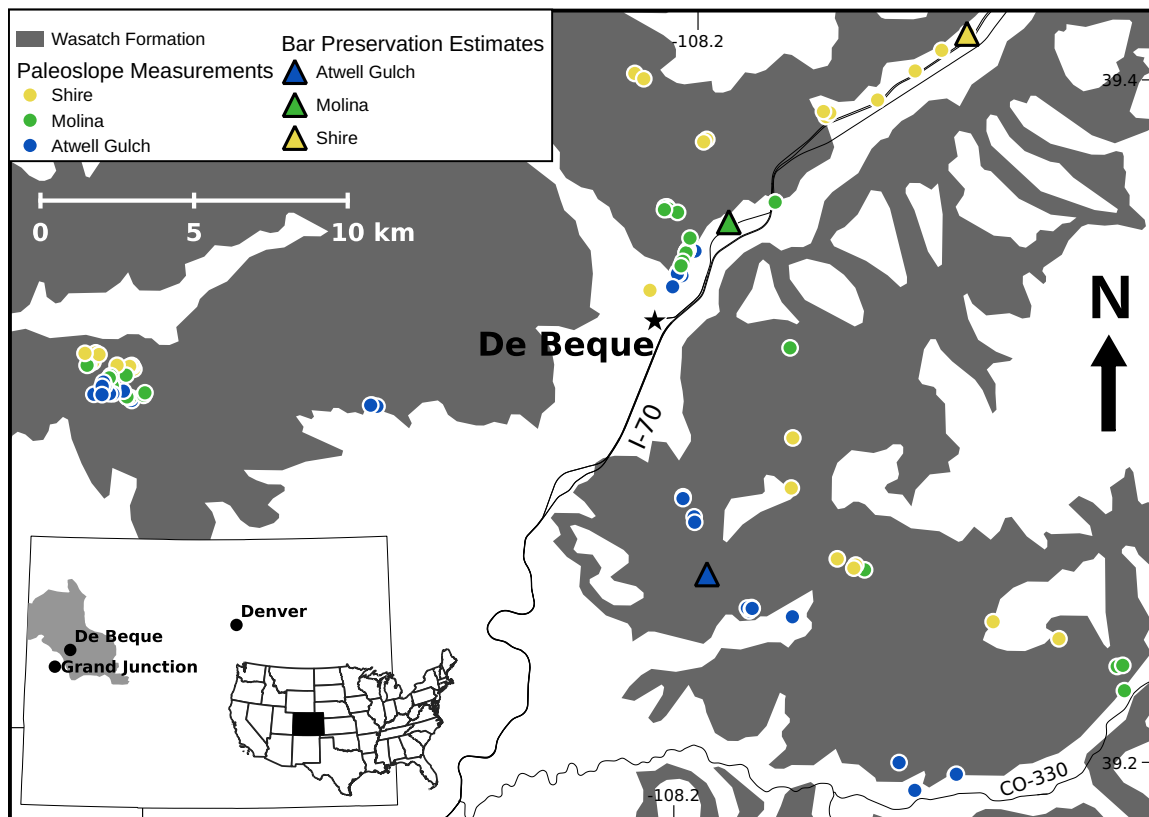


Figure 2.1: The outcropping extent of the Wasatch Formation is shaded; unshaded regions are surrounding Paleocene and Eocene strata. Locations of outcrops that were analyzed for new paleodepth and paleoslope estimates are indicated by circles. Bar preservation estimates were collected from outcrops indicated by triangles.

which the PETM CIE has been shown to coincide with an abrupt increase in sand content and channel amalgamation (Foreman et al. 2012). This PETM interval is found in the Molina Member, which comprises interconnected, sheet-like amalgamated sand bodies with relatively thin intervening layers of floodplain mud (~40% channel). In contrast, the underlying Atwell Gulch and overlying Shire Members of the Wasatch consist predominantly of muddy floodplain paleosols encasing isolated channel sand bodies (~20% channel; Donnell 1969). Accumulating in an active Laramide basin, the Wasatch Formation was within 100 km of the uplifting sediment source, which was consistent throughout deposition (Johnson and Flores 2003; Foreman et al. 2012). Foreman et al. (2012) observed distinctive upper-stage plane bed structures in the Molina Member that are consistent with evidence from modern and ancient

ephemeral river systems characterized by intensely seasonal runoff (Plink-Björklund 2015; Fielding et al. 2018). Foreman et al. (2012) also report deeper and wider channels in the Molina Member, which are interpreted as a fluvial response to enhanced monsoonal precipitation. Paleobotanical evidence for vegetation-community overturn in the Bighorn Basin (Wing and Currano 2013), and sedimentological interpretations of coeval strata from the neighboring Uinta Basin (Birgenheier et al. 2020), also support a regional increase in runoff seasonality that is interpreted to have enhanced sediment flux across the region (Foreman et al. 2012).

Other lines of evidence suggest that the increase in runoff seasonality was not coupled to a change in regional mean annual runoff. Climate model simulations predict overall drying conditions across the North American Mountain West during the PETM (Carmichael et al. 2017), and paleosol records in the Piceance Basin (Erhardt 2005) and nearby Bighorn Basin (Kraus and Riggins 2007) suggest that, regional mean annual precipitation may have decreased during the PETM, but this signal is not readily distinguished from a change in precipitation seasonality, in isolation.

These characteristics of the Piceance Basin make for an opportunity to test the hypotheses outlined above. In particular, because annualized runoff was more or less constant during the PETM, a change in sediment supply would, by necessity, decrease the water-to-sediment ratio, and require enhanced sediment transport capacity. Without changes to annualized runoff, the only way to increase sediment transport capacity is by adjusting fluvial slope (e.g. Paola 2000). Thus, in this basin, a change in fluvial slope would be diagnostic of changing sediment supply.

2.3 Paleohydraulic reconstruction techniques

Estimates of paleo-flow depth through the Wasatch Formation were obtained by measuring the relief on fully preserved fluvial barforms and channel fill structures. Laterally migrating channels accrete sediment on the inner bank of meander bends, which are recognized as stacked clinothem structures (following Ethridge and Schumm 1977). When channels are abandoned by avulsion, sediment fills the resulting topographic low. Sediment fill and clinothems may be measured to assess the bankfull geometry of the alluvial channel by measuring the thickness of these deposits (Mohrig et al. 2000). For this study, 114 measurements of paleo-flow depth were collected using measuring tape across all three Members of the Wasatch Formation. Each measurement comprises a single bar clinothem or channel fill structure, and any given outcrop exposure may possess several individual locations for flow depth measurements. We were careful to select barform features that permitted unambiguous interpretation of the maximum relief. Channel bed deposits at the toes of bar clinothems were also identified, and interpreted as thalweg deposits. Samples were collected from these deposits, and median grain size was measured using a hand lens and standard grain size card.

Trampus et al. (2014) present a model to connect fluvial slope with estimates of bankfull depth and bedload grain size from a dataset comprising over 400 modern rivers. They show that bankfull flow depth and median bed material grain size predict fluvial slope as:

$$\log S = \alpha_0 + \alpha_1 \log D_{50} + \alpha_2 \log H_{bf}, \quad (2.1)$$

where S is the slope, D_{50} is the median bed material grain size, H_{bf} is the bankfull flow depth, and α_0 , α_1 , and α_2 are constants with associated uncertainty; values given in Trampus et al. (2014). Paleo-flow depths from bar clinofolds were combined with collocated measurements of bed-material sediment size to estimate paleoslope via

Equation 2.1.

To quantify the effect of short-term runoff variability on paleochannel mobility, avulsion style and bar preservation were estimated throughout the Wasatch Formation. The basal contact of a fluvial sand body represents an avulsion event that is either preceded abruptly (without crevasse splays) or transitionally (with splays) (Jones and Hajek 2007). Transitional-style avulsions in an alluvial basin indicate more active crevassing in the channel-floodplain system (Hajek and Edmonds 2014). In contrast, stratigraphically abrupt avulsions indicate less active crevassing. We classified avulsions from field observations in all three Members of the Wasatch Formation using criteria in Jones and Hajek (2007).

To reconstruct channel mobility, drone imagery was collected for three outcrops in the Piceance Basin. Bar preservation was quantified, because the relative abundance of poorly preserved or truncated bars reflects the channel mobility relative to the subsidence rate (Chamberlin and Hajek 2019). In this framework, a bar is recognized as “fully preserved” if it has visible clinoform sets with bar-top rollover and hosts upper-bar facies. Partially-preserved or poorly preserved bars lack one or more of these features, but lower-bar facies can still be recognized (Chamberlin and Hajek 2019). Photogrammetry was used to construct 3D digital models of the outcrop surface, and bar clinoforms were mapped on the 3D digital outcrops. Barforms were then classified within channel belts as either fully preserved, partially preserved, or truncated (example interpretations in Figure 2.2).

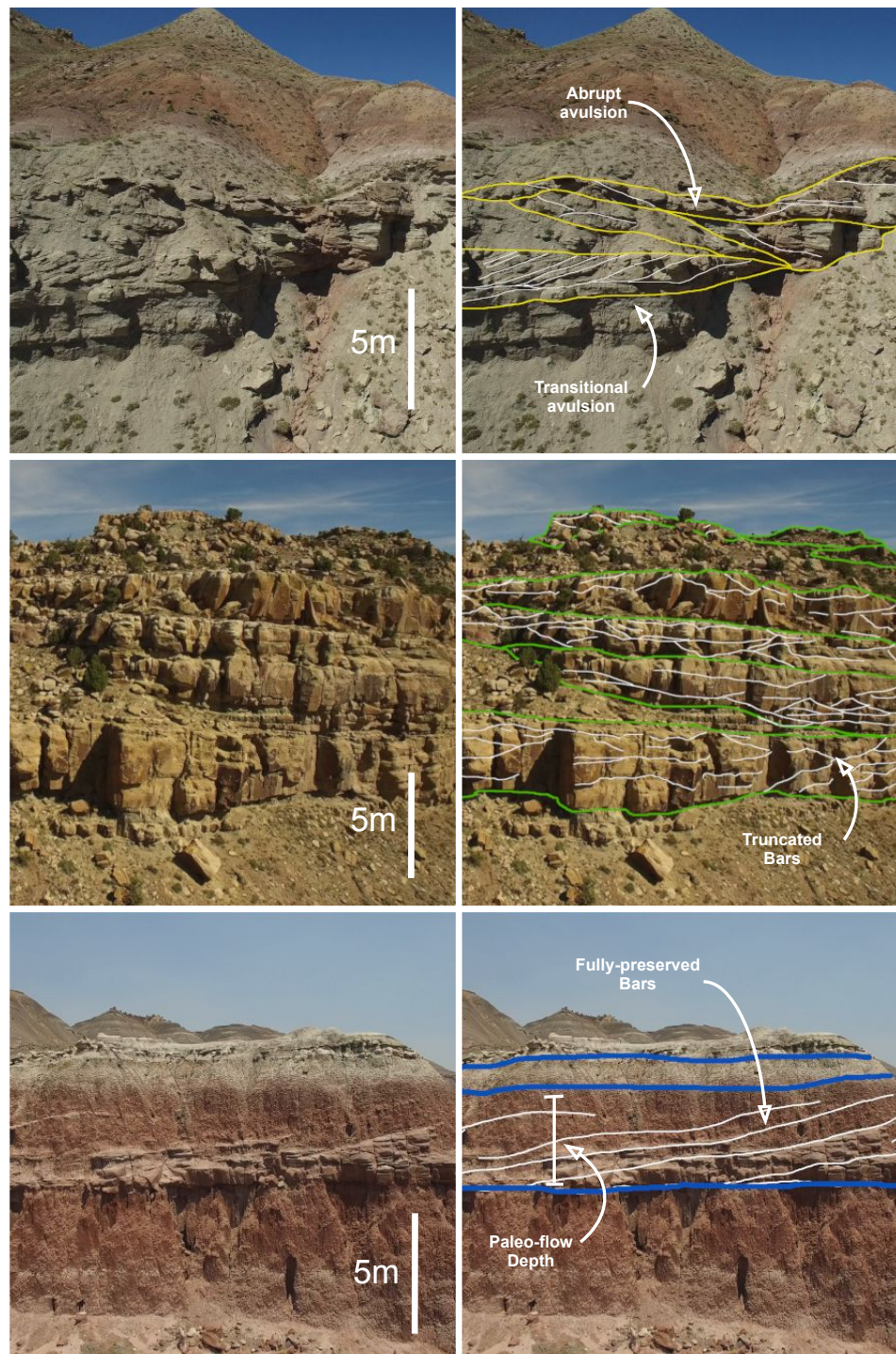


Figure 2.2: Example outcrops showing key sedimentological features in each Member of the Wasatch Formation. Colored lines indicate high-order bounding surfaces between channel stories, whereas the white lines in each photograph indicate bar faces and scour surfaces. Annotations exemplify measurements that were taken for this study.

2.4 Results

The data indicate that channel grain size and paleoflow depths are statistically indistinguishable throughout the Wasatch Formation at a 95% confidence level (using a Kruskal–Wallis ANOVA, see Table 2.1 and Figure 2.3a). Consequently, estimates of paleoslope in the Piceance Basin also indicate no difference between the Molina Member and the bounding Members at a 95% confidence level (Figure 2.3b). Together, these results demonstrate that within the resolution of currently available paleohydraulic methods (Trampush et al. 2014), rivers were not likely to be substantially steeper during the PETM (Molina) as compared to before (Atwell Gulch) or after (Shire). Bar clinoform mapping shows that 11.7% of barforms in the Molina Member are fully preserved, whereas in the Atwell Gulch and Shire Members, 33% and 40% of barforms are fully preserved, respectively (Figure 2.3). A χ^2 test shows that there are significantly fewer fully preserved barforms in the Molina Member, indicating that barforms in the Molina Member crosscut each other within channel belts more frequently than in either the Shire or Atwell Gulch Members (Table 2.1).

Our data also indicate that avulsion style changed during Molina time. Stratigraphically transitional avulsions were more abundant than abrupt avulsions in the Molina Member, as compared to the Shire and Atwell Gulch Members. This indicates that avulsions were more likely to occur via progradation and channel building by crevasse splays, rather than by incision into the floodplain (Hajek and Edmonds 2014).

2.5 Channel mobility from intensified flooding

The preponderance of truncated and partially preserved fluvial bar deposits observed in the Molina Member indicates enhanced fluvial reworking by mobile channels during

Table 2.1: Data for Wasatch Formation in the Piceance Basin. Included for each Member of the Formation are paleoflow depths measured from barforms, paleoslopes, bed material grain size, the proportion of fully preserved bars, the prevalence of transitional avulsions, \pm the associated standard deviation for each. The second part of the table indicates significance values for Kruskal–Wallis ANOVA comparing flow depths and slope in different Members of the Wasatch Formation, as well as results from a χ^2 test for the proportion of fully preserved bars and abundance of avulsion styles.

Formation	Depth (m) $\pm\sigma$	Slope (m/m) $\pm\sigma$	Bedload Grain Size (μm) $\pm\sigma$	% served $\pm\sigma$	Fully Bars	Pre- Bars	% Avulsions $\pm\sigma$	Transitional Avulsions $\pm\sigma$
Shire	1.48 \pm 0.954	7.07×10^{-4} \pm 66.3%	246 \pm 97.3	40 \pm 5.83	40 \pm 5.83		22.4 \pm 5.98	
Molina	1.72 \pm 1.43	6.95×10^{-4} \pm 67.3 %	241 \pm 104	11.7 \pm 4.04	11.7 \pm 4.04		81.6 \pm 4.97	
Atwell Gulch	1.68 \pm 1.34	5.56×10^{-4} \pm 57 %	249 \pm 89.2	33 \pm 8.43	33 \pm 8.43		17.2 \pm 4.42	
	$p = 0.973^*$	$p = 0.676^*$	$p = 0.963^*$	$p \ll 0.001^\dagger$	$p \ll 0.001^\dagger$		$p \ll 0.001^\dagger$	

*Kruskal–Wallis ANOVA

$^\dagger \chi^2$ test

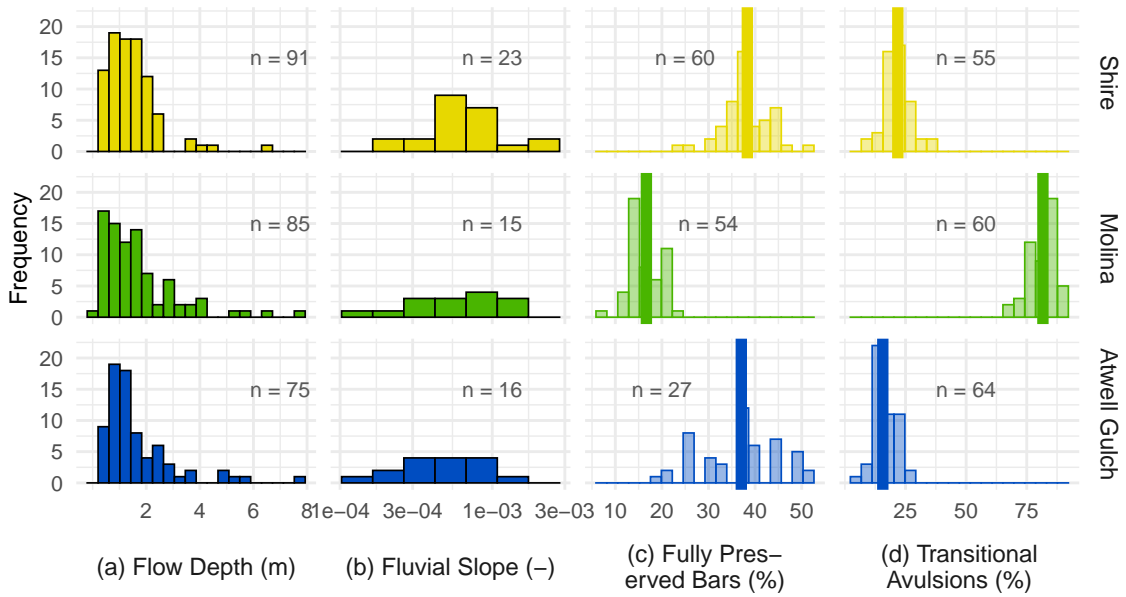


Figure 2.3: Estimates of paleohydraulic parameters from the Wasatch Formation in the Piceance Basin. Paleoflow estimates represent new data collected in this study aggregated with published sources. Paleoslope measurements are derived from a subset of paleo-depth data, paired with grain size data. Bar preservation estimates are derived from 3D outcrops, and avulsion style is tabulated from a separate dataset. Vertical lines represent the measured proportion of fully preserved bars and transitional avulsions in panels C and D. The shaded histograms represent bootstrapped values to visualize the standard error. Statistics and values found in Table 2.1.

the PETM as compared to the intervals before (Atwell Gulch) and after (Shire). Channel mobility is sensitive to changes in sediment supply if the change impacts the water-to-sediment ratio (Bryant et al. 1995). Since water discharge was likely to have been consistent during the PETM, if channel mobility were enhanced by an increase in sediment supply, an adjustment to channel gradient would be expected to handle the additional load. Our estimates do not resolve an adjustment in channel gradient (Table 2.1), which would be required to convey elevated sediment discharge during the PETM. There are three main sources of uncertainty and variability that preclude this interpretation. First is the variability in the data itself, where grain size and flow depth estimates all have large variance relative to the difference in median. Second is the uncertainty inherent in the paleoslope relation we use (Equation 2.1). Each of the parameters (α_0 , α_1 , and α_2) encompass substantial variance, such that predictions using this model can only be constrained within an order of magnitude. Finally,

Equation 2.1 is not specifically formulated for rivers with high runoff variability, so predictions are difficult to generalize. In short, the basic observation that depth and grain size are equivalent precludes an interpretation of enhanced slope during the PETM, and each additional source of uncertainty only compounds the issue.

Thus, lacking evidence for enhanced sediment supply, we interpret that the long-term time-integrated sediment flux in the Piceance Basin was practically stable throughout the PETM. The abundant evidence of enhanced channel mobility is therefore best explained simply as a consequence of short-term runoff variability during the PETM without a change in sediment supply (Esposito et al. 2018). Mechanistically, intervals of high-intensity flow would have exerted higher shear stress on channel banks, promoting enhanced erosion and accelerated lateral migration (Konsoer et al. 2017). This mechanism implies that channels during the PETM may also have widened or become braided (Johnson and Flores 2003), but field observations for this possibility are equivocal. Elevated bed shear stress during intensified flooding would have also enhanced bed material entrainment (Rouse 1939), such that overbank flows transported suspended coarse material to build crevasse splays, in agreement with our finding that avulsions were more likely to be stratigraphically transitional during the PETM. Altogether, the channel-dominated strata and lack of bar preservation in the Molina Member parallel observations from studies in a number of modern rivers with highly variable flow summarized in Fielding et al. (2018) as well as experimental studies (Esposito et al. 2018), and favor a scenario where discharge variability increased, but overall sediment supply remained stable.

The consequence of increased lateral mobility and crevasse-dominated avulsions was to enrich floodplain strata with bed material. Bar preservation estimates imply that mobile channels reworked near-surface deposits, preferentially entraining fines and transporting them downstream, while a change in avulsion style partitioned suspended bed material into floodplain deposits. Since a change in sediment supply

cannot be inferred and fluvial slope was unchanged through the PETM, sediment mass-balance dictates that increased sand concentration in the Piceance Basin must have occurred in conjunction with increased fine sediment flux downstream. This model of fluvial response to changing hydroclimate during the PETM explains broad trends across depositional environments without requiring a continent-scale increase in sediment and water flux.

2.6 Summary

In this study, paleohydraulic techniques were applied in the Piceance Basin of western Colorado to constrain changes in channel-floodplain processes connected with abrupt climate change during the PETM. The analyses indicate that fluvial channel geometries including depth and slope are consistent across the PETM boundary. However, fluvial structures are more often truncated and cross-cut during the PETM interval, and avulsions become transitional in nature. Taken together with experimental and observational studies of discharge variability and paleoclimate evidence from the region, these findings from the Piceance Basin serve as an example that, all else being equal, terrestrial floodplains subjected to seasonally intense precipitation experience accelerated channel dynamics. In this way, mud bypassed the floodplain through morphodynamic reworking, while sand was retained in the basin. This framework emphasizes that shifting hydrological regimes under global warming need not result in transiently high sediment fluxes or hillslope sediment mobilization, but rather may simply reäpportion sediment in alluvial basins through morphodynamic sorting.

Chapter 3

Non-monotonic Fluvial Response to Changes in Flooding Intensity

Abstract

Overbank flooding is a ubiquitous condition in natural rivers that modifies floodplain sediment dispersal and impacts channel mobility. While variable discharge is a critical component driving these processes, fluvial landscape evolution is typically modeled by simplifying the hydrograph to an equivalent steady discharge; namely, the channel-forming discharge. In this framework, changes in the hydrograph only affect landscape evolution if they modify the channel-forming discharge, but different formulations for the channel-forming discharge can generate a range of predictions from the same input hydrograph. Here, we investigate how hydrographs with different flood intensities affect channel mobility, sediment accumulation patterns, and alluvial morphology using a suite of physical experiments where a fan delta grew by dispersing a cohesive sediment mixture into a basin. Flood intensity (Q_v) was defined as the ratio of the maximum discharge to the minimum discharge, i.e. $Q_v = Q_{max}/Q_{min}$. The experiments spanned three levels: no flooding ($Q_v = 1$), low-intensity flooding ($Q_v = 1.5$), and high-intensity flooding ($Q_v = 3$), while the time-averaged discharge was equivalent between all flooding regimes. Across this gradient, channel mobility, alluvial morphology and sediment dispersal scaled non-monotonically with flooding intensity, and the data suggest that levee-building processes are responsible for this behavior. Channel mobility and sediment dispersal in the experiments are driven by avulsions. With no flooding, levee breaches experienced consistent, intermediate levels of shear stress, so the probability of a crevasse splay giving way to an avulsion was set by

the long-term balance between aggradation and sediment supply. For high-intensity flooding, avulsions were more frequent, as increased shear stress on channel margins produced runaway erosion of crevasses. In contrast, during low-intensity flooding, low-stress overbank flow resulted in sedimentation within crevasses, annealing them over successive flood waves. In this way, low-intensity flooding minimized channel mobility, and sediment was transported longitudinally to the channel mouth, while high-intensity flooding enhanced channel mobility and dispersed sediment laterally across the delta topset. The no-flooding condition resulted in intermediate channel mobility and sediment dispersal to both the topset and the shoreline. Localized sediment deposition as a result of low-intensity flooding also accentuated topset relief and shoreline rugosity, whereas extensive sediment dispersal during high-intensity flooding diminished topset roughness and shoreline rugosity, and the no flooding condition resulted in intermediate relief and rugosity. These results point to the importance of discharge variability for governing sediment exchange across channel margins, and its influence on fluvio-deltaic morphodynamics.

3.1 Theoretical background and approach

Rivers experience variable discharge conditions over time, and the hydrograph defines the frequency and magnitude distribution of flow and sediment transport events. The integrated history of flow determines channel dimensions and mobility, which directs sediment dispersal and shapes landscape morphology (Pickup and Rieger 1979). However, due to the complexity associated with morphodynamic feedbacks, it is common when modeling fluvial channel and landscape development to simplify the hydrograph into a characteristic steady discharge; namely, the channel forming discharge (Wolman and Miller 1960; Leopold and Maddock Jr. 1953).

An issue with this approach is that the methods used to calculate a character-

istic discharge do not produce unique solutions: many different types of hydrographs can be summarized to generate the same characteristic value. One formulation used by Blom et al. (2017) exemplifies the strategy. Blom et al. (2017) consider a hydrograph composed of only two flows that transport sediment according to an appropriate sediment transport relation, (e.g. Engelund and Hansen 1967), a maximum flow (Q_{max}) and a minimum flow (Q_{min}), and express the equivalent steady sediment discharge (\bar{Q}) as:

$$\bar{Q} = \alpha Q_{min} + (1 - \alpha) Q_{max}, \quad (3.1)$$

where α is the occurrence frequency of Q_{min} , and the frequency of Q_{max} is by definition $(1 - \alpha)$. In Equation 3.1, α can be termed a flood *intermittency* (Parker et al. 1998), and the difference between Q_{max} and Q_{min} is the flood *magnitude* (Latrubesse et al. 2005). It can be clearly seen that a given value of \bar{Q} cannot be expressed by a unique flood magnitude, because the intermittency may also vary.

Importantly, this and other approaches are intended to be used to calculate equilibrium sediment transport conditions and other system properties like channel geometry (Blom et al. 2017; Naito and Parker 2019). Tuned to capture specific processes and aspects of the morphodynamic system, models using this approach yield insight about these processes, but are difficult to generalize.

Consequently, predictions for channel geometry and sediment transport can contradict depending on the formulation used to calculate the equivalent constant flow. For instance, Blom et al. (2017) indicate that all else being equal, an increase in flow variability generates an increase in channel width; this supposition is supported by experimental studies (Esposito et al. 2018). However, recent numerical modeling studies by Naito and Parker (2019) found that channel width decreases as flow variability increases, because enhanced floodplain aggradation builds banks that confine flow and narrow the channel. This supposition is supported by field observations from

sand-bed channels (Pizzuto 1986). Interestingly, however, both Blom et al. (2017), (their Figure 5), and Naito and Parker (2019)—Figure 3.1—indicate monotonic relationships between increasing flood variability and the equilibrium depth, width, and slope.

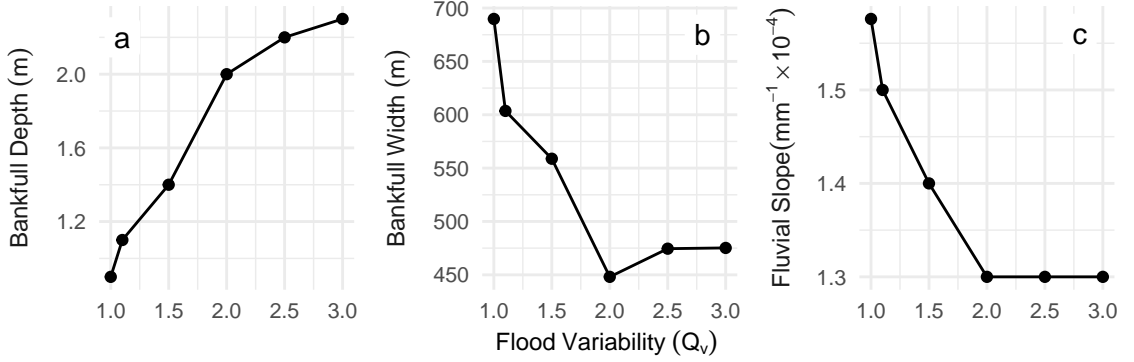


Figure 3.1: Example model results using the framework in Naito and Parker (2019), showing generally monotonic scaling of (a) bankfull depth, (b) bankfull width, and (c) channel slope across a gradient of Q_v .

In this particular case, the discrepancy appears to arise because each formulation describes sediment exchange between the channel and floodplain differently. It is known that in order to faithfully model many floodplain processes, a variable hydrograph is required (Lauer and Parker 2008), yet the appropriate formulation is not clear, as the impact of overbank floods on sediment transport processes at the basin scale remains underconstrained. To cast light on this issue, the present study defines a parameter, *flood intensity* (Q_v), as the ratio of Q_{max} and Q_{min} ,

$$Q_v = \frac{Q_{max}}{Q_{min}}, \quad (3.2)$$

provided that α changes to maintain a constant \bar{Q} . By substituting Equation 3.2 into Equation 3.1, an expression for α may be derived in terms of Q_v , Q_{min} , and the chosen constant discharge: \bar{Q}_c ,

$$\alpha = \frac{\frac{\bar{Q}_c}{Q_{min}} - Q_v}{1 - Q_v}. \quad (3.3)$$

In this way, Q_v describes the variability of flow relative to a baseline, and allows changes in the hydrograph to be separated from adjustments in the equivalent steady flow. This is of critical importance because while flow variability is recognized to impact channel mobility and sediment transport, it remains challenging to parse the relative effects of flood magnitude, intermittency, and fluvial response to an equivalent steady flow.

For example, channel mobility scales with both water discharge and sediment supply (Bryant et al. 1995), but Esposito et al. (2018) show similar results with only a change in Q_v . Bolstering this assertion, numerical modeling presented by Naito and Parker (2019) demonstrates the importance of flood intensity on bank erosion. Experiments also show that flow variability is coupled to overbank erosion and chute cut-offs (Van De Lageweg et al. 2013), in addition to levee building and in-channel sediment aggradation (Esposito et al. 2018), all of which play critical roles in the channel avulsion process (Mohrig et al. 2000). Modern systems characterized by highly seasonal discharge exemplify this feedback, where both lateral migration and avulsion frequency are enhanced relative to rivers with muted hydrographs (Leier et al. 2005; Fielding et al. 2018). Meanwhile, however, an increase in flood intermittency can suppress channel mobility because of sediment reworking during low-flow conditions that entrench channels (Miller et al. 2019)

This study quantifies floodplain morphodynamic feedbacks across a gradient of flooding intensity (Q_v). By using Q_v as the independent variable, we separate changes in flow variability from changes in equivalent steady discharge, and characterize the main ways in which variable flow influences channel mobility, sediment dispersal, and alluvial morphology in an experimental fan delta.

3.2 Methods

3.2.1 Experimental design

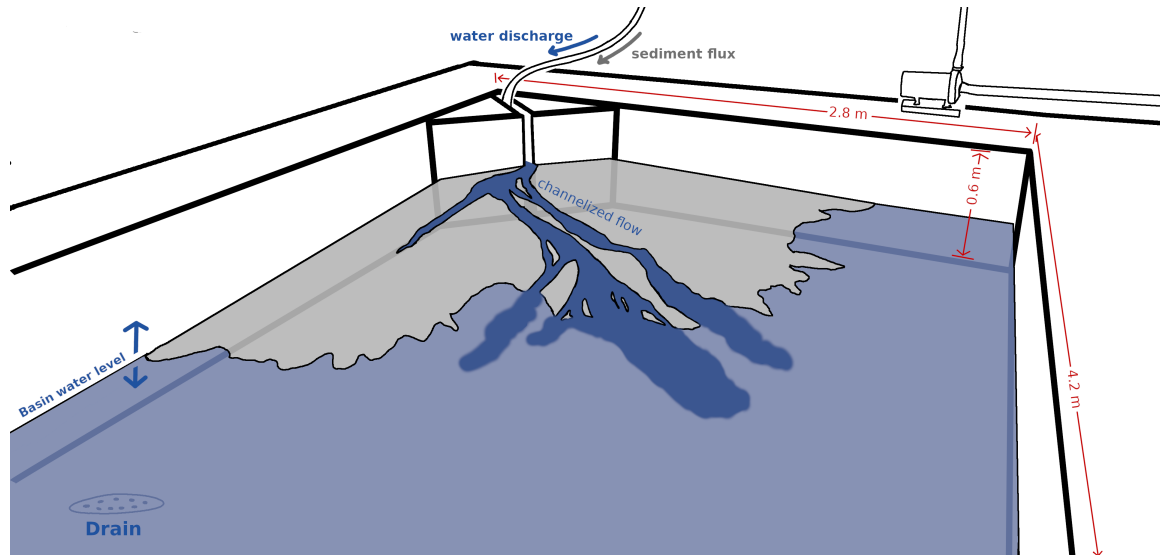


Figure 3.2: The Tulane University Delta Basin measures $4.2 \times 2.8 \times 0.6$ m. Water and sediment are fed from a funnel and pipe system, where the pump for water and feed rate of sediment are controlled on a minute-by-minute basis from a central computer. Water and sediment exit the inlet channel and form a delta in the corner of the basin, that can therefore spread over a 90° swath of the basin. Channels form on the delta topset and direct water and sediment to the shoreline. Water level is controlled via a computer-operated weir (not shown) that is hydraulically connected to the drain on the floor of the basin. By moving the weir vertically, the water level can be controlled with sub-millimeter precision.

A suite of physical experiments were conducted in the Tulane University Delta Basin where fan deltas evolved in response to three discrete flooding regimes: no flooding ($Q_v = 1$), low-intensity flooding ($Q_v = 1.5$), and high-intensity flooding ($Q_v = 3$). The basin has dimensions of $4.2 \times 2.8 \times 0.6$ m, and sediment and water were mixed and fed into the basin from an inlet channel, forming a fan delta that spread radially up to 90° (See Figure 3.2). The feed rate of sediment and water at the apex is set by a computer-controlled commercial feeder and pump, respectively, and water drains from the delta basin via a computer-controlled weir that maintains basin water level with sub-millimeter precision. The experiments featured long-term aggradation, which was induced by steadily raising the water level throughout the

experiment. The water-level-rise rate is calibrated to generate accommodation equal to the long-term sediment-feed rate, so that the average radial shoreline was stable through time (Kim et al. 2006). The sediment used in this experiment was a bimodal mixture of coarse sand, fine sand, and silica flour, with additives that impart cohesion. This mixture enhances channelization compared to cohesionless mixtures, generating rich channel-floodplain interactions and delta lobe-switching via avulsions (Hoyal and Sheets 2009).

Table 3.1: Control parameters for Tulane University Delta Basin for experiment spanning three levels of a gradient of Q_v . *Estimated from Li et al. (2016).

	No Flooding	Low-intensity	High-Intensity
Flood Intensity (Q_v , —)	1.0	1.5	3.0
Flood discharge (L/s)	0.172	0.213	0.426
Baseline discharge (L/s)	0.172	0.142	0.142
Equivalent constant discharge (L/s)	0.172	0.172	0.172
Sediment concentration (lb/L)	0.005	0.005	0.005
Basin water level rise rate (mm/hr)	0.25	0.25	0.25
Flood cycle time (T_f , min)	30	30	30
Compensation time scale (T_c , hrs)*	50	50	50
Total run time (hrs)	100	100	100

Over the duration of the experiment, the sediment mixture, rate of basin water-level rise, time-averaged sediment and water flux, and the water-to-sediment ratio were all held constant (Table 3.1). Floods were designed as a Gaussian function of time (Equation 3.4). This design permitted the intermittency and magnitude of floods to smoothly covary while maintaining a constant integrated discharge over every flood cycle despite changes in amplitude. In this way, the effect of hydrograph variability was separated from changes in overall water and sediment flux. Discharge over every flood cycle was thus defined in reference to an equivalent constant discharge (\bar{Q}_c), and Q_{min} was defined as a fraction of \bar{Q}_c , such that $Q_{min} = k\bar{Q}_c$. In this way, over a flood cycle of duration T_f , discharge is given as:

$$Q(t) = k\bar{Q}_c \left(1 + (Q_v - 1)e^{-\left(\frac{k\sqrt{\pi}(Q_v-1)}{(k-1)T_f}t\right)^2} \right) \quad (3.4)$$

on the closed domain $[-T_f/2, +T_f/2]$. For this experiment, $k = 0.825$ and $T_f = 30$ minutes, where sediment and water were specified every 30 seconds, yielding an experimental hydrograph (see Figure 3.3).

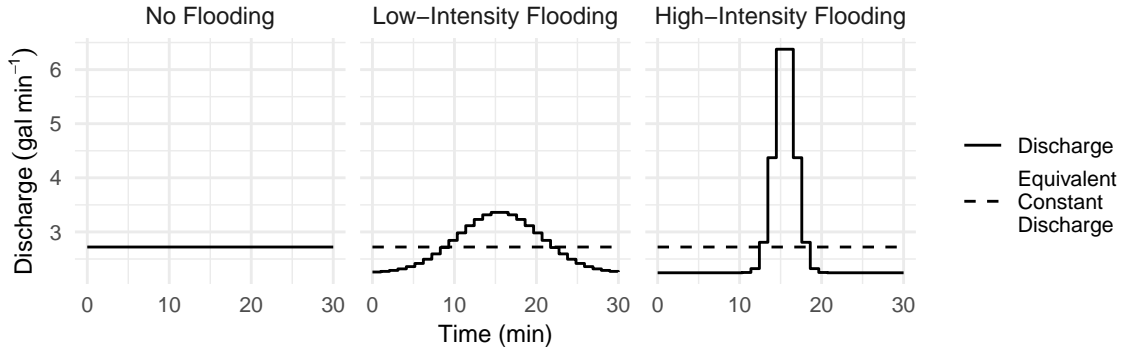


Figure 3.3: Flood pulse design for experimental runs computed using Equation 3.4. From left to right, these flood pulses exemplify flood flooding intensity for $Q_v = 1.0$, $Q_v = 1.5$, and $Q_v = 3.0$. The baseflow discharge (Q_{min}) is 82.5% of the equivalent constant discharge (\bar{Q}_c).

For the experiments with low-intensity flooding ($Q_v = 1.5$) and high-intensity flooding ($Q_v = 3$), floods occurred every 30 minutes. This interval is chosen because it is frequent relative to autogenic cycles of sediment storage and release, ensuring that sedimentary dynamics were not impacted by individual flood events, but rather influenced by flooding as a background condition (Kim et al. 2006; Miller et al. 2019). Since the primary depositional process occurring in this experimental apparatus is the successive emplacement of delta lobes, the appropriate autogenic timescale for this comparison is the *compensation timescale*, (T_c), defined as the ratio of the characteristic topographic relief (l) to the long-term aggradation rate (r) (Straub et al. 2009), that is:

$$T_c = \frac{l}{r}, \quad (3.5)$$

Over a duration of time T_c , depositional lobes stack such that sediment is spread

evenly over the delta topset. In this experimental apparatus, $T_c \approx 50$ hours (Li et al. 2016), and each flood cycle had a duration $T_f = 30$ minutes; giving ~ 100 floods per T_c . Each experimental dataset comprises 100 hours of experimental run time, equivalent to $\sim 2 \times T_c$. This ensures that sufficient time elapsed to characterize the dynamic equilibrium of the delta, and that measured quantities were statistically stationary.

3.2.2 Data collected

Two main types of data were collected from these experiments to constrain channel mobility, sediment dispersal, and fluvial morphology.

For every hour of runtime, topographic data were collected using a terrestrial lidar scanner. The 3D point-cloud data were then gridded at a horizontal resolution of 5×5 mm with a vertical resolution of 1 mm. Rarely, a topographic scan failed ($\sim 0.2\%$ of all scans), and since some analysis of scan data can be biased by gaps in the record, the missing data was interpolated on a pixel-by-pixel basis using the closest complete scans before and after. Topographic scans were then clipped to the basin water level, and used to generate masks of the delta topset and identify the shoreline. Sequential scans were then post-processed to generate synthetic stratigraphy, where each topographic surface was clipped to reflect subsequent erosion such that only preserved depositional surfaces remained (Strong and Paola 2008).

Throughout the experiment, overhead RGB images were collected every 15 minutes to capture each flood peak and trough, then corrected for lens distortion using Agisoft Metashape. Images also occasionally failed to capture ($\sim 0.1\%$ of all images), and the missing data were discarded. For analysis, images were projected into the reference frame for topographic scans, and resampled to 5×5 mm pixel resolution. The area comprising basin water was then clipped in every image using

the topographically-derived topset mask, with the remainder analyzed to identify channel locations. Blue dye was injected into the water for every overhead image, so the intensity of blue color in the images is used to discriminate between active channels and dry land by thresholding the image with an RGB Normalized Difference Water Index (rgbNDWI). rgbNDWI was calculated as:

$$\text{rgbNDWI} = \frac{G - R}{G + R}, \quad (3.6)$$

where G is the green band and R is the red band of the RGB image. This method produces a non-dimensional index, and a threshold was applied to produce binary masks showing the area occupied by channels on the delta. One mask was created for every hour of runtime, and the dataset of 300 masks (100 for each experiment) was then manually retouched to correct for spurious features captured by automated thresholding (Figure 3.4).

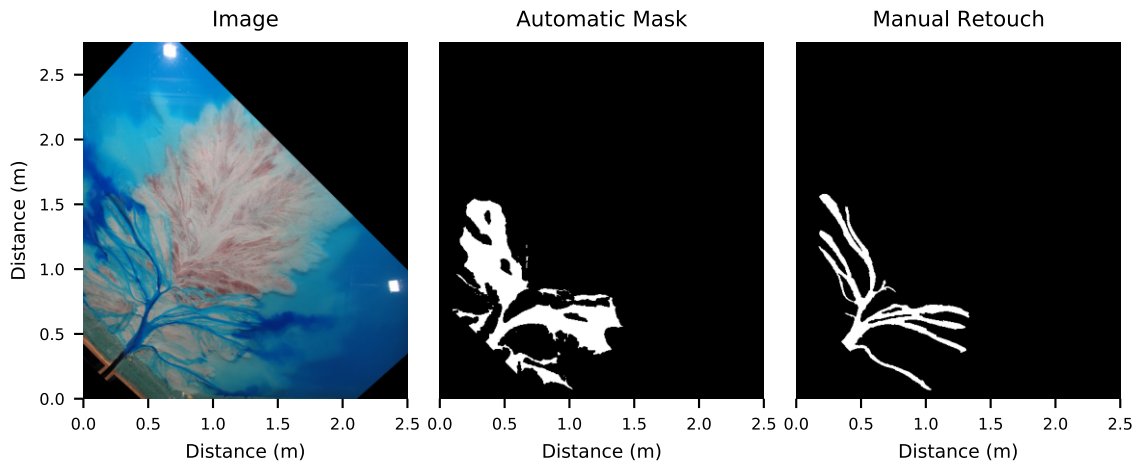


Figure 3.4: To construct channel masks, first the rgbNDWI is calculated from the input image, and a threshold is applied to extract concentrated areas of blue. Then, the basin water is clipped out and a binary erosion is conducted to remove unconnected pieces. Finally, each mask is manually retouched to generate a final image.

Additionally, in every run hour, levee breaches were located and counted from

overhead imagery. Levee breaches were identified in overhead images as locations on the channel banks where water escaped the channel during low flow. In this way, the count estimate reflects locations of potential failure during subsequent floods, rather than locations of overbank flow during floods.

At the end of the experimental run, the deposit was drained and dried, then cut along four strike sections. Each of these cuts was imaged and georeferenced to the basin, generating orthophotos of the face. Facies were interpreted in the cuts based on deposit geometries revealed by corresponding synthetic stratigraphy sections. Samples were taken from several locations in each cut, chosen to capture major facies. Grain-size distributions for these samples were generated using a laser particle size analyzer.

3.2.3 Channel mobility

As channels migrate laterally and avulse, the area occupied by channel decorrelates from its initial state as a function of time because channels visit new locations on the floodplain. Using channel mask data, correlation is described in terms of pixels, where the more pixels that change from “wet” to “dry”, the less two channel images overlap (Wickert et al. 2013). Thus, the normalized channel overlap between any pair of images, O_Φ is given as:

$$O_\Phi = 1 - \frac{D}{A\Phi}, \quad (3.7)$$

where D is the number of pixels that changed, A is the total area of the image, and Φ is a dimensionless parameter that gives the number of pixels that would be expected to change by randomly scattering wet and dry pixels across the surface (Wickert et al. 2013). Between two images, 1 and 2, Φ is expressed as:

$$\Phi = (w_1d_2 + w_2d_1), \quad (3.8)$$

where w_x and d_x are the fraction of wet and dry pixels in images 1 or 2. Theory dictates that channels will decorrelate according to an exponential decay function of the lag time between successive channel maps (Wickert et al. 2013):

$$O_{\Phi} = (a_M - p_M)e^{-Mt} + p_M, \quad (3.9)$$

where O_{Φ} is the normalized channel mask overlap, t is the lag time between masks, and p_M , a_M and M are constants. To quantify channel mobility using this method, the normalized overlap between successive channel masks was measured for each experiment, and an exponential model was fit for each dataset using Equation 3.9 by restricted maximum likelihood (Venables and Ripley 2002). The mobility of channels is interpreted using the reciprocal of the exponential decay constant ($1/M$), i.e. an e -folding time. Higher e -folding times imply immobile channels that decorrelate slowly, because channels remain in the same location over long lag times, whereas small e -folding times imply mobile channels.

3.2.4 Sediment dispersal

To evaluate the spatial heterogeneity of sediment dispersal and patterns of deposition in the fluvio-deltaic system, three approaches are employed. In the first, the spatial variation of sediment deposition was qualitatively assessed using isopach maps and circular sections constructed from synthetic stratigraphy. Spatial patterns of deposition are revealed by comparing isopach maps for equivalent intervals of each experiment, and circular sections highlight lateral variation in sediment thickness.

The second method quantifies the evenness of lateral sediment dispersal by measuring the completeness of stratigraphic columns as a function of discretization time, that is, the precision of timing that is desired for interpretation. Since episodes

of deposition are interspersed with hiatuses in the stratigraphic record, the history of accumulation in any given location is incomplete. Stratigraphic completeness is commonly defined as:

$$f_c \equiv \frac{t^*}{\hat{t}}, \quad (3.10)$$

where t^* is the amount of time represented by sediment, and \hat{t} is the total time encompassed by the stratigraphic column (Straub et al. 2020). Sadler (1981) defines completeness in a different sense, casting it as the ratio of accumulation rates, that is:

$$f_{sadler} \equiv \frac{\dot{z}}{\dot{z}_*}, \quad (3.11)$$

where \dot{z} is the perceived accumulation rate and \dot{z}_* is the true average accumulation rate. If \hat{z} is the full thickness of the stratigraphic column then $\dot{z} = \hat{z}/t^*$ and $\dot{z}_* = \hat{z}/\hat{t}$. Sadler (1981) noted that the perceived accumulation rate decreases with the averaging window (δt) as a power law function.

$$\frac{\dot{z}}{\dot{z}_*} = \left(\frac{\delta t}{\hat{t}} \right)^\beta \quad (3.12)$$

The exponent β , known as the Sadler exponent, takes on negative values and has physical meaning; it scales with the evenness of sediment deposition (Sadler 1981; Jerolmack and Sadler 2018). When using experimental data, however, it is more convenient to measure completeness via Equation 3.10. It can be shown that f_{sadler} is related to f_c as follows.

$$f_{sadler} = \frac{\dot{z}}{\dot{z}_*} = \frac{\hat{z}/t^*}{\hat{z}/\hat{t}} = \frac{\hat{t}}{t^*} = \frac{1}{f_c} \quad (3.13)$$

Therefore, it is clear that f_c is related to the averaging time window as follows.

$$f_c = \left(\frac{\delta t}{\hat{t}} \right)^{-\beta} \quad (3.14)$$

Because β takes on values between -1 and 0, this is a convex-up power law function that, importantly, has a restricted range from 0 to 1. The stratigraphic record can be at minimum 0% complete, and above a critical averaging timescale, the stratigraphic record will essentially always represent some deposition, so the relationship will saturate at $f_c = 1$. However, in between these bounds, the data are well-described by a power-law. For these experiments, the critical timescale is the compensation timescale (T_c), because it is at that discretization time that one expects to see delta lobes evenly spread across the topset. In this way, using stratigraphic columns extracted from circular sections of the experimental data, f_c was calculated for each column across a range of δt values. These data were then fit with Equation 3.14 using Markov Chain Monte-Carlo (MCMC) sampling methods, and the posterior distributions of β were interpreted. In general, β scales with sediment evenness, with higher absolute values indicating less even deposition, and low absolute values indicating more even deposition.

The third method for characterizing spatial patterns of sediment deposition measures the abundance of channel deposits in the strata. High channel mobility and even sedimentation will increase the amount of channel deposits, whereas low channel mobility will spatially restrict channel deposits, resulting in overall lower representation in the stratigraphy. Synthetic stratigraphy was used to sub-sample channel-mask data and produce a dataset showing the abundance of channel deposits throughout the stratigraphic volume. The relative abundance of channels in each experiment was then quantified as the fraction of the deposit in different stratigraphic cuts that was channel or floodplain.

3.2.5 Delta-floodplain morphology

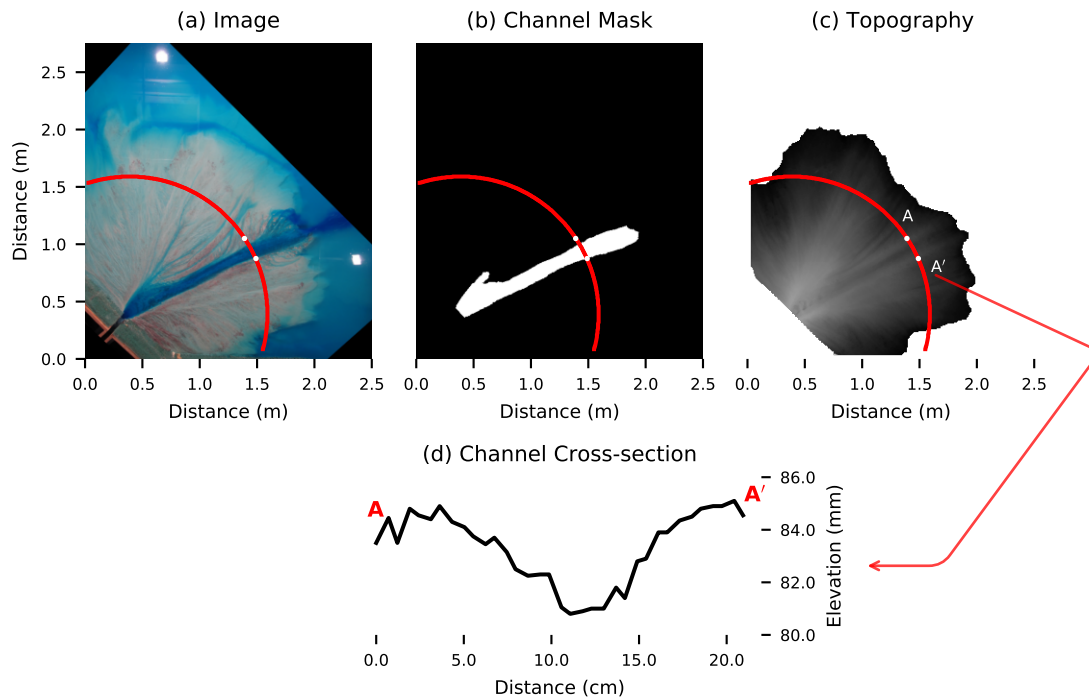


Figure 3.5: In order to extract channel dimensions from coupled topography and overhead imagery data, images were georeferenced to the topography. Circular sections were taken, and changes from “dry” to “wet” (0 to 1) were identified, which defined the left and right bank of the channel. The channel width was taken as the distance between the points, and a line of pixels between the corresponding points were extracted from the topography, and the total relief was taken as the channel depth. Channel slope was taken by extracting all topographic points where the channel mask was “wet” and a least-squares fit was applied to the elevation as a function of radius from the apex.

To document changes in channel morphology throughout each experiment, average estimates of channel width, depth, and slope were produced for each experiment. To measure channel geometries, circular sections were taken across each channel mask at designated radii, and channel banks were identified as points where the edges of channels intersected the section. Channel width was then measured as the distance across the channel between points on the banklines, and topographic data was extracted along this transect. Channel depth was measured as the total topographic relief along this channel transect (see Figure 3.5). Channel slope was estimated by

extracting topography within each channel mask, and fitting a linear regression to the topography data along radial transects from apex to shoreline.

Changes in floodplain and deltaic morphologies, including the average delta topset slope and topographic relief were also documented. Delta topset slopes were calculated by extracting average radial topographic profiles from the delta apex to the shoreline. Floodplain relief was estimated by detrending the delta topset using the calculated slopes and computing the vertical distance from the 25th percentile to the 95th percentile of the detrended elevation data (see Figure 3.6).

The shoreline was defined as topography within 2 mm of the water surface elevation in the basin. Shoreline rugosity (R) was computed as the coefficient of variation in radial distance between every point on the shoreline and the delta apex:

$$R_j = \sqrt{\frac{1}{N} \sum_{i=1}^N \left(\frac{r_{i,j} - \bar{r}_j}{\bar{r}_j} \right)^2}, \quad (3.15)$$

where R_j is the rugosity of the shoreline at time j , $r_{i,j}$ is the distance from the apex to all points i that define the shoreline in image j . \bar{r}_j is the mean distance from the delta apex to the shoreline in image j , and N is the total number of spatial points that define the shoreline.

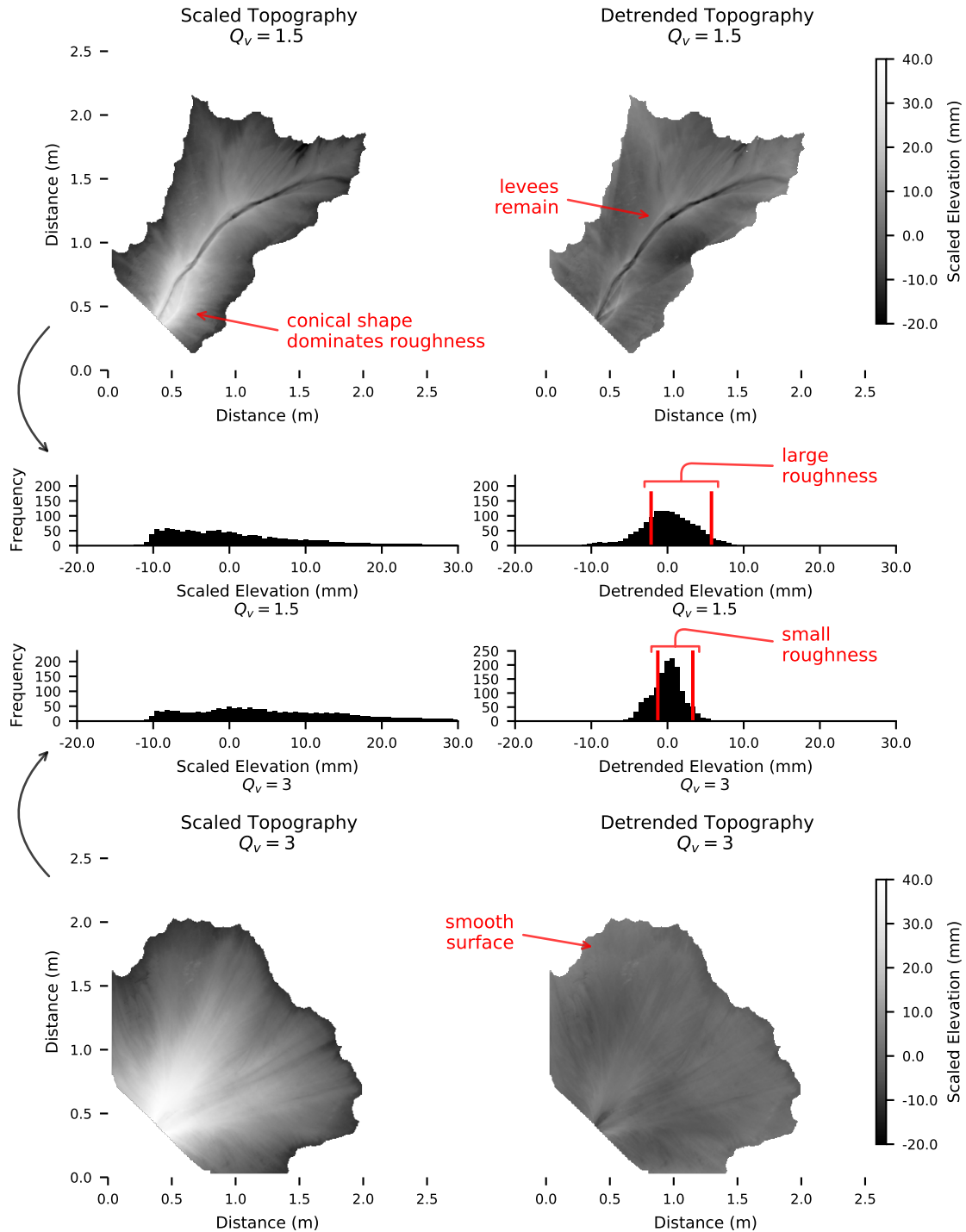


Figure 3.6: To remove the overall conical trend and estimate the surface roughness of the topset, each topographic surface was vertically displaced to be centered on zero (Scaled Topography), and radial transects were taken from the apex to shoreline, and all pixels along the transect were detrended by the slope of the transect (Detrended Topography). Histograms of the elevation images are shown before and after, demonstrating that this procedure removes the long-wavelength topography and retains roughness features like levees. The roughness was taken as the distance from the 25th to 95th percentiles of the detrended histogram.

3.3 Results

3.3.1 Channel mobility

Estimates of the e -folding time for channel overlap decay (Equation 3.9) indicate that channel mobility scaled non-monotonically with flooding intensity. In the no-flooding experiment, the channel overlap e -folding time was 19.8 hours. When low-intensity flooding was imposed, the e -folding time increased to 23.9 hours, an increase of $\sim 20.7\%$. However, when flood intensity increased to $Q_v = 3$, the e -folding time decreased to 4.59 hours, a decrease of $\sim 76.8\%$ from no-flooding. In terms of T_c , the e -folding time for no flooding is 39.6% T_c , compared to 47.8% T_c for low-intensity flooding and 9.18% T_c for high-intensity flooding (see Table 3.2 and Figure 3.7).

3.3.2 Sediment dispersal

Channel and floodplain morphodynamics impact sediment dispersal in the fluvial system, which manifests as the spatial unevenness of sediment deposits. Isopach maps prepared for each flooding regime demonstrate that sedimentation is evenly distributed across the delta topset in the high-intensity flooding experiment, highly localized when $Q_v = 1.5$, and intermediate when no flooding is present (Figure 3.8). In particular, isopach maps show that when low-intensity flooding is imposed, deposition is localized along alluvial ridges, generating clearly visible levee deposits (Figure 3.8, panel b). Meanwhile, deposition is also focused at the channel mouth, where the delta builds elongate lobes. Synthetic stratigraphic sections corroborate this observation, where thin lateral deposition adjacent to the floodplain is contrasted with thick levee deposits in proximal sections, but additional lobe deposition can be seen in the most distal cut.

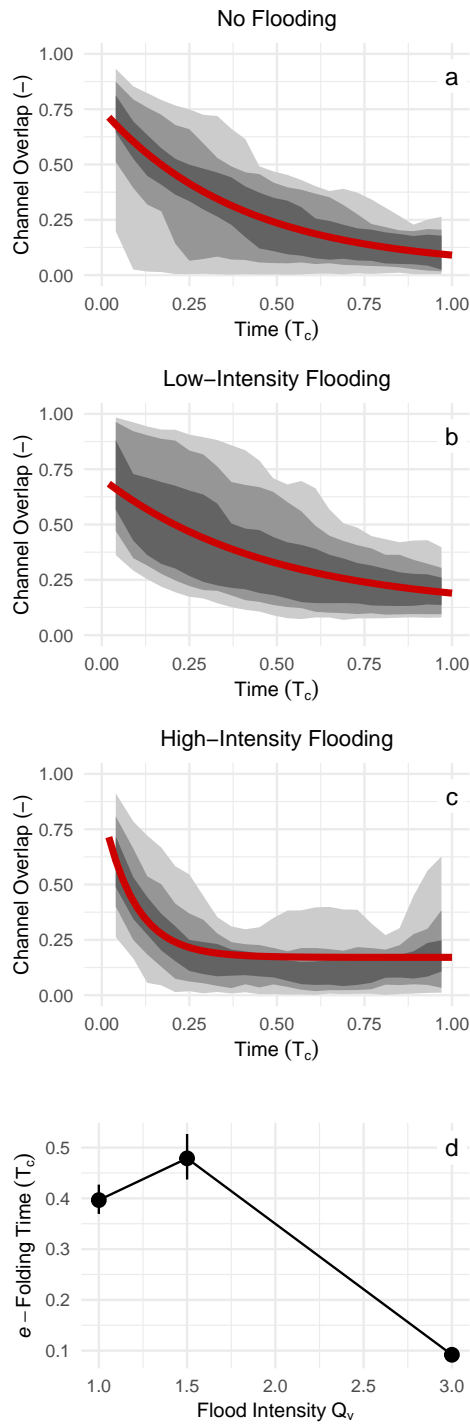


Figure 3.7: Panels a, b, and c show the decay of normalized channel overlap with successive lag times. The shaded regions show the distribution of the data, with the lightest band showing the 1st to 99th percentiles, the middle band showing the 10th to 90th percentiles, and the darkest showing the 25th to 75th percentiles. The red lines show model fits using Equation 3.9. Panel (d) shows estimates of the e -folding time ($1/M$) along with 95% confidence intervals. It is noted that the channel overlap decay e -folding times scale non-monotonically with Q_v .

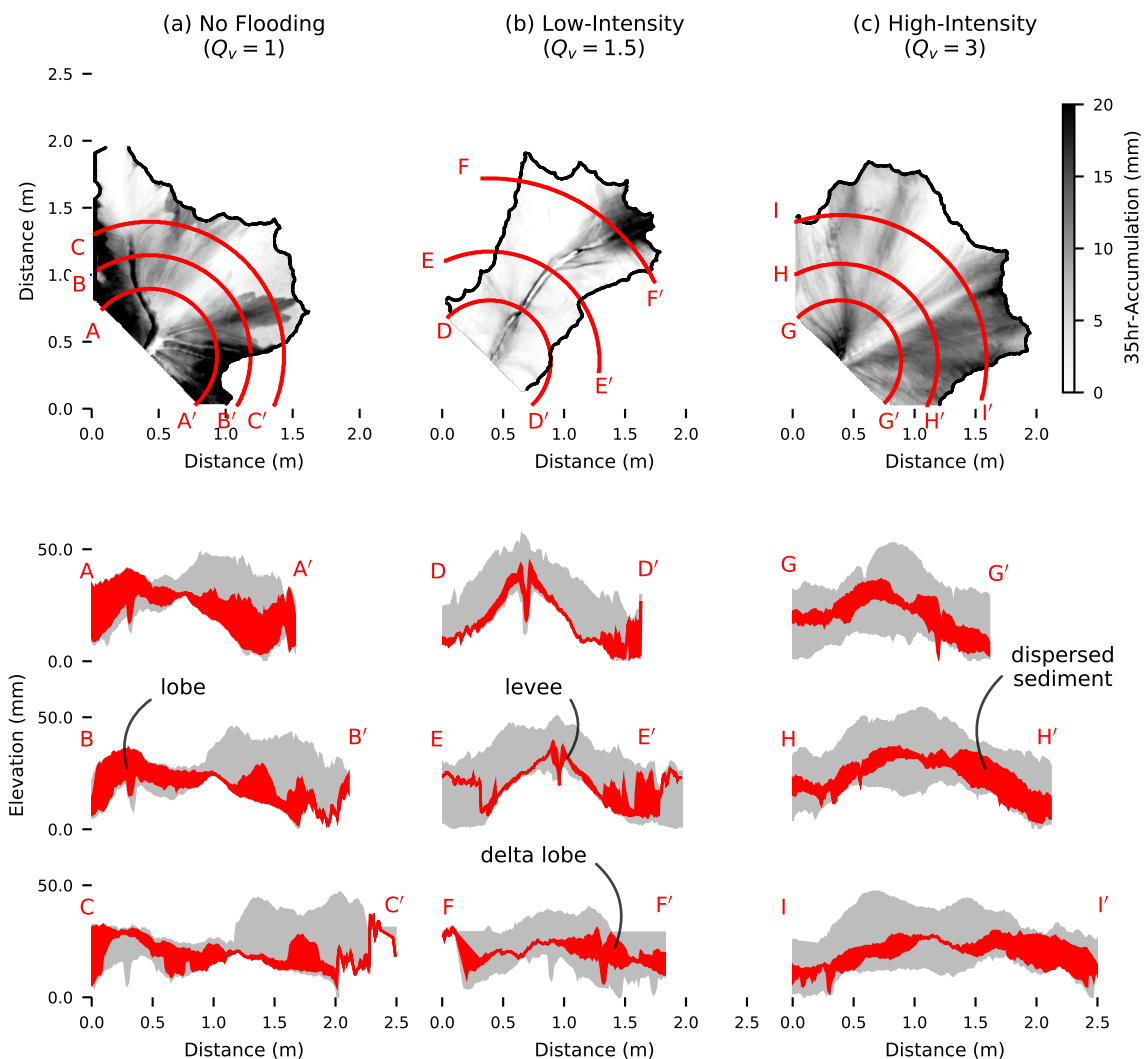


Figure 3.8: Sediment isopach maps for a sample 35 hour interval across three values of Q_v . Dark colors indicate thicker deposition, and the shoreline is outlined for clarity. Circular sections shown in red are displayed below, where the same 35 hour interval is highlighted in red, whereas the deposit for the full 100 hours of runtime is shown in gray. Note that sediment thickness is variable over the illustrated interval when $Q_v = 1$ because the active delta lobe switches from one side of the delta to the other during the episode. Sediment thickness is more variable when $Q_v = 1.5$, because levees that can be seen aggrading on either flank of the channel confine flow and prevent it from being distributed laterally. In contrast, the sediment packages deposited when $Q_v = 3$, are less variable in thickness.

When flooding intensity is high ($Q_v = 3$), sediment is deposited evenly across the floodplain of the delta, indicated by consistent thickness in the isopach map. Consistent thickness of coeval deposits in proximal as well as distal stratigraphic sections also demonstrates relatively uniform deposition. When no flooding is present, ($Q_v = 1$), sediment deposition is focused in delta lobes, but not to the same degree as during low-intensity flooding. In fact, lateral sediment dispersal can clearly be seen in stratigraphic sections as well as the isopach maps in Figure 3.8a.

Channel abundance estimates (Figure 3.9) show that the abundance of channels in the stratigraphic record scales non-monotonically with flooding intensity. When low-intensity flooding was imposed, channel deposits comprise a minor portion of the delta stratigraphy. In contrast, the concentration of channels in the stratigraphy increases with high-intensity flooding. When no flooding is imposed, the concentration of channels in the delta stratigraphy is intermediate, comprising a smaller proportion of the deposit than a high-intensity flooding delta, but more than a low-intensity flooding delta.

Grain size samples taken from channelized and floodplain sediments for each experimental stage show that channelized deposits are, on average, coarser than floodplain sediments (Figure 3.10a and 3.10b). Channel deposits are also relatively coarse compared to the input mixture (shown in black), whereas the floodplain deposits are relatively fine. Additionally, channel abundance consistently decreases as a function of radial distance from the delta apex (Figure 3.10 (d), (e), and (f)), indicating that proximal deposits consist of a larger fraction of coarse sediment than distal deposits, on average.

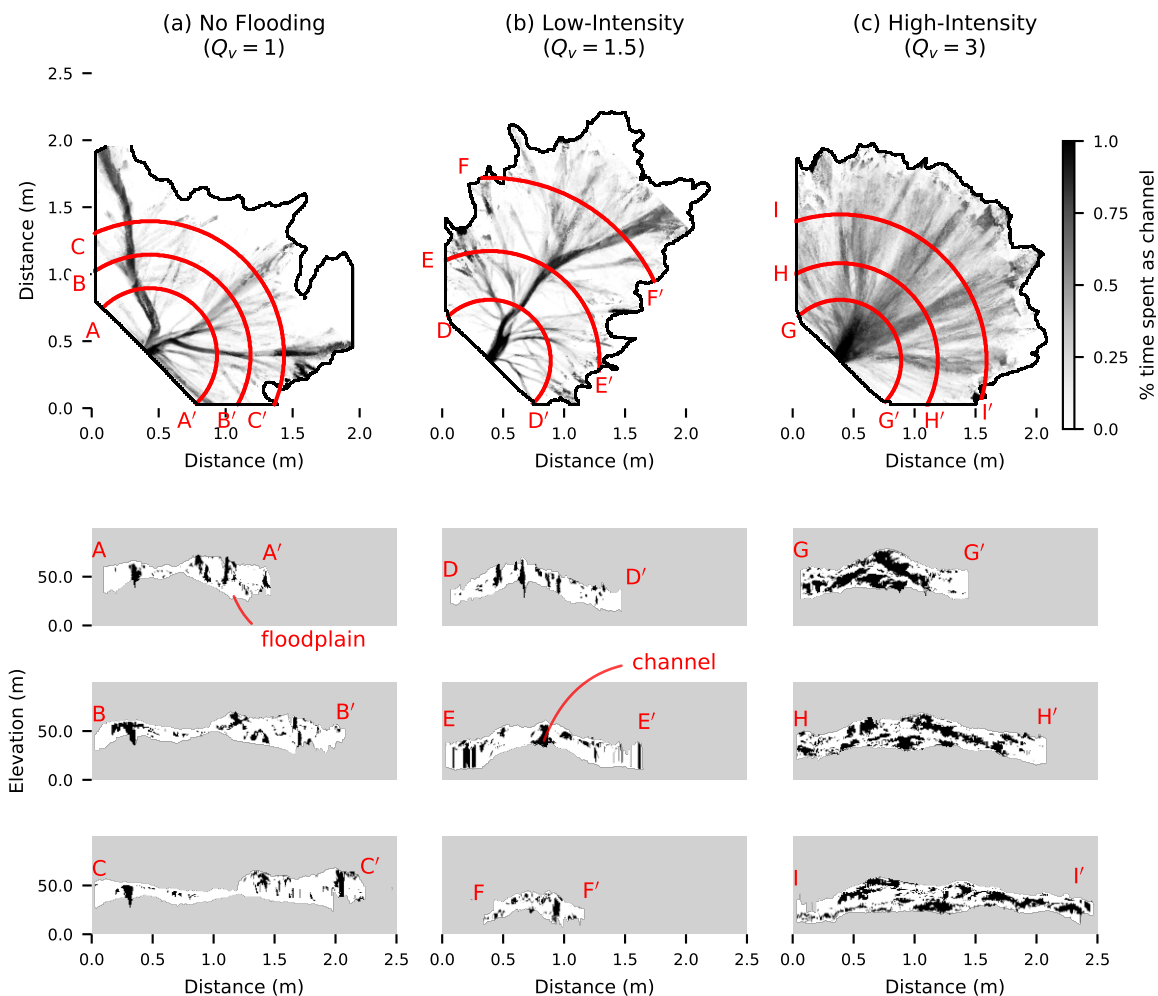


Figure 3.9: Channel abundance maps and stratigraphic sections. In stratigraphic sections, channel deposits are indicated in black, while floodplain deposition is indicated in white. In the plan-view maps, higher channel visitation is indicated by darker colors, whereas light colors demonstrate that channels rarely visited that location. Visually, it is clear that channels are more abundant in the stratigraphy when $Q_v = 3$, whereas the sections for $Q_v = 1.0$ and $Q_v = 1.5$ are less clear. The abundance of channels in the strata as a function of the radius is quantified in Figure 3.10

Finally, the evenness of sediment deposition was quantified by analyzing the decay of stratigraphic completeness as a function of discretization timescale. Extracting preservation data along a circular section of each experimental dataset at a medial distance from the delta apex, the completeness of each location along the section was calculated for a range of δt values from the finest discretization possible up to the compensation timescale. These data were modeled with Equation 3.14 using MCMC methods to produce posterior distributions of β . During low-intensity flooding, β assumes a maximum value (Figure 3.11d), indicating uneven sediment dispersal, and a propensity to favor downstream sediment transport versus lateral sediment dispersal. In contrast, β assumes a minimum value when $Q_v = 3$, indicating that high-intensity flooding promotes lateral sediment dispersal to evenly cover the delta topset. When $Q_v = 1$, β assumes an intermediate value, indicating a balance between lateral vs downstream sediment dispersal.

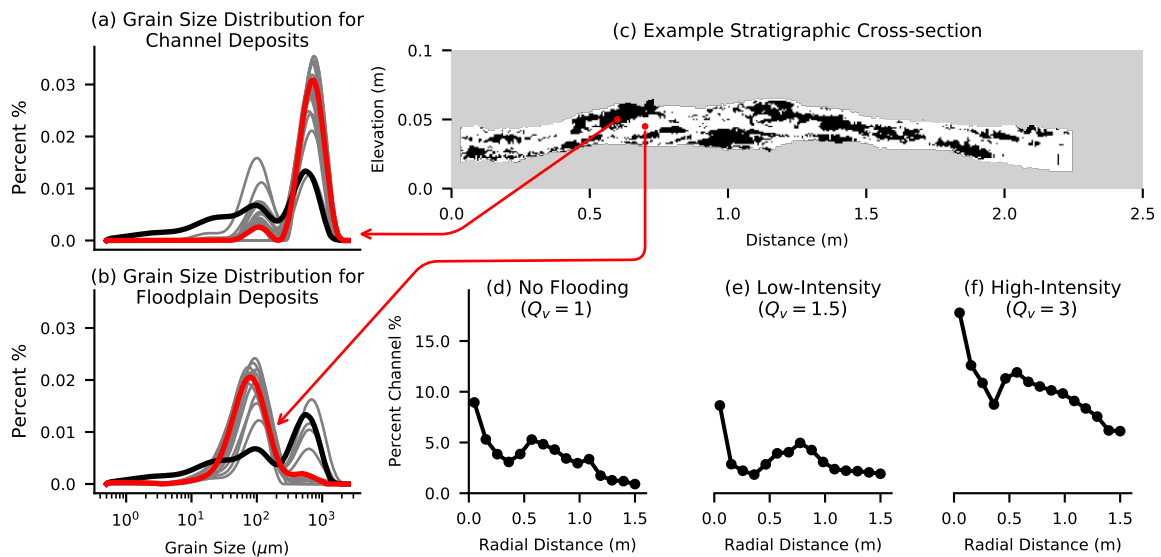


Figure 3.10: Shown in (a) and (b) are grain size distributions from channel and floodplain deposits identified in physical stratigraphic cuts, with an example sample highlighted in red for each facies. Also shown in black is the grain size distribution of the input sediment mixture. Shown in (d), (e), and (f) are the abundance of channel deposits in circular sections taken through the synthetic stratigraphy at several radii from the delta apex. All experiments show a general basinward fining, but channel facies are more abundant when $Q_v = 3$, least abundant when $Q_v = 1.5$ and intermediate when $Q_v = 1$.

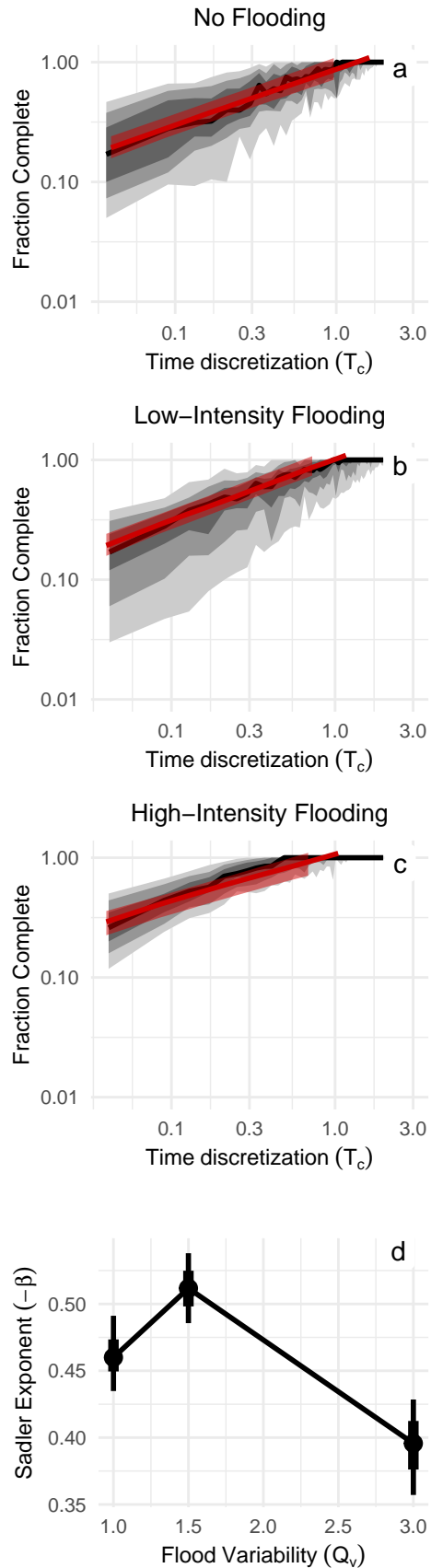


Figure 3.11: The power-law decay of stratigraphic completeness as a function of discretization timescale is shown for flooding intensity values of $Q_v = 1.0$, $Q_v = 1.5$, and $Q_v = 3.0$. The shaded regions show the distribution of the data binned for every value of δt , with the lightest band showing the 1st to 99th percentiles, the middle band showing the 10th to 90th percentiles, and the darkest showing the 25th to 75th percentiles. The binned median is shown as a black line. Model fits of Equation 3.14 are shown in red, with an 80% credible interval for the model predictions. Estimated posterior distributions for $-\beta$ are shown in panel d, where the median is shown as a point, and the 25th to 75th percentiles are shown as a thick line, and the 10th to 90th percentiles shown as a thin line.

3.3.3 Channel and delta floodplain morphology

Channel geometry scaled non-monotonically in response to increasing flooding intensity (Figure 3.12). When no flooding was present, channel slope was 2.66×10^{-2} on average. When low-intensity flooding was imposed, channel slopes shallowed substantially to 1.83×10^{-2} , but as flooding intensified such that $Q_v = 3$, channel slopes increased substantially to 2.69×10^{-2} . When no flooding was present, channels were 10.4 mm deep on average. When low-intensity flooding was imposed, channels deepened to 12.5 mm, but as flooding intensified such that $Q_v = 3$, channels shallowed to 8.89 mm deep. When no flooding was present, channels were 6.97 cm wide on average. When low-intensity flooding was imposed, channels narrowed to 5.78 cm wide, but as flooding intensified such that $Q_v = 3$, channels widened to 16.5 cm across (see Table 3.2).

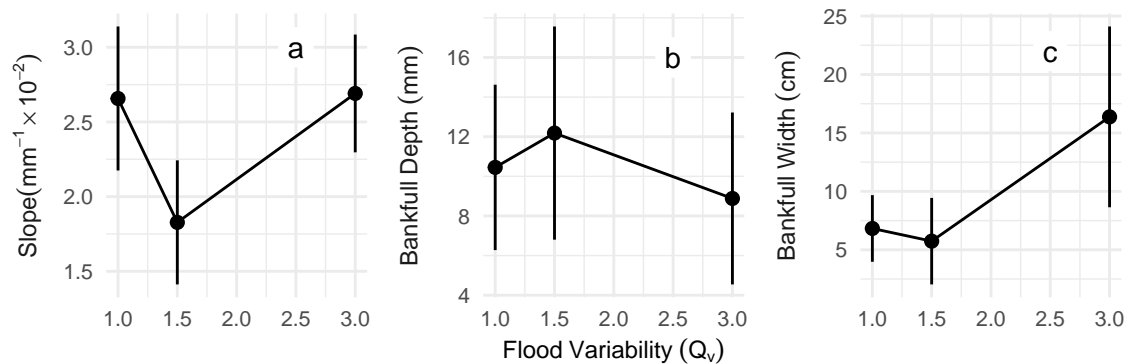


Figure 3.12: Channel geometry estimates across a gradient of Q_v . Points represent average values, and bars represent the mean \pm the standard deviation. Channel widths, depths, and slope all scale non-monotonically with Q_v .

When no flooding was present, floodplain relief averaged 4.87 mm. During low-intensity flooding, enhanced alluvial ridges were observed, with characteristic floodplain relief of 7.47 mm. In contrast, floodplain relief was diminished during high-intensity flooding, totaling 4.83 mm. Delta lobes at the shore grew with delivery of sediment from the river channels, creating a rugose shoreline. When no flooding was present, shoreline rugosity calculated using Equation 3.15, was 0.18. When low-

intensity flooding was imposed, shoreline rugosity increased to 0.356, whereas when flooding intensity increased to $Q_v = 3$, shoreline rugosity decreased to 0.137.

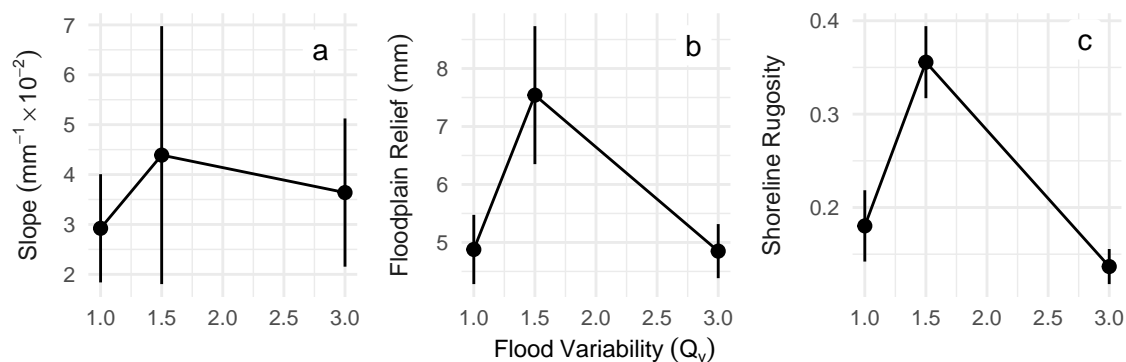


Figure 3.13: Delta morphology characteristics across a gradient of Q_v . Points represent average values, and bars represent the mean \pm the standard deviation. Floodplain roughness, shoreline rugosity, and floodplain slope all scale non-monotonically with Q_v .

3.3.4 Levee breach abundance

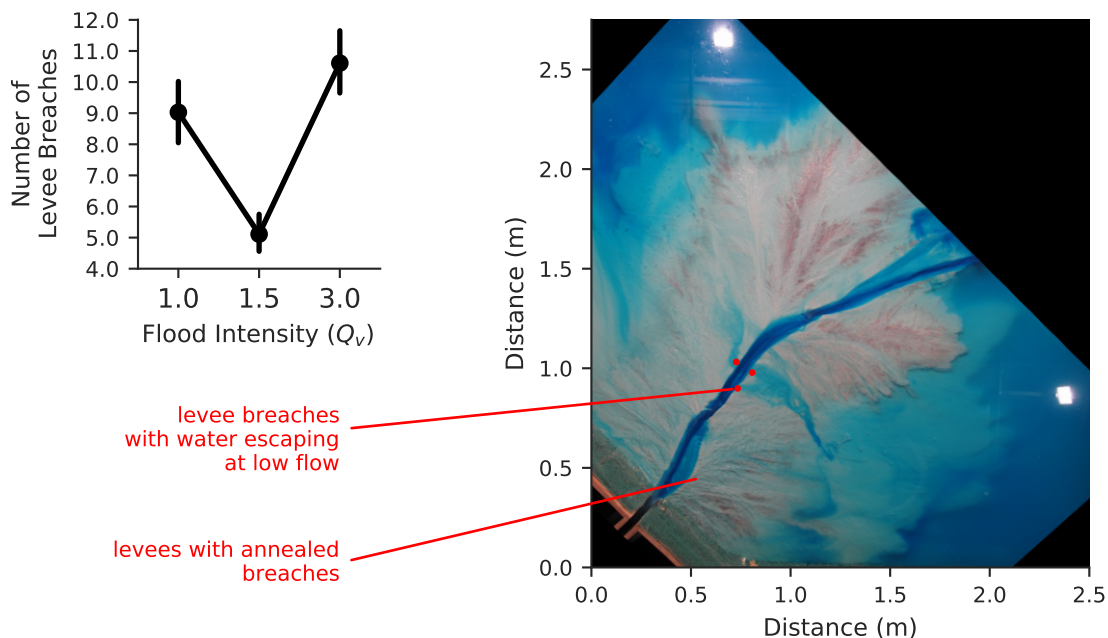


Figure 3.14: Counts of levee breaches across a gradient in flooding intensity. Levee breaches were most common during high-intensity flooding. Levee breaches were less abundant during low-intensity flooding as compared to either no flooding or high-intensity flooding. Shown is an example overhead image at low flow, where levee breaches were identified as locations where flow escaped from the channel to the floodplain. The location of levee breaches that annealed is also indicated.

Counts of levee breaches conducted in each hour of the experiment indicate that levee breaches are less abundant when flood intensity is low ($Q_v = 1.5$) as compared to no flooding or high-intensity flooding. As shown in Figure 3.14, an average of 9.03 levee breaches were active at any given hour when there was no flooding, and when flooding was intense ($Q_v = 3$), 10.6 levee breaches were active. In contrast, when flood intensity was low, only 5.11 levee breaches were active at any given time. These results were analyzed using an ANOVA with Poisson-distributed dispersion, yielding posterior estimates summarized in Table 3.2.

Table 3.2: Posterior estimates or maximum-likelihood estimates for observed delta parameters. Posterior estimates are given as the mean \pm standard deviation. *Estimates made with maximum-likelihood are given as mean \pm 95% confidence intervals.

	$Q_v = 1$	$Q_v = 1.5$	$Q_v = 3$
Channel Depth (mm)	10.4 ± 0.26	12.5 ± 0.402	8.89 ± 0.283
Channel Width (mm)	6.97 ± 0.21	5.78 ± 0.243	16.5 ± 0.509
Channel Slope ($m/m \times 10^{-2}$)	2.66 ± 0.014	1.83 ± 0.013	2.69 ± 0.011
Shoreline Rugosity ($—$)	0.18 ± 0.004	0.356 ± 0.004	0.137 ± 0.004
Delta Topset Roughness (mm)	4.87 ± 0.545	7.47 ± 2.86	4.83 ± 2.59
Delta Topset Slope ($m/m \times 10^{-2}$)	2.92 ± 0.03	4.37 ± 0.06	3.67 ± 0.03
Sediment Dispersal ($-\beta$)	0.462 ± 0.024	0.507 ± 0.028	0.391 ± 0.039
Channel Mobility (hrs)*	19.8 ± 1.44	23.9 ± 2.24	4.59 ± 0.244
Levee Breaches	9.03 ± 0.298	5.11 ± 0.226	10.6 ± 0.331

3.4 Floods and basin-scale morphodynamics

In this experimental apparatus, the main mechanism driving lateral channel mobility is avulsion. Visual observations from overhead imagery show that avulsions occurred in the experiments when channel banklines failed and subsequent erosion scoured a permanent crevasse splay, allowing water and sediment to flow onto the floodplain through the breach (Figure 3.14). Overbank flow is the result of sediment that accumulates in the channel and elevates the water stage above the levee crest. Thus, the key control on avulsion is the balance between in-channel aggradation, which desta-

bilizes the channel by increasing the probability of crevasses, and the propensity to build levees, which confine the flow and preclude avulsions.

Flooding intensity impacted both of these processes, and is shown in Figure 3.15, where the process of channel evolution is illustrated for two contrasting scenarios, namely $Q_v = 1.5$ and $Q_v = 3$. When flooding intensity is low, in-channel aggradation is balanced by levee aggradation (Figure 3.15; $A—A'$), which confines the flow and precludes avulsions, such that over the $1/2T_c$ depicted in the figure, the channel under low-intensity flooding was stationary. In contrast, rapid in-channel aggradation in the channel under high-intensity flooding outpaces levee aggradation (Figure 3.15; $B—B'$). This destabilized the channel and promoted a subsequent avulsion, which relocated flow to river right (Figure 3.15; $B—B'$).; This example serves to show a general result, which is that levee breaches were less abundant under low-intensity flooding, because sediment accreted to form levees and anneal breaches. When flooding was intense or absent, breaches became more common (Figure 3.14). It is this balance that drives impacts on channel mobility, delta sediment dispersal patterns, as well as channel geometries as a result of changing flood intensity.

Channel overlap e -folding times (Figure 3.7) show clearly that extreme flooding ($Q_v = 3$) promotes enhanced channel mobility, in keeping with existing evidence that flooding increases bank erosion, promoting avulsion and inhibiting levee growth (Esposito et al. 2018). Levee breaches are the nuclei for incipient avulsions, and elevated flood stages and flow velocities during peak flood conditions promoted bank erosion and scour that facilitated the avulsion process. This effect was paired with in-channel aggradation during interflood periods that primed overbank flows in the subsequent flood cycles (Figure 3.15). Combined, these processes promoted frequent avulsions, and intensified channel mobility.

In contrast, our results indicate that moderate levels of flooding ($Q_v = 1.5$)

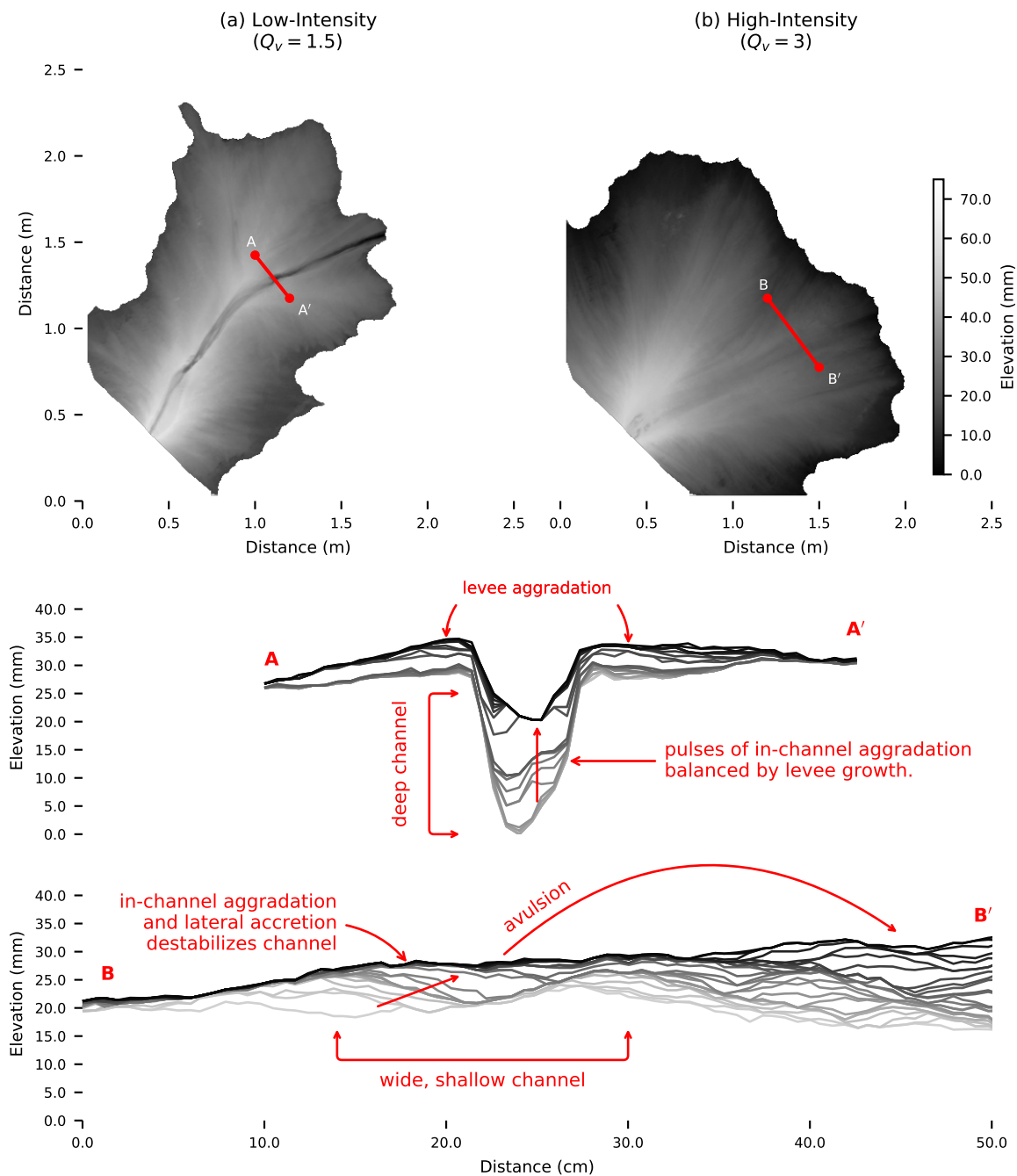


Figure 3.15: Topographic maps of two example stratigraphic surfaces are shown in (a) and (b), with transects marked $A-A'$ and $B-B'$. Transects are shown in the corresponding lower panels. Shown in gray lines are successive stratigraphic surfaces, demonstrating sediment deposition patterns. Darker surfaces are younger, and lighter surfaces are older. Note that in transect $A-A'$, initial channel scouring is followed by subsequent in-channel aggradation, which would lead to avulsion except for the fact that levee aggradation confines the channel, and restricts it to one location. In contrast, transect $B-B'$ shows initial levee aggradation, but levee development does not continue, and in-channel aggradation forces an avulsion to river right.

inhibited channel mobility. Whereas high-intensity floods appear to limit the development of long-lived levees, low-intensity flooding clearly promotes long-term levee construction (Figure 3.8). Moderate floods ensured that sediment was delivered to channel margins during overbank conditions, and waning overbank flow velocity on the falling limb resulted in sediment deposition adjacent to the channel margin (Figure 3.15). Sediment supplied to channel margins thus contributed to channel confinement, by annealing levee breaches and forestalling incipient avulsions (Figure 3.14). However, when flow is steady ($Q_v = 1$), levee breaches are subjected to continuous overbank flow with no rising or falling limb, thus reducing the probability breaches will silt and anneal. In this way, moderate flooding stabilizes levees, and in so doing, limits channel mobility relative to both the high-intensity flooding and the no flooding condition, producing a non-monotonic scaling relationship (Figures 3.7).

Levee breaching also impacts the extent of inundation and sediment dispersal across the delta topset, thereby affecting accumulation patterns. The evidence indicates that across a gradient of flooding intensities, sediment dispersal patterns exhibit non-monotonic behavior, just as with channel mobility. When no flooding is present ($Q_v = 1$), fluvial morphologies and kinematics equilibrate to time-averaged sediment flux and aggradation conditions. An incremental increase in flood amplitude to $Q_v = 1.5$ stabilized channels and confined flow, which restricted floodplain sediment deposition to the area immediately adjacent to the channel. Thus, moderate flooding focused sediment transport downstream to the channel mouth, which prograded delta lobes and led to uneven sediment package thickness and a rugose shoreline (Figure 3.8). A further increase in flood amplitude to $Q_v = 3$, however, produced the opposite response. By driving frequent avulsions through levee breaches, high-intensity flooding resulted in extensive lateral sediment dispersal. Sediment packages in the high-intensity flooding experiment were evenly distributed across the delta topset, in contrast to both the no-flooding condition as well as the low-intensity flood

condition (Figures 3.8 and 3.11).

The non-monotonic style of fluvial sediment dispersal impacted floodplain topography and channel geometry. During high-intensity flooding, frequent avulsions evenly spread sediment across the delta topset, which resulted in muted floodplain roughness (Figure 3.13). Furthermore, because channels were short-lived due to the frequency of avulsions, basinward progradation of delta lobes was inhibited, and shoreline rugosity was diminished (Figure 3.13). In contrast, during low-intensity flooding, stable channels limited lateral sediment dispersal, and focused deposition adjacent to the channel, thus accentuating floodplain roughness (Figures 3.8 and 3.11). With restricted mobility, channels under low-intensity flooding acted as conduits to transport sediment to the shoreline, promoting lobe progradation and enhanced shoreline rugosity (Figure 3.13). Levee-building processes are also reflected in channel geometries, which also display non-monotonic scaling with flood intensity (Figure 3.12). Enhanced erosion of levees and frequent avulsion during high-intensity flooding leads to the formation of broad, shallow channels. Sustained levee aggradation during low-intensity flooding produces relatively deep, narrow channels. Intermediate levee-building under constant flow thus resulted in channels of intermediate dimensions (Figure 3.12). Taken together, these results suggest that the propensity of levee breaches to either anneal or escalate into avulsion is an important but overlooked aspect of fluvial morphodynamics that fundamentally changes predictions of landscape evolution under variable flow.

When attempting to infer alluvial dynamics from the geologic record (e.g. Chapter 2), the distinction between channel deposits and overbank deposits, their relative abundance and spatial relationships form the crux of the process interpretation. These deposits are most clearly recognized by changes in grain size. For example, variation in the abundance of coarse versus fine grains have been interpreted to reflect changes in boundary conditions like enhanced mountain uplift or changes in base

level (Heller and Paola 1992, e.g.). However, the expression of a given stratigraphic exposure may have several plausible root causes, and so detailed observations of sedimentary structures are needed to distinguish between them. Various metrics and facies associations have been proposed as diagnostic of alluvial systems experiencing extreme floods (e.g. Plink-Björklund 2015), but in general, the specific mechanisms by which changes in flood intensity are expressed in the strata have remained underconstrained. This study: (1) identifies levee-building as a definitive mechanism governing the spatial allocation of grain sizes and sediment in fluvio-deltaic systems undergoing variable flow, and (2) demonstrates that this mechanism is responsible for non-monotonic dynamics across a gradient in flooding intensity. Thus, stratigraphic interpretations of flooding intensity from field outcrops should target levee deposits as the main focus for inferring the level of flooding intensity.

Moreover, the non-monotonic behavior suggests that changes in flooding may manifest differently depending on whether the current level of flooding is above or below the optimum for levee construction. For example, the Piceance Basin (Chapter 2) was likely characterized by low-intensity flooding during Atwell Gulch time prior to the PETM. The transition in flooding during the PETM destabilized Piceance rivers, by driving overbank flow and crevassing. This likely indicates that enhanced flooding during the PETM pushed flood intensity beyond the optimum condition for levee construction in the Piceance floodplain. However, another basin may have a different response. For example, if intensified flooding in another basin brought the system state closer to its optimum levee condition, channels may have stabilized instead.

This aspect of the response is also relevant for projections of future climate change. Changes in precipitation due to global warming are expected to result in enhanced flooding in some regions and diminished flooding in others. This study suggests that the fluvial response will depend on the system state relative to the levee-building optimum. In regions where the flood intensity is below the optimum

level for levee construction, enhanced flooding may cause future channel stabilization. On the other hand, a counterintuitive implication is that if flood intensity in a region is at or below its optimum for levee-building, a decrease in flood intensity may, in fact, destabilize channels.

3.5 Summary

Variable flow is a natural condition for all river channels, yet its impacts on fluvial morphodynamics are difficult to predict. This study evaluated the impact of flooding intensity on fluvial dynamics using a set of three physical experiments that spanned a gradient of flood intensity (Q_v). In each experiment, the time-averaged sediment and water flux were held constant while channel mobility, sediment dispersal, and landscape morphology were observed.

When no flooding was present ($Q_v = 1$), channels were flanked by discontinuous levees, which restricted channel mobility and produced a characteristic width and depth. Levee breaches, crevassing and avulsion events were the primary mechanisms to deliver sediment to the floodplain, building delta lobes and producing a rugose shoreline.

When low-amplitude floods ($Q_v = 1.5$) were imposed, sediment was consistently delivered to levee crests with every flood cycle. As a result, levee breaches tended to anneal over successive flood waves, and channels deepened and narrowed, while cohesive channel banks severely decreased channel mobility. Tall levees confined flow and restricted the locus of deposition to areas immediately adjacent to the channel margin and lobes at the delta shoreline. The outcome of this was to enhance shoreline rugosity, lower channel slopes, and construct substantial floodplain relief.

However, when flood amplitude increased to $Q_v = 3$, vigorous overbank flow

advected sediment beyond channel margins, exacerbating existing levee breaches, and increasing the avulsion frequency. This process inhibited levee aggradation and promoted enhanced bank erosion, which created wide, shallow channels characterized by rapid planform mobility. Low channel margins primed the system for substantial overbank flow, and promoted lateral sediment dispersal across the delta topset. Floodplain relief decreased as a result of even sediment deposition, and enhanced channel mobility precluded the development of long delta lobes. Combined, these processes produced higher channel slopes and lower shoreline rugosity.

Taken together, these observations of fluvio-deltaic morphologies and kinematics show that surface processes and sediment dispersal scale non-monotonically across a gradient of flooding intensities. Flooding induces a morphodynamic feedback in the fluvial system, where flood amplitude determines the inundation extent, thereby altering erosion and deposition patterns and shaping fluvio-deltaic morphology, which in turn impacts overbank flow. Levees are the lynchpin of this feedback, governing sediment exchange between channels and adjacent floodplains. Below a threshold of flood amplitude, marginal increases in flood intensity stabilized levees, whereas above the threshold, a marginal increase in flooding intensity destabilized levees. Our results indicate that the optimum lies somewhere between $Q_v = 1$ and $Q_v = 3$, and demonstrate that deviation from the optimum levee construction condition induces a cascade of impacts on fluvial dynamics across scales. Importantly, since each experiment was run with the same equivalent steady discharge, these results suggest that in fan deltas with variable flow, levee construction processes are required to accurately predict landscape evolution and interpret fluvio-deltaic stratigraphy.

Chapter 4

Paleoclimate Bias due to Transitions in Flooding

Abstract

Many of the best geologic analogues for contemporary climate change, like the Paleocene-Eocene Thermal Maximum, are recorded only by biogeochemical proxies embedded in the stratigraphic record. However, sediment accumulation is an unfaithful recorder, characterized by hiatuses and erosion. This makes it difficult to determine the duration and magnitude of past climate change events with confidence. Moreover, climate can modulate both the average rate of sedimentation and its temporal variability, i.e. steadiness. This implies that the fidelity of the stratigraphic record can change in tandem with climate events, injecting unaccounted-for uncertainty into climate reconstructions. To explore this issue, this study examines the preservation potential for climate events in stratigraphy built by experimental fan deltas that were subjected to transitions in flood intensity. The intensity of floods alters sediment dispersal patterns, thereby impacting the rate and steadiness of sediment accumulation. Over the duration of the experiment, climate events were simulated by toggling flooding intensity between a high and a low value, while varying the duration of each transition. Transitions induced landscape disequilibrium, which was more severe for abrupt transitions versus gradual ones. The recovery from landscape disequilibrium was marked by contrasting sediment dispersal patterns depending on the sign of the transition. Transitions from low- to high-intensity flooding (*positive* sign) promoted transiently rapid sedimentation across a large area to repave the surface. This enhanced the fidelity of the proxy record, and dilated the perceived duration of the climate event in the strata. In contrast, transitions from high to low-intensity flooding (*negative* sign)

were marked by localized deposition, which generated transiently slow sedimentation. As a result, this reduced the fidelity of the stratigraphic record and compressed the perceived duration of the climate event. Thus, climate change events like the PETM impact the fidelity of the stratigraphic record in real time, altering the preservation potential for paleoclimate proxies through landscape disequilibrium and hysteresis. This has the potential to cast uncertainty onto paleoclimate reconstructions, and also fundamentally bias interpretations.

4.1 Reconstructing climate from strata

Accurate predictions of future climate change are grounded in a clear reckoning of Earth history, which hinges on precise paleoclimate reconstructions spanning a broad range of geologic time. Periods of abrupt, intense climate change in the geologic past, such as the onset of the Paleocene-Eocene Thermal Maximum (PETM) (Kennett and Stott 1991, Chapter 2), serve as analogues to contemporary conditions (McInerney and Wing 2011), but the magnitude and duration of such events are challenging to resolve in stratigraphy because the record is incomplete (Trampush and Hajek 2017). In fact, there are many substantive discrepancies between paleoclimate records of the PETM, and key aspects of this event remain disputed or unclear (McInerney and Wing 2011). Part of the uncertainty arises due to the biogeochemical pathways by which climate proxies are fixed in the host strata, including problems related to time averaging (Gocke et al. 2010), chemical kinetics (Baczynski et al. 2016), and/or source-material mixing (Farquhar et al. 1989). These uncertainties can be managed with strategic sampling and careful site selection, but the fundamental limit on proxy record resolution is the presence or absence of sediment accumulation (Trampush and Hajek 2017).

It is established practice to construct age models for stratigraphic sections by

linearly interpolating between horizons of known age, identified by biostratigraphy or radiogenic isotopes (e.g. Westerhold et al. 2009). This method implicitly assumes that sediment accumulation is steady and uniform between horizons (Abels et al. 2010). However, in nearly all depositional environments, sediment accumulation is stochastic because autogenic dynamics focus erosion and deposition in some regions of the basin while other areas receive no sediment (Ganti et al. 2011; Straub and Foreman 2018). The locus of deposition moves over time via processes including channel avulsion, migration, and lobe switching, such that even closely-spaced stratigraphic sections can represent different sediment accumulation histories (Ganti et al. 2011; Straub et al. 2012). In the stratigraphic record, hiatuses are often imperceptible, and chronostratigraphy may lack the resolution to clearly identify expanded or condensed sections (Sadler 1981). In this way, autogenic dynamics control the statistics of erosion and deposition, with the best-case scenario for paleoclimate proxy fidelity being high sedimentation rates paired with low variability (Trampush and Hajek 2017; Foreman and Straub 2017).

A consequence of this is that lengthier climate events have greater taphonomic potential. For example, in deltas, river channels focus short-term sediment deposition to build delta lobes, but over longer timescales, lobes compensate for uneven deposition by avulsing to new locations (Straub et al. 2009). The compensation timescale (Equation 3.5) sets a natural threshold that climate signals must surpass in order to be transferred faithfully to the stratigraphic record (e.g. Foreman and Straub 2017). Climate events that persist longer than the compensation timescale are likely to be preserved in all stratigraphic sections because sediment is dispersed evenly across the delta topset (Li et al. 2016).

This conceptual framework presupposes that the lengthscales and timescales of autogenic dynamics are intrinsic properties of the sedimentary system, and moreover, it is also generally assumed that the statistics of erosion and deposition are station-

ary through time (Trampush and Hajek 2017; Jerolmack and Paola 2010; Toby et al. 2019). These assumptions are unrealistic, however, because it is known that autogenic dynamics are modulated by external boundary conditions like sediment supply (Bryant et al. 1995), base level rise (Muto 2001), and hydrograph variability (Esposito et al. 2018, and Chapter 3). For instance, all else being equal, a high-variability hydrograph at equilibrium is characterized by high channel mobility, lateral sediment dispersal, and a low-relief landscape. In contrast, a low-variability hydrograph inhibits channel mobility, restricts lateral sediment dispersal, and creates high-relief landscapes with substantial surface roughness. Sedimentological evidence from many fluvial basins suggests that the onset of the PETM exemplifies a transition from low to high hydrograph variability (Foreman et al. 2012; Chen et al. 2018, also see Chapter 2). This implies that autogenic dynamics varied throughout the PETM interval, and therefore that the resolution of the paleoclimate record itself may, in fact, covary with the climate. However, this implication remains untested, and it is unclear how to interpret paleoclimate proxy fidelity under such circumstances. To address this knowledge gap, the present study uses sedimentary experiments to explore how autogenic fluvial dynamics coëvolve with abrupt changes in hydrograph variability, and evaluate proxy fidelity and preservation bias in the resulting stratigraphy.

4.2 Methods

4.2.1 Experimental design

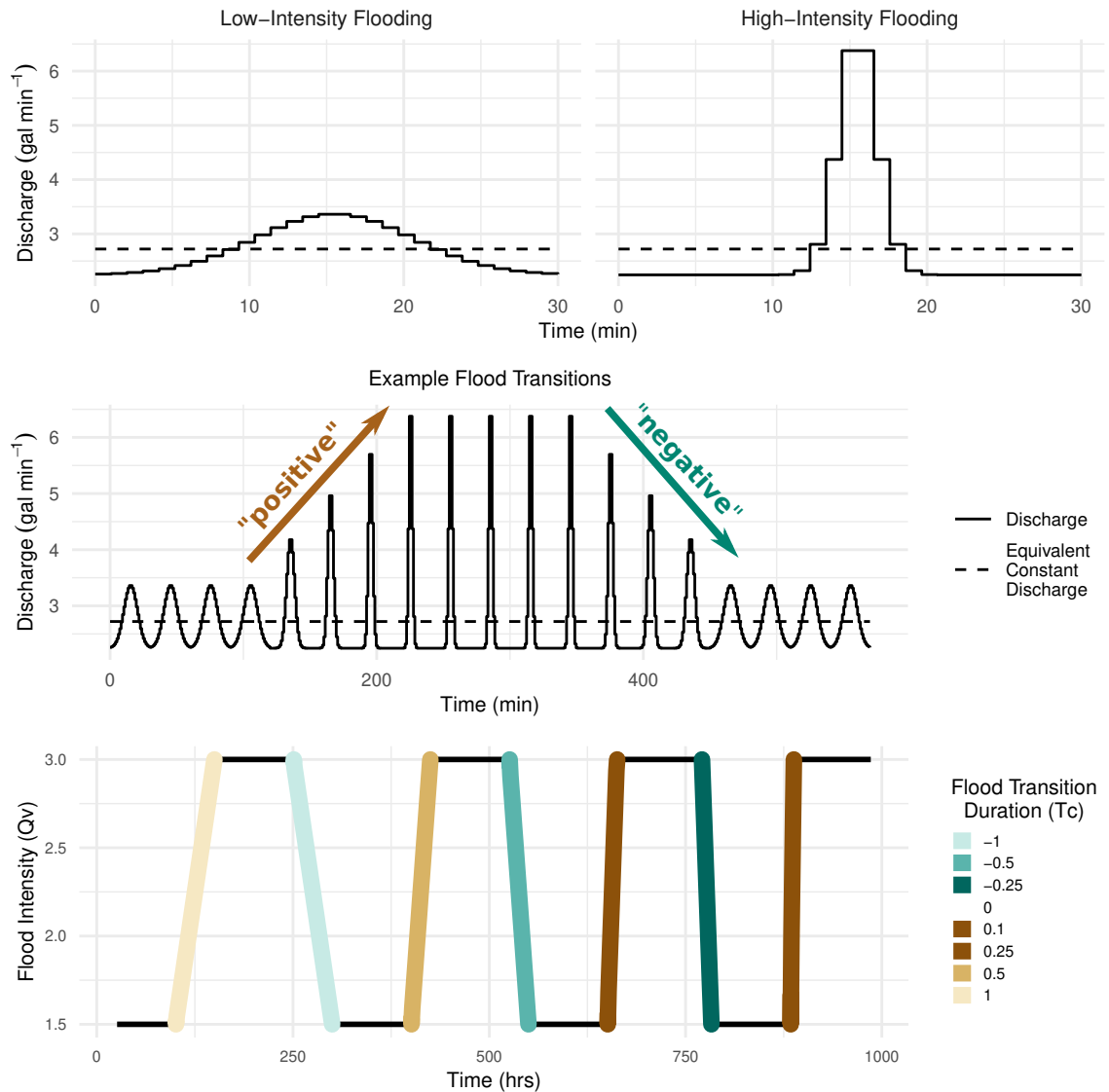


Figure 4.1: Two flood states are chosen, low-intensity flooding where $Q_v = 1.5$, and high-intensity flooding, where $Q_v = 3$. Transitions were engineered between the two states, where the duration of the transition varied. During each transition, flood waves were linearly scaled using Equation 3.4, such that flood intensity smoothly varied. Transitions from low-to-high flooding intensity are termed positive, and transitions from high-to-low are termed negative. Seven transitions were engineered over the experimental run, with different duration. The most abrupt occurred over $1/10T_c$ whereas the most gradual occurred over $1T_c$. Stasis periods of duration $2 \times T_c$ were placed between each transition to allow the system to re-equilibrate.

The impact of changing flood conditions on sedimentary dynamics was tested with a physical fan delta experiment conducted at the Tulane University Sediment Dynamics Laboratory, using the same apparatus described in § 3.2.1. Using the same sediment mixture as in Chapter 3, a constant ratio of sediment and water were mixed and fed into the basin via the inlet channel to form a delta, while long-term aggradation was induced by steadily raising the water level throughout the experiment.

Hydrograph variability was simulated by imposing a periodic function of water and sediment discharge at the delta apex (Equation 3.4), and each flood cycle had a duration $T_f = 30$ minutes; giving ~ 100 floods per T_c . In this way, flood magnitude and intermittency were allowed to smoothly covary and produce different levels of flooding intensity, (Q_v , Equation 3.2), while holding a constant equivalent steady discharge (\bar{Q}_c , see § 3.2.1)

The experiment toggled between two levels of flooding intensity: low-intensity flooding ($Q_v = 1.5$) and high-intensity flooding ($Q_v = 3$). Over a total experimental run of 987 hours, four low-to-high (*positive*) transitions and three high-to-low (*negative*) transitions were completed. Throughout, positive transitions are denoted as T_i^+ and negative transitions are denoted T_i^- where i is an index identifying each transition (Table 4.1). Between each transition, sufficient time elapsed such that dynamic equilibrium was restored ($2 \times T_c$). To investigate the impact of abrupt versus gradual hydrologic change, each transition occurred over a specified duration. The most gradual transition occurred over $1 \times T_c$, while the most abrupt occurred over only $1/10 \times T_c$. In total, the experimental run was composed of seven transitions and eight stasis periods. The parameters for each stage of the experiment are given in Table 4.1.

Table 4.1: Control parameters for Tulane University Delta Basin for experiment with seven transitions in flood intensity. Two effects were analyzed: (1) the duration of flood transitions, and (2) the sign of transitions. Basic parameters, like the sediment concentration and water level rise rate are equivalent between this experiment and the one described in Chapter 3. For visual representation of transitions during runs, see Figure 4.1. *Estimated from Li et al. (2016).

T_1^+	$(Q_v = 1.5 \rightarrow Q_v = 3)$	$1 \times T_c$
T_2^-	$(Q_v = 3 \rightarrow Q_v = 1.5)$	$1 \times T_c$
T_3^+	$(Q_v = 1.5 \rightarrow Q_v = 3)$	$0.5 \times T_c$
T_4^-	$(Q_v = 3 \rightarrow Q_v = 1.5)$	$0.5 \times T_c$
T_5^+	$(Q_v = 1.5 \rightarrow Q_v = 3)$	$0.25 \times T_c$
T_6^-	$(Q_v = 3 \rightarrow Q_v = 1.5)$	$0.25 \times T_c$
T_7^+	$(Q_v = 1.5 \rightarrow Q_v = 3)$	$0.1 \times T_c$
Low-intensity flood discharge (L/s)		0.213
High-intensity flood discharge (L/s)		0.426
Baseline discharge (L/s)		0.142
Equivalent constant discharge (L/s)		0.172
Sediment concentration (lb/L)		0.005
Water level rise (mm/hr)		0.25
Flood cycle time (T_f , min)		30
Compensation time scale (T_c , hours)		$\sim 50^*$
Run time (hrs)		987

4.2.2 Data collected

For every hour of runtime, topographic data were collected using a terrestrial lidar scanner. The 3D point-cloud data were then gridded at a horizontal resolution of 5×5 mm with a vertical resolution of 1 mm. Rarely, a topographic scan failed ($\sim 0.2\%$ of all scans), and some analysis of scan data can be biased by gaps in the record, so the missing data was interpolated on a pixel-by-pixel basis using the closest complete scans before and after. Topographic scans were then clipped to the basin water level, and used to generate masks of the delta topset and identify the shoreline.

Sequential scans were post-processed to generate synthetic stratigraphy, where only topographic information that represents permanent sediment accumulation is retained. Two methods were used; in the first, each topographic surface was clipped to reflect subsequent erosion such that only the minimum elevation is preserved in

each surface, and successive surfaces are collapsed to the lowest bounding surface (Strong and Paola 2008). In the second method, eroded surfaces are masked, such that the amount of missing deposition is represented by missing data, rather than by transforming stratigraphic surfaces.

4.2.3 Quantifying stratigraphic bias

Each transition in flood intensity in this experiment was imposed externally by changing boundary conditions. As such, the value of flooding intensity itself can be cast as a paleoclimate signal “preserved” in the stratigraphic column. This is directly analogous to paleoclimate reconstruction from real stratigraphic records, be they from cores or outcrop exposures, where samples for paleoclimate proxy analysis are spaced evenly along the stratigraphic section. Without detailed age constraints, the best assumption available is to use a linear sedimentation age model between known age control points (Foreman and Straub 2017), but because deposition is stochastic, samples taken evenly in space are not distributed evenly through depositional time (Schumer et al. 2011).

Synthetic paleoclimate records were constructed for each flood transition using a random selection of 1D vertical stratigraphic columns spanning the interval of interest, that were taken from circular sections at evenly spaced intervals from delta apex to shoreline. An example of this process for two selected columns is shown in Figure 4.2, one for a positive transition (T^+) and the other for a negative transition (T^-). Erosion and deposition at every hour are shown for each column, as is the trajectory of the surface elevation through time. Using the flood intensity value itself as the fictive paleoclimate proxy, each stratigraphic column was sampled evenly in space from bottom to top, with the age of the top and bottom surfaces used to construct a linear age model for the section. Then, values of flood intensity were sampled using

the stratigraphic column to produce a profile of Q_v with respect to the perceived depositional time (black line) and the true depositional time (gray line). To evaluate the fidelity of paleoclimate records with coëvolving fluvio-deltaic stratigraphy, the perceived duration of the flooding transition was calculated for each synthetic paleoclimate record, and the perceived duration was then compared to the true transition time with a random-effects ANOVA fit using MCMC methods, where the random effect is the section radius (§ A.3.1). Since the columns were taken from a circular section, each at a different distance from the apex, estimates must be evaluated from

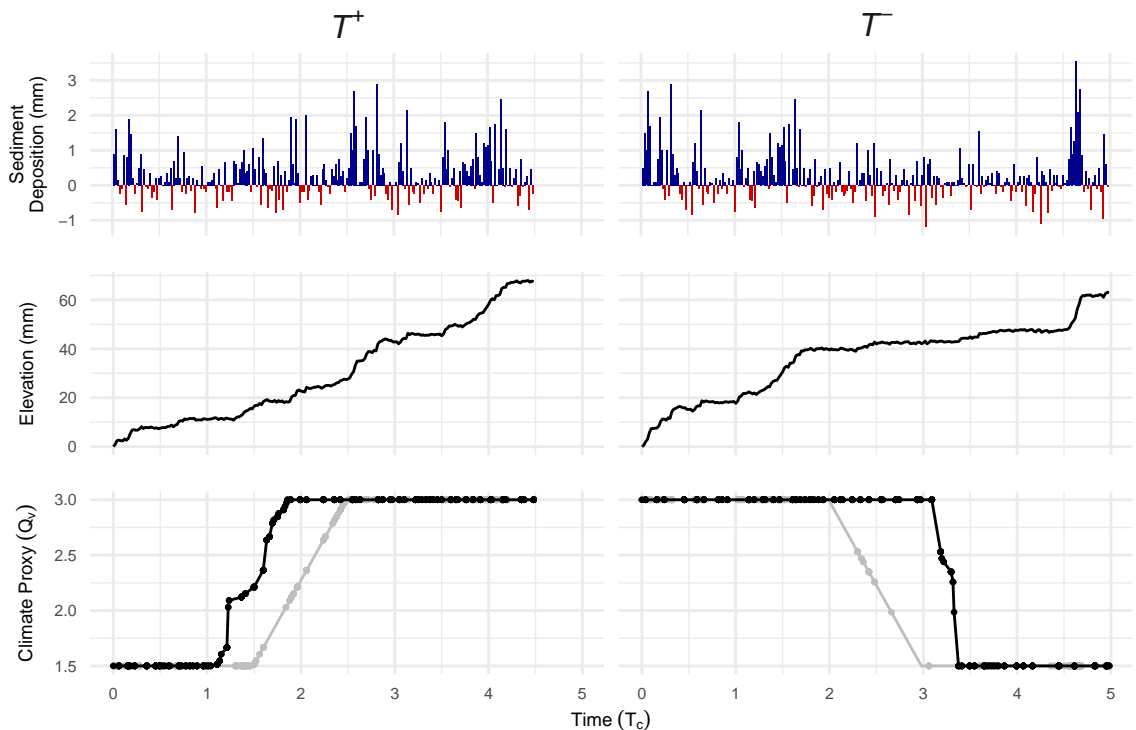


Figure 4.2: Shown is an example of uneven temporal sampling in the stratigraphic record for positive and negative transitions. Two random vertical columns were extracted from the topographic datasets, and the erosion and deposition for every hour of the experiment during a positive and negative transition was computed, and shown as a time series of red and blue bars, where red is erosion and blue is deposition. Using this data, the elevation trajectory of the surface is constructed throughout the transition in flooding (middle panels). Note that the accumulation of sediment is not steady, but instead is marked by periods of rapid accumulation and periods of relative stasis. These data are used to construct a synthetic stratigraphic column, which is sampled evenly from bottom to top, and a linear age model is assumed between the age at the top of the column and the age at the bottom. Then, these evenly spaced vertical samples are used to reconstruct the intensity of flooding through each transition. Because the accumulation of sediment is unsteady, these samples do not accurately capture the timing of the transition.

each section to characterize the overall effect, since sediment distribution patterns at the delta apex differ from those at the shoreline.

4.2.4 Quantifying sedimentation statistics and autogenic dynamics

To characterize the rate and variability of sedimentation, deposition and erosion data were taken from each flooding transition using the same set of randomly selected columns. The mean accumulation rate and standard deviation were then calculated for each column and compared between transition events. The differences were modeled using a random-effects ANOVA fit via MCMC sampling, to characterize the mean sedimentation rate as well as the steadiness during each transition (§ A.3.2 and § A.3.3). Additionally, the effect of the mean accumulation rate and variance on stratigraphic bias were also evaluated using a linear model with random-effects fit using MCMC sampling, again with radius as the random effect (§ A.3.4).

It is infeasible to measure the impacts of abrupt change by characterizing the statistics of autogenic dynamics directly, because it would be necessary to observe surface processes evolve for long periods of time. Instead surface roughness was calculated for each run hour. High-intensity flooding is associated with low topographic relief and even sediment dispersal, whereas low-intensity flooding is marked by high topographic relief and uneven sediment dispersal (see § 3.2.5). Thus, surface roughness can be used as an indicator for autogenic dynamics, and mechanistically explain trends in stratigraphic bias. Topographic surfaces were detrended along radial transects from the delta apex to the shoreline to remove the long-wavelength conical shape of the delta. The characteristic surface relief was then calculated as the difference between the 90th and 10th percentiles of the elevation distribution (Figure 3.6).

So long as boundary conditions are constant, dynamic equilibrium is established in the experimental basin over long timescales ($> 1 \times T_c$), and surface rough-

ness attains a quasi-steady value that varies around a consistent mean. Equilibrium surface roughness values for each flooding extreme were estimated by averaging over two $1 \times T_c$ segments of the experiment separated from the nearest transition by $1 \times T_c$. Disequilibrium surface roughness following transitions was then quantified by averaging over a 10-hour segment immediately following each transition. A 10-hour window was chosen to be long enough to average over short-term fluctuations in roughness but short enough to serve as a snapshot of the system state, and not encompass drift due to fluvial system responses to boundary conditions (Figure 4.8).

Finally, to directly quantify the evenness and extent of sedimentation, sediment accumulation maps were constructed for a 10-hour interval immediately following each transition. Observing sediment distribution for an equivalent amount of time after each transition reveals important aspects of the sedimentary response to the transition, thus characterizing the recovery of autogenic dynamics following a perturbation. The extent of sedimentation was determined as the area which accumulated more than 2 mm of sediment over the 10-hour segment, and the variability in the package thickness was characterized as the difference between the 90th and 10th percentiles of the isopach.

4.3 Results

4.3.1 Stratigraphic preservation bias

The perceived duration of transitions in flooding intensity was calculated by reconstructing the record of flooding intensity based on the preserved sediment using a linear age model (Figure 4.2). The perceived duration depends on both the abruptness of the event, as well as its sign (+ vs -). For each transition event, Figure 4.3 demonstrates the true climate event curve in color compared to an ensemble of re-

constructed climate events from the preserved stratigraphy in gray.

Two observations are evident from these ensembles. First, the preserved climate records appear to systematically lead the true event timing during positive transitions, and lag the true event during negative transitions; this effect is stronger for gradual transitions, and weaker for abrupt transitions. Second, the duration of flood transition events appear to be compressed for negative transitions and extended for positive transitions. The normalized difference between the true event duration

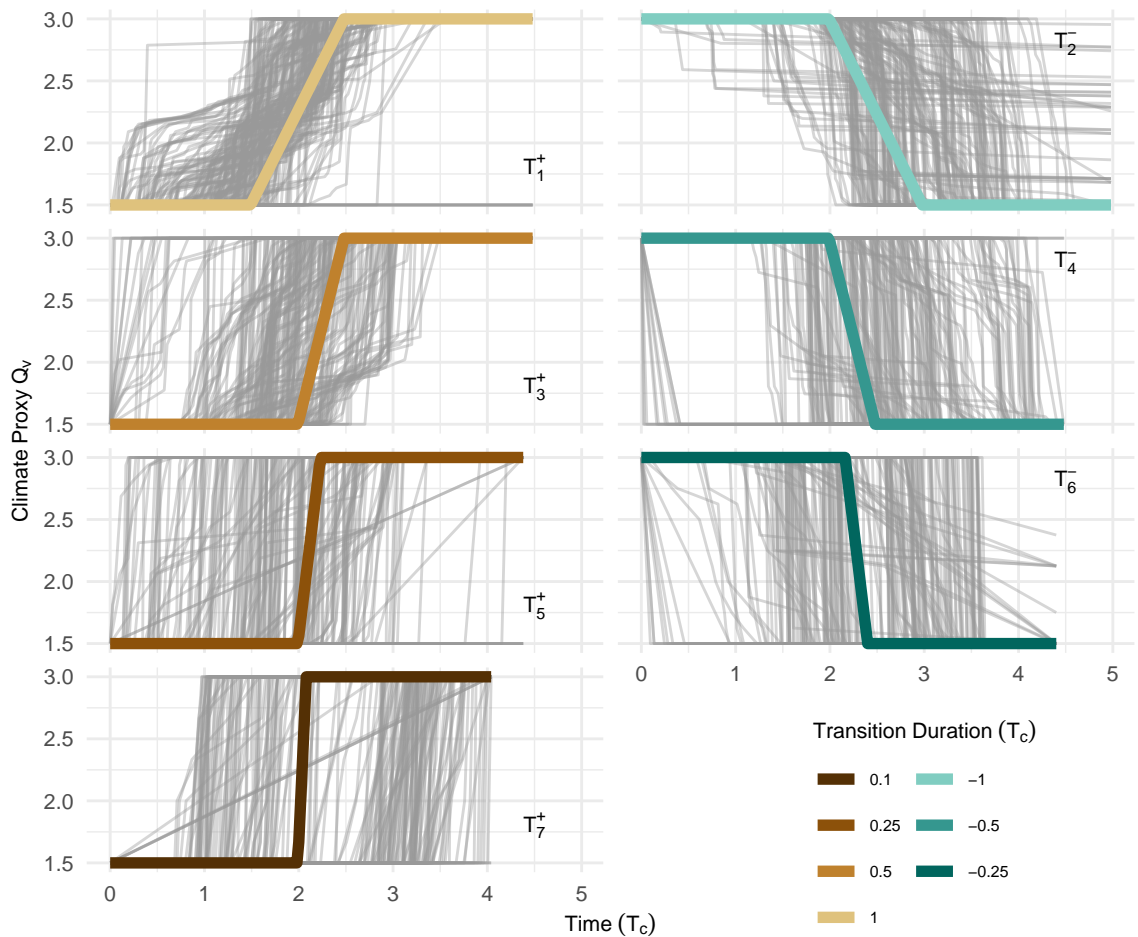


Figure 4.3: Each flooding transition is shown in the thick colored line with respect to nondimensional time units relative to T_c . The reconstructed “climate” records of each flooding transition is shown in gray for an ensemble of 100 randomly selected vertical columns in the same way as Figure 4.2. In general, an individual column poorly predicts the real pacing or timing of the flooding transition. Additionally, reconstructions of the flooding transition onsets from the ensembles appear to lead the real transitions for positive transitions, but lag for negative transitions, however the effect is unclear for abrupt transitions.

and the perceived event duration is termed the “bias,” and is calculated for each ensemble and plotted in Figure 4.4.

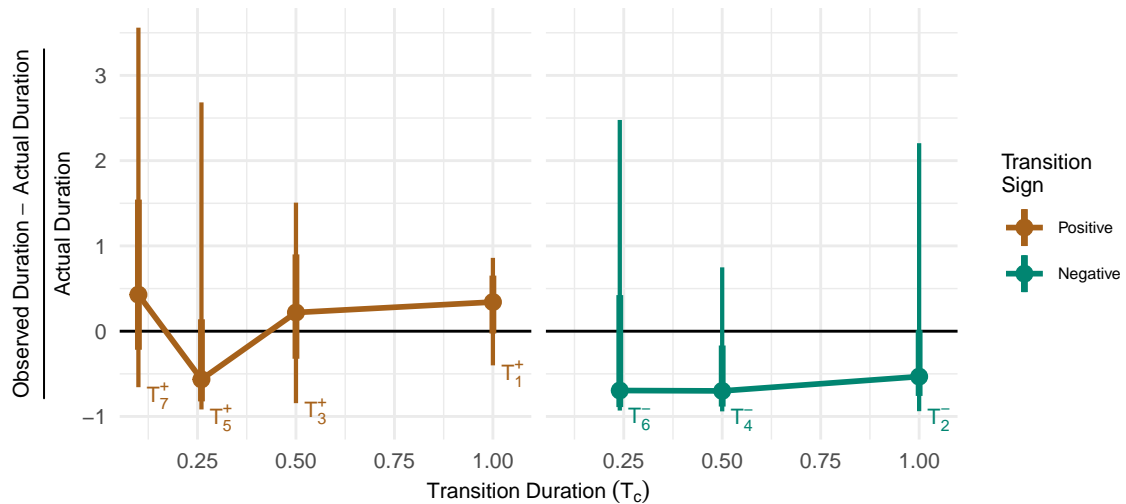


Figure 4.4: The normalized difference between the perceived transition duration and the actual duration of the transition is shown for 100 randomly selected vertical columns for each transition. The median is shown by a point, the 25th to 75th percentiles are shown by a thick vertical line, and the 10th to 90th percentiles is shown by a thin line. In general, the reconstructed duration of climate transitions is longer than the true value for positive transitions, and shorter for negative transitions, and there is no obvious trend with duration.

In general, records of positive transitions consistently overestimate the true length of the transition event. This is evident in Figure 4.4, where the difference between perceived duration and true duration is, on average, approximately 25% longer than the true duration. In contrast, records of negative transitions consistently underestimate the length of the event. This is evident in Figure 4.4, where the differences between the perceived duration and true duration are generally close to 75% shorter than the true duration.

4.3.2 Sedimentation statistics

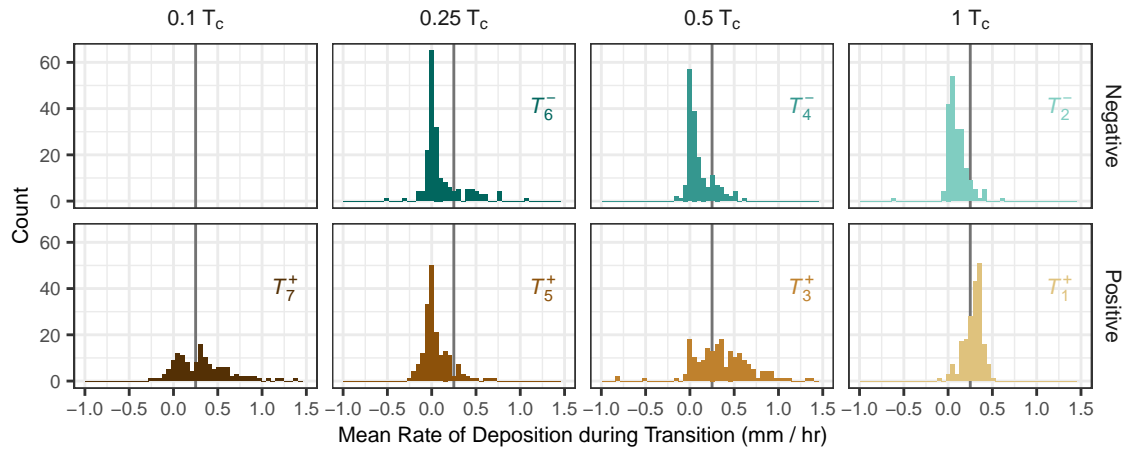


Figure 4.5: Histograms of the mean accumulation rate for 100 random columns during each transition. Negative values indicate erosion on average, and the vertical line is the water level rise rate, which sets the long-term pace for sediment accumulation. Note that mean sediment accumulation rates cluster around 0 for negative transitions, and often exceed the long-term average for positive transitions.

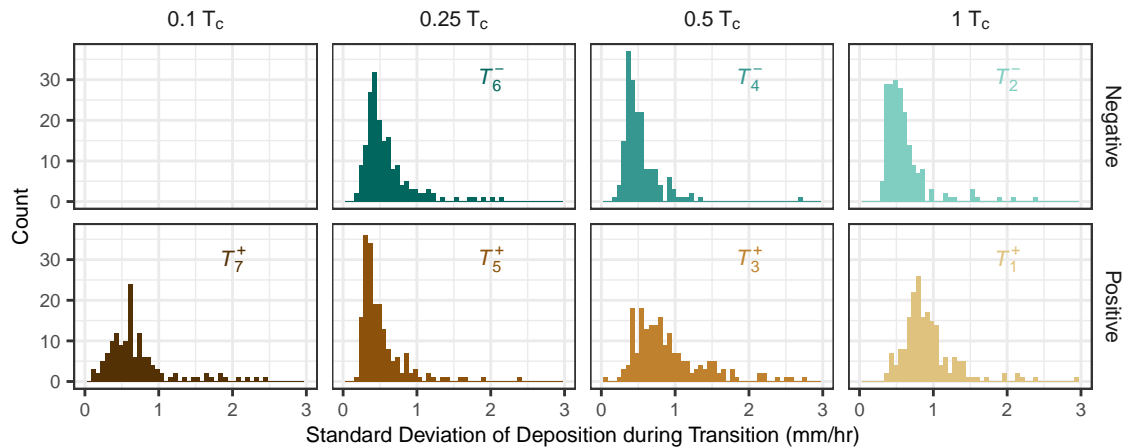


Figure 4.6: Histograms of the standard deviation of sediment accumulation during flooding transitions. In general, there are few differences between positive and negative transitions, except that positive transitions appear to have a slightly higher standard deviation on average.

Over the long term, sedimentation rates approach the long-term mean, but the data show that during negative flooding transitions, the transient sedimentation rate is lower than the long-term aggradation rate. Figure 4.5 demonstrates this, where the long-term aggradation rate is shown relative to the mean aggradation rate of 100

columns sampled for each transition. Results from positive transitions are mixed, where transient sedimentation rates exceed the long-term rate for gradual transitions (0.5 and $1T_c$), but fall short of the long-term rate following abrupt transitions ($0.25T_c$ and $0.1T_c$). Sedimentation variability, as measured by the temporal standard deviation of deposition events, also differs between positive and negative transitions, with positive transitions in general having slightly more variable sedimentation than negative transitions, with the exception of T_5^+ and T_6^- (both of length $0.25T_c$), which were indistinguishable (Figure 4.6). Sedimentation statistics (mean rate and standard deviation) are strong predictors of event preservation bias as shown in Figure 4.7. The mean rate has the largest effect, but the standard deviation is also a significant term (§ A.3.4).

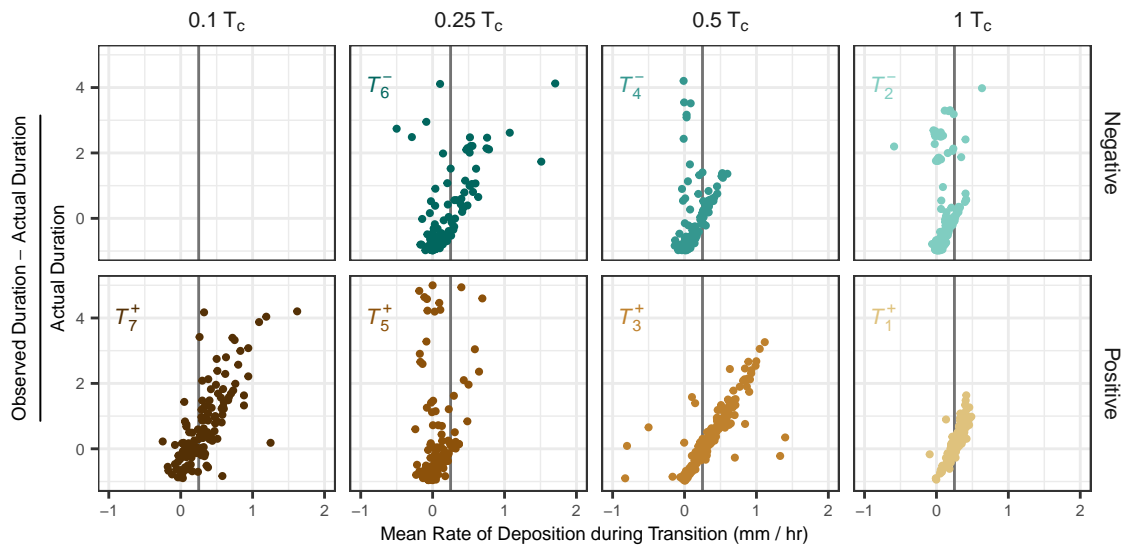


Figure 4.7: Shown is the relationship between the mean accumulation rate during transitions and the stratigraphic bias. Mean accumulation rate is a strong predictor of stratigraphic bias, with values lower than the long-term average accumulation rate mapping to negative bias values.

4.3.3 Surface roughness and sediment dispersal

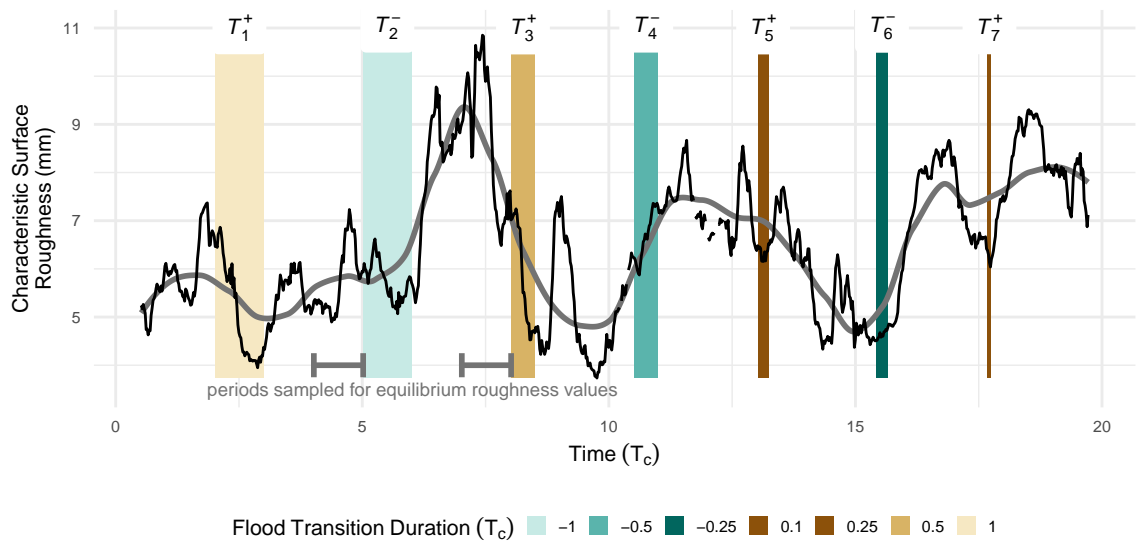


Figure 4.8: Roughness calculated for each run hour, with a LOESS smoothing curve applied in gray. Transitions are marked by colored rectangles. Stasis periods are unmarked intervals. Time axis is given in normalized time units of T_c . Equilibrium values for roughness are extracted from two periods $1T_c$ long that are isolated from transitions and marked by gray bars.

Throughout the experiment, surface roughness generally tracked the value of flooding intensity, with periods of high-intensity flooding generally associated with smooth surface topography and low-intensity flooding characterized by rough surface topography (Figure 4.8). Periods immediately following transitions in flooding were often transiently higher or lower than the equilibrium values, as estimated from two isolated stasis periods of the experiment (see Figure 4.9). Equilibrium values for surface roughness during high-intensity flooding are 5.21–6.21 mm. Estimates of surface roughness immediately following a positive transition—from low-intensity flooding to high-intensity flooding—were as large as 8.82 mm. These roughness values generally differ from the equilibrium value, depending on the duration of the preceding transition. Broadly, surface roughness is large following abrupt positive transitions, and smaller following gradual positive transitions (Figure 4.9), with roughness values after the most gradual transition approaching the equilibrium value. Equilibrium

values estimated for stasis periods of low-intensity flooding are 7.36–10 mm, and immediately following negative transitions (high to low-intensity) estimates of surface roughness were as low as 4.51 mm. After a negative transition, surface roughness is generally lower than the equilibrium value, with more abrupt transitions showing a larger difference compared to equilibrium.

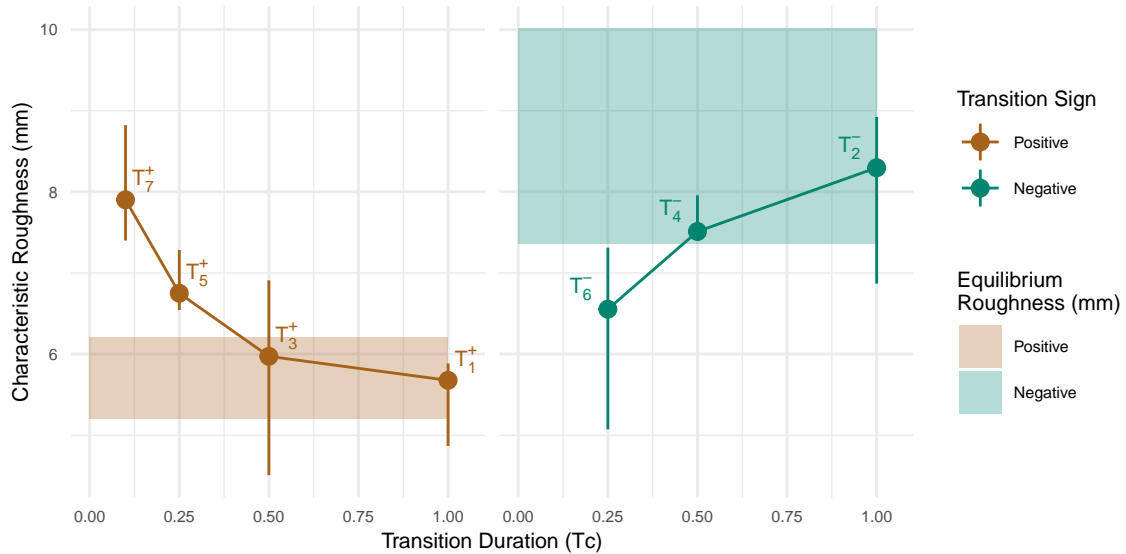


Figure 4.9: Surface roughness estimates after each transition. The duration of the preceding transition is given on the abscissa in units of T_c . Ranges of equilibrium values for roughness during low and high-intensity flooding are given by shaded regions. Abrupt transitions possess roughness values more typical of the preceding flooding regime, whereas gradual transitions are marked by roughness values in the range of equilibrium values.

Visualized using isopach maps, two key observations emerge regarding sediment dispersal patterns after flooding transitions. First, sediment dispersal patterns are qualitatively different between negative and positive transitions (Figure 4.10). Sediment deposited following positive transitions is generally widely distributed, whereas sediment deposited following a negative transition is focused near the river channel. Additionally, following positive transitions, sediment deposition across the topset is generally thicker, whereas following negative transitions, sediment deposition is generally thinner. Second, the differences are more accentuated for abrupt transitions as compared to gradual transitions.

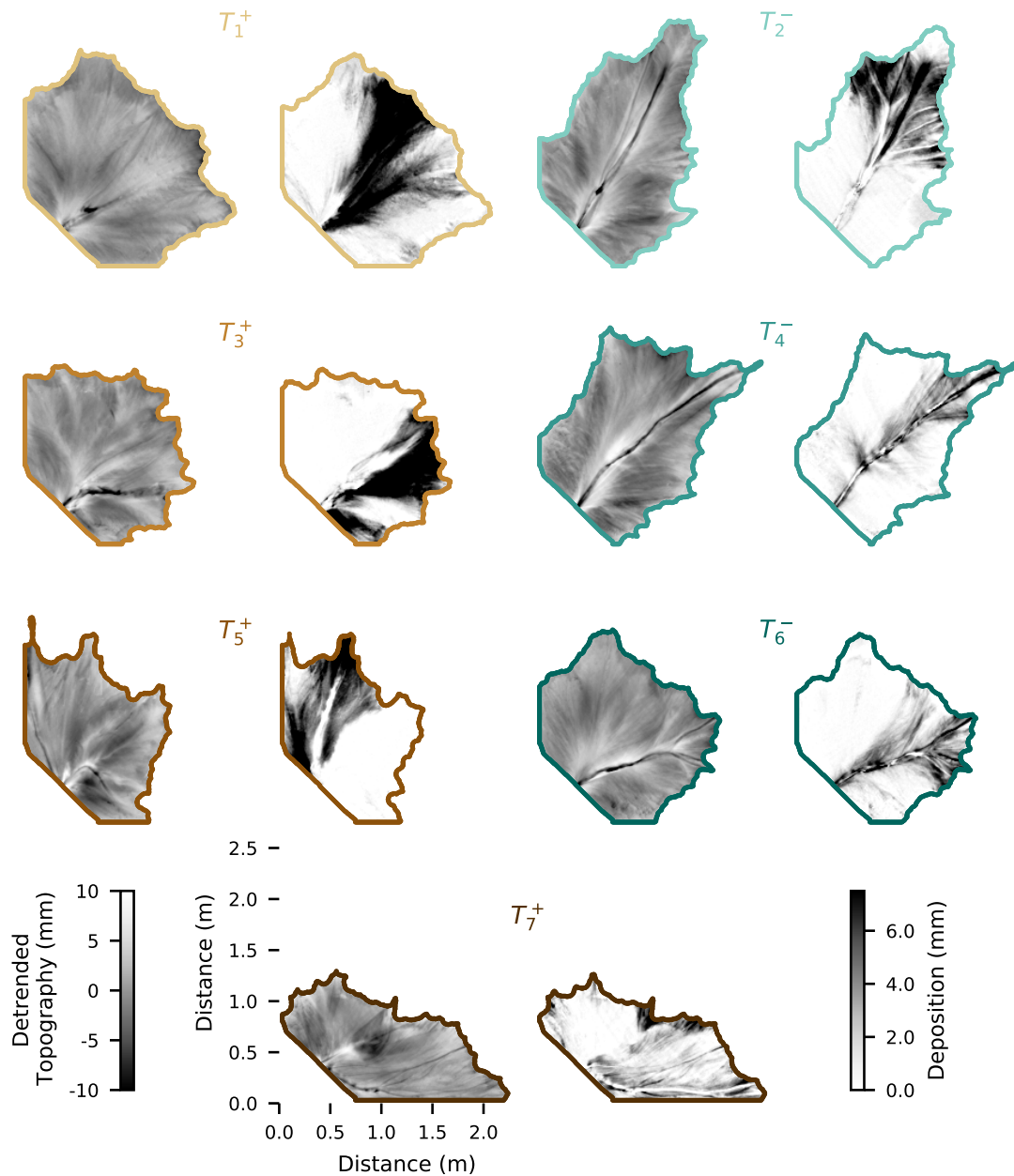


Figure 4.10: Paired maps show detrended topography (Figure 3.6; § 3.2.5) at the end of each transition period, as well as the sediment accumulation for a 10 hour window immediately following the transition. All maps are on the same scale. Isopach maps in general show broad lateral sediment distribution following positive transitions and localized deposition following negative transitions. Large contrasts in detrended topography are indicative of surface roughness, whereas muted colors are indicative of smooth topography. In particular, note prominent alluvial ridges visible in the topography maps for T_3^+ , T_5^+ , and T_7^+ . In the matching isopach maps, sediment accumulation is confined between these ridges. In contrast, note smooth antecedent topography in T_6^- and T_1^+ .

These qualitative observations are quantified in Figure 4.11, where deposition is clearly more extensive for positive transitions as compared to negative transitions. There is also a clear trend, where more abrupt transitions result in more focused deposition regardless of sign. The standard deviation of isopach thickness are also quantified in Figure 4.11, where it is evident that despite the fact that sediment is deposited over a larger area for positive transitions, the thickness within the deposit is more spatially variable than after negative transitions.

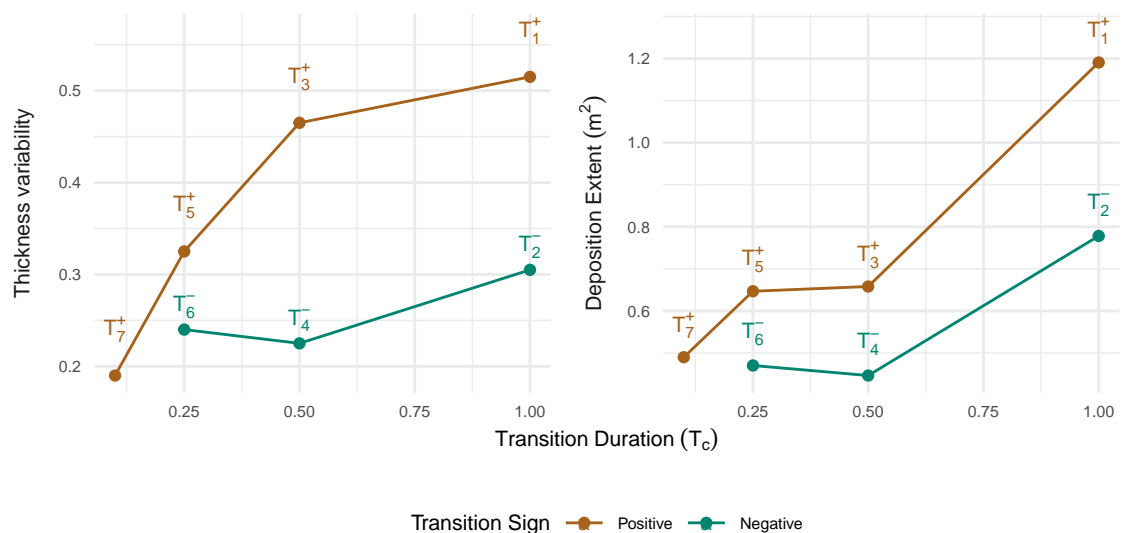


Figure 4.11: The thickness variability of sediment packages was measured as the standard deviation of sediment package thickness for sediment that accumulated in a 10-hour window after each transition. In general, sediment packages are more variable in thickness than negative transitions, and the variability increases as the transitions become more gradual. The extent of deposition following each transition is quantified as the surface area that received at least 2 mm of deposition, and in general, is higher after positive transitions, and has an increasing trend with more gradual transitions.

4.4 Discussion

To accurately forecast the impacts of future climate change, it is critical to understand the taphonomy and stratigraphic expression of past extreme climate events like the PETM (Carmichael et al. 2017). In this study, a fan-delta experiment is used to examine how transitions in flooding intensity impact sediment dispersal and surface

roughness to characterize surface-process disequilibrium following perturbation. The impact of changing sedimentation patterns on the fidelity of signal preservation in the stratigraphic record is then evaluated. The analyses show that changes in hydrograph variability bias the preservation of climate events by affecting sedimentation statistics. Additionally, these observations suggest that sedimentation statistics reflect changing autogenic landscape dynamics, and that the duration and sign of flooding transitions controls the nature of sediment dispersal.

The impact of transitions in flooding intensity on autogenic dynamics, and therefore stratigraphic bias, is best understood by considering how sediment transport processes shape delta floodplain topography. Each flooding intensity regime tested in this experiment (high and low) drives distinctive patterns of sediment dispersal that produce contrasting states of topographic relief (§ 3.2.5). High-intensity flooding produces smooth floodplain topography because vigorous overbank flow distributes sediment which deposits in topographic lows. In contrast, sluggish overbank flow during low-intensity flooding generates local aggradation and uneven sedimentation patterns, thus enhancing floodplain relief.

Abrupt transitions in flood regime create disequilibrium by juxtaposing the current flood regime against topography inherited from the prior flood regime. For example, transition T_5^+ (marked on Figure 4.8) was the second-most abrupt positive transition ($0.25 \times T_c$), and as a result, the inherited topography was out of equilibrium with respect to the flooding regime, as exemplified in Figure 4.9. Reëquilibrating topography with the flood regime can proceed one of two ways: either (1) by *reworking*, where river channels erode the surface and replace it with new sediment, or (2) by *repaving*, where the sediment aggrades on top of the existing surface to generate new topography. In this experimental apparatus, significant erosion of the surface is rare because of the cohesive nature of the sediment, and the high long-term aggradation rate favors repaving as the dominant mechanism of topographic change.

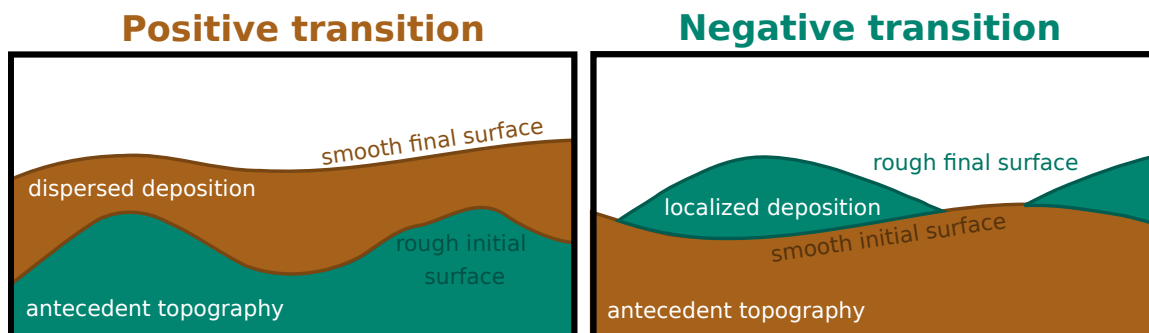


Figure 4.12: Cartoon showing differences in repaving strategies following negative and positive transitions. Following positive transitions, the antecedent topography is rough and intense flood disperse sediment widely, where it fills topographic lows to produce a smooth equilibrium surface. In contrast, to reequilibrate following a negative transition, sluggish overbank flows deposit sediment locally, constructing a rough equilibrium surface.

A cartoon of this process for both the negative and positive transitions is shown in Figure 4.12. Before a negative transition, the delta floodplain is characterized by low-relief topography, and in order to create new surface roughness, localized sediment deposition is required. In contrast, when rough topography is inherited after positive transitions, topographic lows are filled in to smooth out the surface. The recovery pathway required to repave the fluvial surface with new sediment is clearly dependent both the degree of disequilibrium and the nature of topography-process mismatch.

4.4.1 Hysteresis in fluvial response

Across all observations presented in this study, the effects of positive flooding transitions are categorically different than negative transitions. The difference in response demonstrates that following a change in flood regime, the fluvial system reequilibration exhibits hysteresis, because the inherited topography following transitions of a different sign requires a different pathway to reverse. For example, positive transitions in flood regime inherit comparatively rough topography, but the equilibrium topography is smooth. High-intensity flooding promotes intense overbank flow that routes sediment from the channel to the delta floodplain. This process, in conjunc-

tion with an active, highly mobile channel (see § 3.3.1), disperses sediment laterally over the delta topset, filling topographic lows with sediment. Initially, relict topography partially confines sediment dispersal, as alluvial ridges and delta lobes act as barriers to flow, but as topographic lows are repaved, subsequent floods can overtop confining topography. In this way, new areas become available for deposition: a feedback process sustaining uniform sedimentation. This process is shown in Figure 4.10, where isopach maps of transitions T_1^+ , T_3^+ , and T_5^+ show sediment accumulation filling remnant alluvial swales. T_1^+ exhibits the least confinement, because the inherited topography was within the range of equilibrium values (Figure 4.9), whereas T_5^+ is relatively confined compared to more gradual transitions. This trend is supported by the fact that the sediment accumulation rate measured from randomly selected columns generally increases following positive transitions. The additional sediment that is directed overbank and used to repave the the surface is initially uneven, because the basal contact is rough (Figure 4.10 and Figure 4.12)

In contrast, negative transitions inherit smooth topography, but the equilibrium topography is rough. Low-intensity flooding tends to focus deposition close to the channel margins, because sluggish overbank flows transport suspended sediment onto the floodplain, but lack the capacity to route the sediment beyond the region immediately adjacent to the channel. When the delta floodplain is in dynamic equilibrium with low-intensity flooding, uneven sediment dispersal creates a feedback that promotes the growth of levees that further confine flow and limit the spatial distribution of sediment. After an abrupt negative transition in flood intensity, however, smooth topography and a lack of levees means that for a transient period, overbank flow distributes more sediment to the channel margins, which aggrades to build levees. This can be seen in Figure 4.10, where T_2^- , T_4^- , and T_6^- all show varying extents of locally-focused deposition. T_4^- is perhaps the best example, as miniature crevasse splays can be observed along both channel banklines, and levee aggradation is clearly

visible, but the region of deposition is restricted compared to positive transitions. This is quantified in Figure 4.11, where the extent and thickness of post-transition deposition is smaller for negative versus positive transitions.

4.4.2 Climate event duration and fluvial disequilibrium

Since inherited topography controls sediment distribution following flooding transitions, it follows that abrupt transitions create more extreme fluvial disequilibrium than gradual transitions. Shown by the surface roughness immediately following flooding transitions (Figure 4.9), the more abrupt a transition is, the more relict topography remains to be repaved. For example, T_7^+ was the most abrupt positive transition in flooding intensity (duration $0.1 \times T_c$, in Figure 4.9), and juxtaposed high-intensity flooding on a fluvial surface with large topographic relief (8.3 mm). As a result, during the interval immediately following this transition, the sedimentary system was confined between preëxisting alluvial ridges, and most sediment deposition was directed to the delta shoreline. In fact, the inherited topography was rough enough following this transition that the system never fully equilibrated before the end of the experimental run (see roughness values in Figure 4.8 from the last transition to the end). This episode contrasts with a gradual positive transition in flooding intensity (duration $1 \times T_c$), where successively more intense flooding dispersed sediment into alluvial swales and therefore repaving the surface during the transition itself. In this way, after the transition was complete, the topography had already been partially resurfaced, and recovery to equilibrium conditions was established faster than following abrupt transitions.

A similar pattern is borne out for negative transitions, but with some important differences. For example, the extent of deposition following abrupt negative transitions is also spatially restricted compared to gradual negative transitions; this

is the same pattern observed for positive transitions (Figure 4.11), but for a different reason. While deposition after abrupt positive transitions is confined by relict topography, following the most abrupt negative transitions, sediment transport to channel margins is enhanced by a lack of levees. In contrast, following a gradual negative transition, levee aggradation during the transition itself confines flow, and instead focuses deposition basinward and prograding delta lobes (Figure 4.10).

4.4.3 Stratigraphic bias during climate events

The fidelity of paleoclimate records is dependent on the temporal sampling resolution of the stratigraphic record. Bias and uncertainty arise because the statistics of stochastic sedimentation, which results in uneven temporal sampling (Schumer et al. 2011). By understanding how climate events alter sedimentation statistics, this bias can be predicted.

If the mean sedimentation rate is equivalent to the long-term aggradation rate, and the statistics of sedimentation do not change throughout the climate event, that is, they are stationary through time, then no bias is expected for the preservation of climate events. In contrast, the results presented herein show that positive transitions in flooding intensity promote rapid sedimentation during the climate event as compared to true onset time (Figure 4.5). As a consequence, time is more likely to be preserved during the climate transition and represented in the stratigraphic record than would be expected by a linear age model. The outcome of enhanced temporal sampling is that climate events are dilated relative to their true duration. An ensemble of columns from the experiments demonstrates this outcome (Figure 4.3), where for positive transitions, the perceived duration of climate events is consistently longer than the true duration.

In the opposite scenario, during negative transitions sediment is focused at

channel margins and on delta lobes (Figure 4.10; T_2^- , T_4^- , T_6^-). Thus, a given column in an ensemble is more likely to have a hiatus than would be expected if sedimentation statistics were stationary throughout the interval—as is assumed for a linear age model. As a consequence, time is undersampled relative to the null expectation, and the perceived length of the climate transition is compressed.

4.4.4 Implications for interpreting Eocene hyperthermal events

Eocene hyperthermals like the PETM are some of the closest geologic analogues available for contemporary climate warming. The PETM is characterized by an abrupt onset phase and a gradual recovery phase, and is interpreted to have a severe ecological, biogeochemical, and landscape evolution consequences (McInerney and Wing 2011, also § 2.1). In part, a better understanding of these impacts depends on constraining the onset and recovery times with precision. In many terrestrial basins, the PETM is thought to have enhanced seasonal flooding intensity (Foreman et al. 2012; Chen et al. 2018), and while estimates for the duration of the PETM onset vary, in general there is consensus that the onset is approximately 20 ka or less (e.g. Bowen et al. 2001; Aziz et al. 2008). Thus, the onset of the PETM can be interpreted as an abrupt positive flooding transition, especially in the Piceance Basin (§ 2.5).

As our experiments show, an abrupt positive transition in flooding intensity results in persistent landscape disequilibrium, where high-intensity flooding disperses sediment laterally to either repave rough inherited topography or rework it through lateral erosion. Applying these results to the PETM in the Piceance Basin yields two main insights. First, the contact between pre-PETM and PETM sediment is likely to represent a substantial hiatus. This is because sediment deposited at the onset of the PETM and immediately after would have reworked and repaved over relict alluvial topography, which itself was likely in stasis, given that the conditions before the PETM

were likely characterized by low-intensity flooding (§ 2.5). Second, progressively intensified flooding during the PETM onset would have transiently enhanced sediment accumulation rates, so the perceived duration of the PETM onset in the Piceance should therefore be dilated. Put another way, after the PETM, hiatuses are shorter because sediment is widely dispersed by mobile channels. In this way, estimates of the PETM onset time derived from fluvial strata are likely to be overestimates, meaning that the event onset was likely more abrupt than measured.

The PETM is followed by a recovery phase, which is generally estimated to take place over approximately 200 ka (Aziz et al. 2008; Röhl et al. 2007), constituting a gradual negative transition in flooding intensity. As our experiments show, stratigraphy produced by a gradual decrease in flood intensity undersamples time, meaning that estimates of the duration of the PETM recovery are likely underestimates of the true recovery time. Therefore, a complete picture of the PETM in terrestrial basins impacted by changes in flooding intensity is likely to overestimate the onset time and underestimate the recovery time.

4.5 Summary

Due to the poor temporal resolution of the stratigraphic record, constraining important aspects of major climate events in Earth history like the PETM remains a challenge. Events like the PETM can only be detected in the stratigraphic record if the event is longer than characteristic timescales set by autogenic sediment transport processes. To date, this threshold has largely been considered as an intrinsic property of the sedimentary system, uncoupled from climate change itself. However, during major climate events, autogenic dynamics covary with boundary conditions, introducing unaccounted-for bias in paleoclimate reconstructions.

This study imposed abrupt transitions in hydrograph variability on physical sedimentary experiments to explore the fluvio-deltaic response to climate events like the PETM. Fluvio-deltaic systems in equilibrium produce topography with characteristic relief, and the data demonstrate that after abrupt transitions in boundary conditions, the antecedent topography is out of equilibrium with current conditions. In this way, fluvio-deltaic systems retain memory of previous conditions until either aggradation has repaved antecedent topography, or the surface is reworked through erosion.

Equilibrium is reestablished after a negative (high to low) flooding transition via locally focused deposition that constructs alluvial topography. In contrast, following positive (low to high) transitions, topographic equilibrium is restored by filling broad regions of low topography (Figure 4.12). These different sediment dispersal patterns result in signal preservation bias in the stratigraphic record. Since sediment was evenly distributed during positive transitions, paleoclimate records extracted from those stratigraphy preferentially oversample time, which dilates the perceived duration of the climate perturbation. In contrast, focused accumulation following negative transitions increases the spatial heterogeneity of sediment packages; on average, paleoclimate records during these events undersample time, thus compressing the perceived duration of the climate event.

Preserved records of climate change are subject to many sources of uncertainty; to derive insight, all sources must be recognized and constrained. These results indicate that climate reconstructions assuming a linear age model are not only subject to uncertainty due to stratigraphic incompleteness, sediment buffering and signal shredding, but may in fact be systematically biased by interactions between allogenic change and autogenic dynamics. In order for climate events like the PETM to be resolved in the stratigraphy, they have to pass a taphonomic threshold, but because changes in climate can modulate autogenic sedimentary processes, the threshold itself

is a function of the climate change. The direction in which the threshold moves depends on the nature of the climate change event, but nonetheless, introduces a source of predictable, systematic bias to paleoclimate reconstruction.

Chapter 5

Conclusion

River flooding is ubiquitous, and a grave hazard for people who live along river corridors. While the immediate threats from flooding are the loss of life and property damage (Dankers and Feyen 2008; Simonovic 2009), flooding is also a key control on landscape evolution (Bauch and Hickin 2011), and in this way threatens the long-term sustainability of riparian communities (Haque and Zaman 1989). Furthermore, with contemporary global climate change, flood hazard is expected to intensify in the coming decades and centuries (Trenberth 2011), but there is no road map for how these threats will manifest (Jakob and Church 2011).

Insight into future change can be derived from the stratigraphic record, which archives the environmental impacts of climate change in the geologic past. However, when it comes to interpreting the impacts of intensified flooding from strata, interpretations of paleoclimate are clouded by a fundamental lack of knowledge of the ways that variable flow impacts fluvial morphodynamics. This dissertation characterizes the processes at play when an alluvial system undergoes a transition from one flooding regime to another, using this simplified scenario as a model for past, present, and future climate change.

A geologic case study of this scenario is explored in Chapter 2. Using the example of the PETM, archived by strata in the Piceance Basin, the impact that flooding has on stratigraphic stacking patterns in alluvial landscapes is addressed. The prevailing model for landscape response during the PETM asserts that a shift from muted, low-intensity flooding to high-intensity flooding in many regions instigated wide-spread sediment mobilization (e.g. Foreman et al. 2012; Pujalte et al. 2015; Lyons et al. 2019). In this chapter, I falsified this model by demonstrating that

in the Piceance Basin, no evidence exists for a basin-wide increase in sediment supply. An alternative model of fluvial landscape response is proposed whereby sediment was sorted by mobile channels that reworked floodplain deposits, such that sand was preferentially retained in terrestrial basins, while mud was preferentially exported to downstream basins.

To evaluate this framework, a suite of experiments were conducted to explore fluvial responses to changes in flood conditions. One aspect of fluvial system evolution in response to flooding that remained untested is the assumption that since increased amounts of flooding tend to accelerate fluvial dynamics, the response must be monotonic with flooding intensity. In Chapter 3, I tested this assumption by evaluating fluvial morphodynamics across a gradient of flooding conditions, and discovered that levees stabilize channels, and generate a non-monotonic response. As a result, levee construction is identified as a key mechanism missing from descriptions of fluvial landscape evolution under variable flow. At basin-filling scales, these results suggest that flooding intensity can impact stratigraphic architecture in counterintuitive ways; for example, a decrease in flooding intensity could actually result in higher channel mobility. These experiments verify that in the Piceance Basin, enhanced accumulation of sand in terrestrial basins can be generated by changes in flooding intensity alone that enhance channel mobility.

To evaluate the impact of these processes and feedbacks on the stratigraphic expression of climate change, in Chapter 4 I engineered hydroclimate perturbations in experimental deltas. In this experiment, the difference between positive (low-to-high), as well as negative (high-to-low) transitions is evaluated, while the duration of each climate perturbation was controlled. Three main observations were made. First, the perceived duration of each climate transition was biased from the true duration, and reconstructions based on strata deposited during positive transitions consistently overestimated the length of the transition, whereas reconstructions from negative

transitions consistently underestimated the event duration. Second, during positive transitions, sediment accumulation rates transiently exceed the long-term average, whereas during negative transitions, sediment accumulation rates are transiently depressed. Finally, surface roughness was measured throughout the experiment, and it is evident that surface roughness immediately following each transition scales with the duration and sign of transition.

Via this third insight, I discovered that landscape and stratigraphic response to climate change is best understood through the lens of landscape–process disequilibrium. Chapter 3, shows that each flooding regime is characterized by an equilibrium surface roughness. In Chapter 4, it is demonstrated that immediately following a transition from one flood regime to another, the topography is out of equilibrium with the flood regime, and that following a transition, equilibrium topography is restored by a combination of surface reworking and repaving. During negative transitions, sediment deposition is laterally restricted as a result of feedbacks that promote surface roughening, so average deposition rates across the delta topset are transiently depressed. In contrast, during positive transitions, process feedbacks promote widespread sediment distribution, which is deposited on rugose topography, transiently raising the short-term deposition rate.

These new tools and insights can be applied to understanding paleoclimate during the PETM. Evidence presented in Chapter 4 clearly shows that stratigraphic bias accompanies changes in surface processes during climate events. The duration of the PETM is estimated from sections using a variety of tools, but a fundamental underlying assumption of most paleoclimate reconstructions is that sedimentation rates are near-linear between known age control points, and that time is evenly sampled. While it is well-known that time is not evenly sampled in the stratigraphic record, I showed in this chapter that these assumptions can lead to fundamentally biased reconstructions of climate event timing. Using the example of the PETM, these re-

sults imply that in localities where the PETM is associated with intensified channel dynamics, estimates of the onset of the PETM are likely to be overestimates. Thus, the climate event may have been even more abrupt than previously thought. Furthermore, these results imply that estimates for the recovery time for the PETM are likely to be underestimates. That is, abnormal climate conditions may have persisted much longer than previously estimated, making for a sluggish recovery.

There were substantial regional differences in the precipitation response to the PETM, with models predicting that some regions became more arid and flashy, while others became more humid, with consistent runoff. For example, the results in Chapter 2 indicate that intensified flooding destabilized channels in some regions like the Piceance Basin. The outcomes from Chapter 3 imply that the surface-process response to these regional changes may be more complex than previously thought. However, in other regions, intensified flooding may have actually stabilized channels during the PETM. This idea remains untested from stratigraphic data, and constitutes a new avenue of potential research.

By advancing knowledge of how variable flow impacts fluvial morphodynamics, this dissertation lays the groundwork for refining landscape evolution models to incorporate complex responses to flow variability, and improve interpretations of climate events in the geologic past. Additionally, this dissertation adds to the mounting evidence that environmental variability fundamentally alters sediment transport processes, rather than simply obscuring the overall trend. That is, in addition to being a source of noise in sedimentary systems, floods are also themselves a signal that is propagated into the stratigraphic record. Leveraging this signal content of the river hydrograph will yield new insights into fluvial landscape evolution, and sharper tools for interpreting of the stratigraphic record.

Bibliography

- Abels, Hemmo A. et al. (Jan. 15, 2010). “Long-period eccentricity control on sedimentary sequences in the continental Madrid Basin (middle Miocene, Spain)”. In: *Earth and Planetary Science Letters* 289.1, pp. 220–231. DOI: 10.1016/j.epsl.2009.11.011 (cited on page 60).
- Allen, J. R. L. (1978). “Studies in fluvial sedimentation: an exploratory quantitative model for the architecture of avulsion-controlled alluvial suites”. In: *Sedimentary Geology* 21.2, pp. 129–147 (cited on page 2).
- Aziz, Hayfaa Abdul et al. (July 1, 2008). “Astronomical climate control on paleosol stacking patterns in the upper Paleocene–lower Eocene Willwood Formation, Bighorn Basin, Wyoming”. In: *Geology* 36.7, pp. 531–534. DOI: 10.1130/G24734A.1 (cited on pages 82, 83).
- Baczynski, Allison A. et al. (Sept. 1, 2016). “Distortion of carbon isotope excursion in bulk soil organic matter during the Paleocene-Eocene thermal maximum”. In: *GSA Bulletin* 128.9, pp. 1352–1366. DOI: 10.1130/B31389.1 (cited on page 59).
- Bauch, Gregory D. and Edward J. Hickin (2011). “Rate of floodplain reworking in response to increasing storm-induced floods, Squamish River, south-western British Columbia, Canada”. In: *Earth Surface Processes and Landforms* 36.7, pp. 872–884. DOI: <https://doi.org/10.1002/esp.2115> (cited on page 86).
- Bijl, Peter K. et al. (Oct. 8, 2009). “Early Palaeogene temperature evolution of the southwest Pacific Ocean”. In: *Nature* 461.7265, pp. 776–779. DOI: 10.1038/nature08399 (cited on page 12).
- Birgenheier, L. P. et al. (2020). “Climate impact on fluvial-lake system evolution, Eocene Green River Formation, Uinta Basin, Utah, USA”. In: *Bulletin* 132.3, pp. 562–587 (cited on page 15).
- Blom, Astrid et al. (2017). “The equilibrium alluvial river under variable flow and its channel-forming discharge”. In: *Journal of Geophysical Research: Earth Surface* 122.10, pp. 1924–1948. DOI: 10.1002/2017JF004213 (cited on pages 3, 4, 7, 26, 27).
- Bowen, Gabriel J. et al. (2001). “Refined isotope stratigraphy across the continental Paleocene-Eocene boundary on Polecat Bench in the northern Bighorn Basin”. In: *Paleocene-Eocene Stratigraphy and Biotic Change in the Bighorn and Clarks Fork Basins, Wyoming. University of Michigan Papers on Paleontology* 33, pp. 73–88 (cited on page 82).

- Bryant, Madeline, Peter Falk, and Chris Paola (Apr. 1, 1995). “Experimental study of avulsion frequency and rate of deposition”. In: *Geology* 23.4, pp. 365–368. DOI: 10.1130/0091-7613(1995)023<0365:ES0AFA>2.3.CO;2 (cited on pages 21, 28, 61).
- Carmichael, Matthew J. et al. (Oct. 1, 2017). “Hydrological and associated biogeochemical consequences of rapid global warming during the Paleocene-Eocene Thermal Maximum”. In: *Global and Planetary Change* 157, pp. 114–138. DOI: 10.1016/j.gloplacha.2017.07.014 (cited on pages 12, 15, 76).
- Chamberlin, Ellen P. and Elizabeth A. Hajek (June 1, 2019). “Using bar preservation to constrain reworking in channel-dominated fluvial stratigraphy”. In: *Geology* 47.6, pp. 531–534. DOI: 10.1130/G46046.1 (cited on page 17).
- Chen, Chen et al. (Sept. 6, 2018). “Estimating regional flood discharge during Palaeocene-Eocene global warming”. In: *Scientific Reports* 8.1, p. 13391. DOI: 10.1038/s41598-018-31076-3 (cited on pages 6, 12, 61, 82).
- D’Ambrosia, Abigail R. et al. (Mar. 1, 2017). “Repetitive mammalian dwarfing during ancient greenhouse warming events”. In: *Science Advances* 3.3, e1601430. DOI: 10.1126/sciadv.1601430 (cited on page 12).
- Dai, Aiguo (Sept. 15, 2006). “Precipitation Characteristics in Eighteen Coupled Climate Models”. In: *Journal of Climate* 19.18, pp. 4605–4630. DOI: 10.1175/JCLI3884.1 (cited on page 1).
- Dankers, Rutger and Luc Feyen (2008). “Climate change impact on flood hazard in Europe: An assessment based on high-resolution climate simulations”. In: *Journal of Geophysical Research: Atmospheres* 113 (D19). DOI: 10.1029/2007JD009719 (cited on pages 11, 86).
- Davis, John Clements (2011). *STATISTICS AND DATA ANALYSIS IN GEOLOGY, 3RD ED.* John Wiley & Sons. 656 pp. (cited on page 103).
- DeConto, Robert M. et al. (Apr. 2012). “Past extreme warming events linked to massive carbon release from thawing permafrost”. In: *Nature* 484.7392, pp. 87–91. DOI: 10.1038/nature10929 (cited on page 11).
- Dickens, Gerald R. et al. (Dec. 1, 1995). “Dissociation of oceanic methane hydrate as a cause of the carbon isotope excursion at the end of the Paleocene”. In: *Paleoceanography* 10.6, pp. 965–971. DOI: 10.1029/95PA02087 (cited on page 11).
- Donnell, John R. (1969). *Paleocene and lower Eocene units in the southern part of the Piceance Creek Basin, Colorado.* US Govt. Print. Off., (cited on page 14).
- Engelund, F. and E. Hansen (1967). “A monograph on sediment transport in alluvial streams”. In: *Technical University of Denmark Østervoldgade 10, Copenhagen K.* (cited on page 26).

- Erhardt, Andrea M (2005). “Relative contributions of tectonics and climate on fluvial sedimentation in the Wasatch Formation of western Colorado”. PhD thesis. Colorado School of Mines. Arthur Lakes Library (cited on page 15).
- Esposito, Christopher R. et al. (June 26, 2018). “Sediment Storage Partitioning in Alluvial Stratigraphy: The Influence of Discharge Variability”. In: *Journal of Sedimentary Research* 88.6, pp. 717–726. DOI: 10.2110/jsr.2018.36 (cited on pages 3, 13, 22, 26, 28, 51, 61).
- Ethridge, Frank G. and Stanley A. Schumm (1977). “Reconstructing paleochannel morphologic and flow characteristics: methodology, limitations, and assessment”. In: (cited on pages 4, 16).
- Farquhar, G D, J R Ehleringer, and {and} K. T. Hubick (1989). “Carbon Isotope Discrimination and Photosynthesis”. In: *Annual Review of Plant Physiology and Plant Molecular Biology* 40.1, pp. 503–537. DOI: 10.1146/annurev.pp.40.060189.002443 (cited on page 59).
- Fielding, Christopher R., Jan Alexander, and Jonathan P. Allen (Mar. 1, 2018). “The role of discharge variability in the formation and preservation of alluvial sediment bodies”. In: *Sedimentary Geology* 365, pp. 1–20. DOI: 10.1016/j.sedgeo.2017.12.022 (cited on pages 15, 22, 28).
- Foreman, Brady Z. (Apr. 2014). “Climate-driven generation of a fluvial sheet sand body at the Paleocene-Eocene boundary in north-west Wyoming (USA)”. In: *Basin Research* 26.2, pp. 225–241. DOI: 10.1111/bre.12027 (cited on pages 5, 6).
- Foreman, Brady Z., Paul L. Heller, and Mark T. Clementz (Oct. 24, 2012). “Fluvial response to abrupt global warming at the Palaeocene/Eocene boundary”. In: *Nature* 491.7422, pp. 92–95. DOI: 10.1038/nature11513 (cited on pages 4, 6, 12, 14, 15, 61, 82, 86, 102).
- Foreman, Brady Z. and Kyle M. Straub (Sept. 1, 2017). “Autogenic geomorphic processes determine the resolution and fidelity of terrestrial paleoclimate records”. In: *Science Advances* 3.9, e1700683. DOI: 10.1126/sciadv.1700683 (cited on pages 8, 60, 65).
- Ganti, Vamsi et al. (June 1, 2011). “Space-time dynamics of depositional systems: Experimental evidence and theoretical modeling of heavy-tailed statistics”. In: *Journal of Geophysical Research: Earth Surface* 116 (F2). DOI: 10.1029/2010JF001893 (cited on page 60).
- Ganti, Vamsi et al. (May 1, 2016). “Experimental river delta size set by multiple floods and backwater hydrodynamics”. In: *Science Advances* 2.5, e1501768. DOI: 10.1126/sciadv.1501768 (cited on page 3).

- Ganti, Vamsi et al. (July 28, 2020). “Morphodynamic Hierarchy and the Fabric of the Sedimentary Record”. In: *Geophysical Research Letters* 47.14. DOI: 10.1029/2020GL087921 (cited on page 2).
- Gergel, Diana R. et al. (Mar. 1, 2017). “Effects of climate change on snowpack and fire potential in the western USA”. In: *Climatic Change* 141.2, pp. 287–299. DOI: 10.1007/s10584-017-1899-y (cited on page 2).
- Gilvear, D. J. and S. J. Winterbottom (1992). “Channel change and flood events since 1783 on the regulated river tay, Scotland: Implications for flood hazard management”. In: *Regulated Rivers: Research & Management* 7.3, pp. 247–260. DOI: <https://doi.org/10.1002/rrr.3450070304> (cited on pages 1, 4).
- Gocke, M., K. Pustovoytov, and Y. Kuzyakov (Mar. 15, 2010). “Effect of CO₂ concentration on the initial recrystallization rate of pedogenic carbonate — Revealed by ¹⁴C and ¹³C labeling”. In: *Geoderma* 155.3, pp. 351–358. DOI: 10.1016/j.geoderma.2009.12.018 (cited on page 59).
- Hajek, E. A. and D. A. Edmonds (Mar. 1, 2014). “Is river avulsion style controlled by floodplain morphodynamics?” In: *Geology* 42.3, pp. 199–202. DOI: 10.1130/G35045.1 (cited on pages 17, 19).
- Hajek, Elizabeth A. and Kyle M. Straub (2017). “Autogenic Sedimentation in Clastic Stratigraphy”. In: *Annual Review of Earth and Planetary Sciences* 45.1, pp. 681–709. DOI: 10.1146/annurev-earth-063016-015935 (cited on page 5).
- Haque, C. E. and M. Q. Zaman (1989). “Coping with Riverbank Erosion Hazard and Displacement in Bangladesh: Survival Strategies and Adjustments”. In: *Disasters* 13.4, pp. 300–314. DOI: <https://doi.org/10.1111/j.1467-7717.1989.tb00724.x> (cited on pages 2, 86).
- Held, Isaac M. and Brian J. Soden (Nov. 1, 2006). “Robust Responses of the Hydrological Cycle to Global Warming”. In: *Journal of Climate* 19.21, pp. 5686–5699. DOI: 10.1175/JCLI3990.1 (cited on page 1).
- Heller, Paul L. and Chris Paola (1992). “The large-scale dynamics of grain-size variation in alluvial basins, 2: Application to syntectonic conglomerate”. In: *Basin Research* 4.2, pp. 91–102 (cited on page 55).
- Hickin, Edward J. and Gerald C. Nanson (Nov. 1984). “Lateral Migration Rates of River Bends”. In: *Journal of Hydraulic Engineering* 110.11, pp. 1557–1567. DOI: 10.1061/(ASCE)0733-9429(1984)110:11(1557) (cited on page 2).
- Howard, Alan D. (1982). “Equilibrium and time scales in geomorphology: Application to sand-bed alluvial streams”. In: *Earth Surface Processes and Landforms* 7.4, pp. 303–325. DOI: 10.1002/esp.3290070403 (cited on pages 3, 4).

- Hoyal, D. C. J. D. and B. A. Sheets (2009). “Morphodynamic evolution of experimental cohesive deltas”. In: *Journal of Geophysical Research: Earth Surface* 114 (F2). DOI: 10.1029/2007JF000882 (cited on page 30).
- Jakob, Matthias and Mike Church (Jan. 1, 2011). “The Trouble with Floods”. In: *Canadian Water Resources Journal / Revue canadienne des ressources hydriques* 36.4, pp. 287–292. DOI: 10.4296/cwrj3604928 (cited on page 86).
- Jerolmack, Douglas J. and Chris Paola (Oct. 1, 2010). “Shredding of environmental signals by sediment transport”. In: *Geophysical Research Letters* 37.19, p. L19401. DOI: 10.1029/2010GL044638 (cited on pages 12, 61).
- Jerolmack, Douglas J. and Peter Sadler (Feb. 7, 2018). “Transience and persistence in the depositional record of continental margins”. In: *Journal of Geophysical Research: Earth Surface*. DOI: 10.1029/2006JF000555@10.1002/(ISSN)2169-9011.LANDSCAPE1 (cited on pages 36, 105).
- John, Cédric M. et al. (June 1, 2008). “North American continental margin records of the Paleocene-Eocene thermal maximum: Implications for global carbon and hydrological cycling”. In: *Paleoceanography* 23.2. DOI: 10.1029/2007PA001465 (cited on pages 6, 12).
- Johnson, Ronald C. and Romeo M. Flores (2003). “History of the Piceance Basin from latest Cretaceous through early Eocene and the characterization of lower Tertiary sandstone reservoirs”. In: (cited on pages 14, 22).
- Jones, H. L. and E. A. Hajek (Nov. 15, 2007). “Characterizing avulsion stratigraphy in ancient alluvial deposits”. In: *Sedimentary Geology* 202.1, pp. 124–137. DOI: 10.1016/j.sedgeo.2007.02.003 (cited on page 17).
- Junk, Wolfgang J., Peter B. Bayley, and Richard E. Sparks (1989). “The flood pulse concept in river-floodplain systems”. In: *Canadian special publication of fisheries and aquatic sciences* 106.1, pp. 110–127 (cited on page 1).
- Kelly, D. Clay, Timothy J Bralower, and James C Zachos (Aug. 1, 1998). “Evolutionary consequences of the latest Paleocene thermal maximum for tropical planktonic foraminifera”. In: *Palaeogeography, Palaeoclimatology, Palaeoecology* 141.1, pp. 139–161. DOI: 10.1016/S0031-0182(98)00017-0 (cited on page 12).
- Kennett, J. P. and L. D. Stott (Sept. 1991). “Abrupt deep-sea warming, palaeoceanographic changes and benthic extinctions at the end of the Palaeocene”. In: *Nature* 353.6341, pp. 225–229. DOI: 10.1038/353225a0 (cited on pages 5, 11, 59).
- Kim, Wonsuck et al. (Dec. 1, 2006). “Shoreline response to autogenic processes of sediment storage and release in the fluvial system”. In: *Journal of Geophysical*

- Research: Earth Surface* 111 (F4). DOI: 10.1029/2006JF000470 (cited on pages 30, 31).
- Kirby, W. H. and M. E. Moss (Dec. 15, 1987). “Summary of flood-frequency analysis in the United States”. In: *Journal of Hydrology. Analysis of Extraordinary Flood Events* 96.1, pp. 5–14. DOI: 10.1016/0022-1694(87)90139-9 (cited on pages 1, 4).
- Kirtland Turner, Sandra (Oct. 13, 2018). “Constraints on the onset duration of the Paleocene–Eocene Thermal Maximum”. In: *Philosophical Transactions of the Royal Society A: Mathematical, Physical and Engineering Sciences* 376.2130, p. 20170082. DOI: 10.1098/rsta.2017.0082 (cited on pages 5, 11).
- Konsoer, Kory M et al. (May 6, 2017). “Length scales and statistical characteristics of outer bank roughness for large elongate meander bends: the influence of bank material properties, floodplain vegetation and flow inundation.: Scales of bank roughness on large meander bends”. In: *Earth Surface Processes and Landforms*. DOI: 10.1002/esp.4169 (cited on page 22).
- Kraus, Mary J. and Susan Riggins (2007). “Transient drying during the Paleocene–Eocene Thermal Maximum (PETM): analysis of paleosols in the Bighorn Basin, Wyoming”. In: *Palaeogeography, Palaeoclimatology, Palaeoecology* 245.3, pp. 444–461 (cited on page 15).
- Kraus, Mary J. et al. (Oct. 1, 2015). “Alluvial response to the Paleocene–Eocene Thermal Maximum climatic event, Polecat Bench, Wyoming (U.S.A.)” In: *Palaeogeography, Palaeoclimatology, Palaeoecology* 435 (Supplement C), pp. 177–192. DOI: 10.1016/j.palaeo.2015.06.021 (cited on page 4).
- Kruskal, William H. and W. Allen Wallis (Dec. 1, 1952). “Use of Ranks in One-Criterion Variance Analysis”. In: *Journal of the American Statistical Association* 47.260, pp. 583–621. DOI: 10.1080/01621459.1952.10483441 (cited on page 102).
- Langbein, W. B. (1949). “Annual floods and the partial-duration flood series”. In: *Eos, Transactions American Geophysical Union* 30.6, pp. 879–881. DOI: <https://doi.org/10.1029/TR030i006p00879> (cited on page 1).
- Latrubesse, E. M., J. C. Stevaux, and R. Sinha (Sept. 1, 2005). “Tropical rivers”. In: *Geomorphology. Tropical Rivers* 70.3, pp. 187–206. DOI: 10.1016/j.geomorph.2005.02.005 (cited on page 26).
- Lauer, J. Wesley and Gary Parker (2008). “Modeling framework for sediment deposition, storage, and evacuation in the floodplain of a meandering river: Theory”. In: *Water Resources Research* 44.4. DOI: 10.1029/2006WR005528 (cited on page 27).

- Leary, Kate C. P. and Vamsi Ganti (2020). “Preserved Fluvial Cross Strata Record Bedform Disequilibrium Dynamics”. In: *Geophysical Research Letters* 47.2, e2019GL085910. DOI: 10.1029/2019GL085910 (cited on pages 3, 13).
- Leier, Andrew L., Peter G. DeCelles, and Jon D. Pelletier (2005). “Mountains, monsoons, and megafans”. In: *Geology* 33.4, pp. 289–292 (cited on page 28).
- Leopold, L.B. and Thomas Maddock Jr. (1953). *The hydraulic geometry of stream channels and some physiographic implications*. USGS Numbered Series 252 (cited on page 25).
- Li, Qi, Lizhu Yu, and Kyle M. Straub (Mar. 1, 2016). “Storage thresholds for relative sea-level signals in the stratigraphic record”. In: *Geology* 44.3, pp. 179–182. DOI: 10.1130/G37484.1 (cited on pages 30, 32, 60, 64).
- Lynds, R. M. et al. (Oct. 8, 2014). “Paleoslope Reconstruction In Sandy Suspended-Load-Dominant Rivers”. In: *Journal of Sedimentary Research* 84.10, pp. 825–836. DOI: 10.2110/jsr.2014.60 (cited on page 4).
- Lyons, Shelby L. et al. (Jan. 2019). “Palaeocene–Eocene Thermal Maximum prolonged by fossil carbon oxidation”. In: *Nature Geoscience* 12.1, p. 54. DOI: 10.1038/s41561-018-0277-3 (cited on pages 6, 12, 86).
- McInerney, Francesca A. and Scott L. Wing (2011). “The Paleocene-Eocene Thermal Maximum: A Perturbation of Carbon Cycle, Climate, and Biosphere with Implications for the Future”. In: *Annual Review of Earth and Planetary Sciences* 39.1, pp. 489–516. DOI: 10.1146/annurev-earth-040610-133431 (cited on pages 5, 11, 59, 82).
- Mertes, Leal A. K. (July 1, 1997). “Documentation and significance of the perirheic zone on inundated floodplains”. In: *Water Resources Research* 33.7, pp. 1749–1762. DOI: 10.1029/97WR00658 (cited on page 1).
- Miller, Kimberly Litwin, Wonsuck Kim, and Brandon McElroy (2019). “Laboratory Investigation on Effects of Flood Intermittency on Fan Delta Dynamics”. In: *Journal of Geophysical Research: Earth Surface* 124.2, pp. 383–399. DOI: <https://doi.org/10.1029/2017JF004576> (cited on pages 28, 31).
- Mohrig, David et al. (2000). “Interpreting avulsion process from ancient alluvial sequences: Guadalupe-Matarranya system (northern Spain) and Wasatch Formation (western Colorado)”. In: *Geological Society of America Bulletin* 112.12, pp. 1787–1803 (cited on pages 16, 28).
- Muto, Tetsuji (Mar. 1, 2001). “Shoreline Autoretreat Substantiated in Flume Experiments”. In: *Journal of Sedimentary Research* 71.2, pp. 246–254. DOI: 10.1306/091400710246 (cited on page 61).

- Naito, Kensuke and Gary Parker (2019). “Can Bankfull Discharge and Bankfull Channel Characteristics of an Alluvial Meandering River be Cospecified From a Flow Duration Curve?” In: *Journal of Geophysical Research: Earth Surface* 124.10, pp. 2381–2401. DOI: 10.1029/2018JF004971 (cited on pages 4, 7, 26–28).
- O’Connor, Jim E. and John E. Costa (2004). “Spatial distribution of the largest rainfall-runoff floods from basins between 2.6 and 26,000 km² in the United States and Puerto Rico”. In: *Water Resources Research* 40.1. DOI: <https://doi.org/10.1029/2003WR002247> (cited on page 2).
- Paola, Chris (2000). “Quantitative models of sedimentary basin filling”. In: *Sedimentology* 47 (s1), pp. 121–178 (cited on page 15).
- Paola, Chris, Paul L. Heller, and Charles L. Angevine (1992). “The large-scale dynamics of grain-size variation in alluvial basins, 1: Theory”. In: *Basin Research* 4.2, pp. 73–90 (cited on pages 3, 6).
- Paola, Chris et al. (Dec. 1, 2009). “The “unreasonable effectiveness” of stratigraphic and geomorphic experiments”. In: *Earth-Science Reviews* 97.1, pp. 1–43. DOI: 10.1016/j.earscirev.2009.05.003 (cited on page 4).
- Paola, Chris et al. (2018). “Time Not Our Time: Physical Controls on the Preservation and Measurement of Geologic Time”. In: *Annual Review of Earth and Planetary Sciences* 46.1, pp. 409–438. DOI: 10.1146/annurev-earth-082517-010129 (cited on page 2).
- Parker, Gary (Nov. 14, 1978). “Self-formed straight rivers with equilibrium banks and mobile bed. Part 2. The gravel river”. In: *Journal of Fluid Mechanics* 89.1, pp. 127–146. DOI: 10.1017/S0022112078002505 (cited on page 2).
- Parker, Gary et al. (Oct. 1, 1998). “Alluvial Fans Formed by Channelized Fluvial and Sheet Flow. I: Theory”. In: *Journal of Hydraulic Engineering* 124.10, pp. 985–995. DOI: 10.1061/(ASCE)0733-9429(1998)124:10(985) (cited on page 26).
- Pickup, G. and W. A. Rieger (1979). “A conceptual model of the relationship between channel characteristics and discharge”. In: *Earth Surface Processes* 4.1, pp. 37–42. DOI: 10.1002/esp.3290040104 (cited on pages 2, 3, 25).
- Pielke, Roger A. and Mary W. Downton (Oct. 15, 2000). “Precipitation and Damaging Floods: Trends in the United States, 1932–97”. In: *Journal of Climate* 13.20, pp. 3625–3637. DOI: 10.1175/1520-0442(2000)013<3625:PADFTI>2.0.CO;2 (cited on page 1).
- Pizzuto, James E. (1986). “Flow variability and the bankfull depth of sand-bed streams of the American midwest”. In: *Earth Surface Processes and Landforms* 11.4, pp. 441–450. DOI: 10.1002/esp.3290110409 (cited on page 27).

- Plink-Björklund, Piret (June 2015). “Morphodynamics of rivers strongly affected by monsoon precipitation: Review of depositional style and forcing factors”. In: *Sedimentary Geology* 323, pp. 110–147. DOI: 10.1016/j.sedgeo.2015.04.004 (cited on pages 15, 55).
- Prins, A. (1969). “Dominant discharge”. In: (cited on page 3).
- Prins, A. and M. de Vries (1971). “On dominant discharge concepts for rivers”. In: (cited on page 3).
- Pujalte, V., J. I. Baceta, and B. Schmitz (Dec. 11, 2015). “A massive input of coarse-grained siliciclastics in the Pyrenean Basin during the PETM: the missing ingredient in a coeval abrupt change in hydrological regime”. In: *Climate of the Past* 11.12, pp. 1653–1672. DOI: 10.5194/cp-11-1653-2015 (cited on pages 6, 12, 86).
- Quinn, Niall et al. (2019). “The Spatial Dependence of Flood Hazard and Risk in the United States”. In: *Water Resources Research* 55.3, pp. 1890–1911. DOI: <https://doi.org/10.1029/2018WR024205> (cited on page 2).
- Ravizza, G. et al. (Apr. 1, 2001). “An osmium isotope excursion associated with the Late Paleocene thermal maximum: Evidence of intensified chemical weathering”. In: *Paleoceanography* 16.2, pp. 155–163. DOI: 10.1029/2000PA000541 (cited on page 12).
- Röhl, Ursula et al. (2007). “On the duration of the Paleocene-Eocene thermal maximum (PETM)”. In: *Geochemistry, Geophysics, Geosystems* 8.12. DOI: 10.1029/2007GC001784 (cited on page 83).
- Rouse, Hunter (1939). “Experiments on the mechanics of sediment suspension”. In: *Proc. 5th Int. Congr. Appl. Mech., Cambridge, 1939* (cited on page 22).
- Sadler, Peter M. (Sept. 1, 1981). “Sediment Accumulation Rates and the Completeness of Stratigraphic Sections”. In: *The Journal of Geology* 89.5, pp. 569–584. DOI: 10.1086/628623 (cited on pages 4, 5, 36, 60, 105).
- Schumer, Rina, Douglas Jerolmack, and Brandon McElroy (2011). “The stratigraphic filter and bias in measurement of geologic rates”. In: *Geophysical Research Letters* 38.11. DOI: <https://doi.org/10.1029/2011GL047118> (cited on pages 65, 81).
- Simonovic, S. P. (2009). “Managing flood risk, reliability and vulnerability”. In: *Journal of Flood Risk Management* 2.4, pp. 230–231. DOI: <https://doi.org/10.1111/j.1753-318X.2009.01040.x> (cited on page 86).
- Singh, Deepti et al. (2013). “Precipitation extremes over the continental United States in a transient, high-resolution, ensemble climate model experiment”. In: *Jour-*

Journal of Geophysical Research: Atmospheres 118.13, pp. 7063–7086. DOI: <https://doi.org/10.1002/jgrd.50543> (cited on page 2).

Slingerland, Rudy and Norman D. Smith (2004). “River Avulsions and Their Deposits”. In: *Annual Review of Earth and Planetary Sciences* 32.1, pp. 257–285. DOI: 10.1146/annurev.earth.32.101802.120201 (cited on page 2).

Slotnick, Benjamin S. et al. (Sept. 2012). “Large Amplitude Variations in Carbon Cycling and Terrestrial Weathering during the Latest Paleocene and Earliest Eocene: The Record at Mead Stream, New Zealand”. In: *The Journal of Geology* 120.5, pp. 487–505. DOI: 10.1086/666743 (cited on pages 6, 11).

Smith, James A. et al. (Oct. 1, 2001). “Extreme Rainfall and Flooding from Supercell Thunderstorms”. In: *Journal of Hydrometeorology* 2.5, pp. 469–489. DOI: 10.1175/1525-7541(2001)002<0469:ERAFFS>2.0.CO;2 (cited on page 2).

Smith, James A. et al. (2018). “Strange Floods: The Upper Tail of Flood Peaks in the United States”. In: *Water Resources Research* 54.9, pp. 6510–6542. DOI: <https://doi.org/10.1029/2018WR022539> (cited on page 1).

Smith, Jon J. et al. (Sept. 29, 2009). “Transient dwarfism of soil fauna during the Paleocene–Eocene Thermal Maximum”. In: *Proceedings of the National Academy of Sciences*, pnas.0909674106. DOI: 10.1073/pnas.0909674106 (cited on page 12).

Stassen, Peter et al. (Feb. 1, 2012). “Perturbation of a Tethyan coastal environment during the Paleocene–Eocene thermal maximum in Tunisia (Sidi Nasseur and Wadi Mezaz)”. In: *Palaeogeography, Palaeoclimatology, Palaeoecology* 317–318, pp. 66–92. DOI: 10.1016/j.palaeo.2011.12.011 (cited on page 12).

Straub, Kyle M. and Brady Z. Foreman (Feb. 2, 2018). “Geomorphic stasis and spatiotemporal scales of stratigraphic completeness”. In: *Geology* 46.4, pp. 311–314. DOI: 10.1130/G40045.1 (cited on page 60).

Straub, Kyle M. et al. (Sept. 1, 2009). “Compensational Stacking of Channelized Sedimentary Deposits”. In: *Journal of Sedimentary Research* 79.9, pp. 673–688. DOI: 10.2110/jsr.2009.070 (cited on pages 31, 60).

Straub, Kyle M. et al. (June 1, 2012). “Prevalence of exponential bed thickness distributions in the stratigraphic record: Experiments and theory”. In: *Journal of Geophysical Research: Earth Surface* 117 (F2). DOI: 10.1029/2011JF002034 (cited on page 60).

Straub, Kyle M. et al. (2020). “Buffered, Incomplete, and Shredded: The Challenges of Reading an Imperfect Stratigraphic Record”. In: *Journal of Geophysical Research: Earth Surface* 125.3, e2019JF005079. DOI: 10.1029/2019JF005079 (cited on pages 5, 36).

- Strong, Nikki and Chris Paola (Aug. 1, 2008). “Valleys That Never Were: Time Surfaces Versus Stratigraphic Surfaces”. In: *Journal of Sedimentary Research* 78.8, pp. 579–593. DOI: 10.2110/jsr.2008.059 (cited on pages 32, 65).
- Thomas, E. and N. J. Shackleton (Jan. 1, 1996). “The Paleocene-Eocene benthic foraminiferal extinction and stable isotope anomalies”. In: *Geological Society, London, Special Publications* 101.1, pp. 401–441. DOI: 10.1144/GSL.SP.1996.101.01.20 (cited on page 11).
- Tipper, John C. (Jan. 1, 2015). “The importance of doing nothing: stasis in sedimentation systems and its stratigraphic effects”. In: *Geological Society, London, Special Publications* 404.1, pp. 105–122. DOI: 10.1144/SP404.6 (cited on page 5).
- Toby, Stephan C. et al. (2019). “A Stratigraphic Framework for the Preservation and Shredding of Environmental Signals”. In: *Geophysical Research Letters* 46.11, pp. 5837–5845. DOI: 10.1029/2019GL082555 (cited on page 61).
- Trampush, S. M., S. Huzurbazar, and B. McElroy (Dec. 2014). “Empirical assessment of theory for bankfull characteristics of alluvial channels”. In: *Water Resources Research* 50.12, pp. 9211–9220. DOI: 10.1002/2014WR015597 (cited on pages 4, 16, 19).
- Trampush, S. M. et al. (Jan. 1, 2017). “Identifying autogenic sedimentation in fluvial-deltaic stratigraphy: Evaluating the effect of outcrop-quality data on the compensation statistic”. In: *Journal of Geophysical Research: Earth Surface* 122.1, pp. 91–113. DOI: 10.1002/2016JF004067 (cited on page 4).
- Trampush, Sheila M. and Elizabeth A. Hajek (Nov. 1, 2017). “Preserving proxy records in dynamic landscapes: Modeling and examples from the Paleocene-Eocene Thermal Maximum”. In: *Geology* 45.11, pp. 967–970. DOI: 10.1130/G39367.1 (cited on pages 5, 8, 59–61).
- Trenberth, Kevin E. (Mar. 31, 2011). “Changes in precipitation with climate change”. In: *Climate Research* 47.1, pp. 123–138. DOI: 10.3354/cr00953 (cited on pages 1, 86).
- Trenberth, Kevin E. et al. (Sept. 1, 2003). “The Changing Character of Precipitation”. In: *Bulletin of the American Meteorological Society* 84.9, pp. 1205–1218. DOI: 10.1175/BAMS-84-9-1205 (cited on page 2).
- Van De Lageweg, W. I., W. M. Van Dijk, and M. G. Kleinmans (Nov. 1, 2013). “Morphological and Stratigraphical Signature of Floods In A Braided Gravel-Bed River Revealed From Flume Experiments Morphological and Stratigraphical Signature of Floods in A Braided River”. In: *Journal of Sedimentary Research* 83.11, pp. 1033–1046. DOI: 10.2110/jsr.2013.70 (cited on page 28).

- Venables, W. N. and Brian D. Ripley (2002). *Modern applied statistics with S*. 4th ed. Statistics and computing. New York: Springer. 495 pp. (cited on page 35).
- Wang, Bin and Qinghua Ding (2006). “Changes in global monsoon precipitation over the past 56 years”. In: *Geophysical Research Letters* 33.6. DOI: <https://doi.org/10.1029/2005GL025347> (cited on page 2).
- Westerhold, Thomas et al. (Oct. 15, 2009). “Latest on the absolute age of the Paleocene–Eocene Thermal Maximum (PETM): New insights from exact stratigraphic position of key ash layers +19 and -17”. In: *Earth and Planetary Science Letters* 287.3, pp. 412–419. DOI: 10.1016/j.epsl.2009.08.027 (cited on page 60).
- Wickert, Andrew D. et al. (2013). “River channel lateral mobility: metrics, time scales, and controls”. In: *Journal of Geophysical Research: Earth Surface* 118.2, pp. 396–412 (cited on pages 34, 35).
- Wing, Scott L. and Ellen D. Currano (July 1, 2013). “Plant response to a global greenhouse event 56 million years ago”. In: *American Journal of Botany* 100.7, pp. 1234–1254. DOI: 10.3732/ajb.1200554 (cited on pages 12, 15).
- Wolman, M. Gordon and John P. Miller (1960). “Magnitude and frequency of forces in geomorphic processes”. In: *The Journal of Geology* 68.1, pp. 54–74 (cited on pages 3, 25).
- Zachos, James et al. (2001). “Trends, rhythms, and aberrations in global climate 65 Ma to present”. In: *Science* 292.5517, pp. 686–693 (cited on pages 4, 11, 12).
- Zachos, James C., Gerald R. Dickens, and Richard E. Zeebe (Jan. 17, 2008). “An early Cenozoic perspective on greenhouse warming and carbon-cycle dynamics”. In: *Nature* 451.7176, pp. 279–283. DOI: 10.1038/nature06588 (cited on pages 5, 11).
- Zachos, James C. et al. (Mar. 1, 1993). “Abrupt Climate Change and Transient Climates during the Paleogene: A Marine Perspective”. In: *The Journal of Geology* 101.2, pp. 191–213. DOI: 10.1086/648216 (cited on page 5).

Appendix A

Statistical Models

A.1 Flooding in the Stratigraphic Record

A.1.1 Kruskal-Wallis test

To evaluate whether flow depth, bed material grain size, and paleoslope differed between the PETM and the surrounding units, a nonparametric test was chosen because values for these data are not normally distributed (Figure 2.3). 114 new observations of flow depth were combined with 137 previously-published estimates of flow depth from the Piceance Basin (Foreman et al. 2012) for a total of 251. A total of 107 grain size samples were taken, one from each set of outcrops. In this way, there are often multiple flow depth measurements for every bed material grain size measurement. To calculate paleoslopes using Equation 2.1, the average depth and grain size for each *set* of outcrops were combined to produce 54 unique estimates of slope. Each datum came from one of three stratigraphic formations, so each estimate (slope, depth, grain size) was tested using a Kruskal-Wallis rank test, where the test statistic is formulated as:

$$H = (N - 1) \frac{\sum_{i=1}^g n_i (\bar{r}_i - \bar{r})^2}{\sum_{i=1}^g \sum_{j=1}^{n_i} (r_{ij} - \bar{r})^2}, \quad (\text{A.1})$$

where N is the total number of observations, $g = 3$ is the number of formations, n_i is the number of observations in group i , r_{ij} is the rank of observation j in group i , \bar{r}_i is the average range for observations in group i , and \bar{r} is the average of all r_{ij} . The H statistic is compared to a critical value from the χ^2 distribution with $g - 1 = 2$ degrees of freedom (Kruskal and Wallis 1952). A significance level of $\alpha = 0.05$ was used to reject the null hypothesis that no group statistically dominates the others. In

each of these cases, the null hypothesis was not rejected (Table 2.1).

A.1.2 χ^2 test for proportions

In § 2.4 it is asserted that transitional avulsions were more frequent during the PETM as opposed to before and after, and that fluvial bars are less likely to be fully preserved during the PETM as opposed to before and after. To test this assertion, a Pearson's χ^2 test for proportions was conducted using tallies of transitional versus abrupt avulsions, and of fully- versus partially-preserved bars, comprising 141 observations of alluvial barforms from three exposures in the Piceance Basin, as well as 179 observations of avulsions gathered from a widely distributed area around the basin. In this case, the null hypothesis is that transitional avulsions and fully preserved bars will occur with equal frequency in the Atwell Gulch, Molina, and Shire members of the Wasatch formation. The χ^2 test statistic is formulated as:

$$\chi^2 = N \sum_{i=1}^n \frac{\frac{O_i}{N} - p_i}{p_i}, \quad (\text{A.2})$$

where N is the total number of observations, $g = 3$ is the number of formations, O_i is the number of observations in formation i , and p_i is the expected probability of that observation under the null hypothesis. The test statistic was compared to a χ^2 distribution with $g - 1 = 2$ degrees of freedom (Davis 2011). Both the test for transitional avulsions and the test for fully preserved bars rejected the null hypothesis at a 95% confidence level (Table 2.1).

A.2 Non-monotonic Fluvial Response to Changes in Flooding Intensity

A.2.1 Restricted maximum likelihood estimation for channel mobility

To quantify channel mobility, the exponential decay of normalized channel overlap was quantified, and estimates of the decay constant were interpreted in terms of an e -folding time (see § 3.2.3). To accomplish this, Equation 3.9 was fit using a non-linear least squares procedure for each level of flood intensity (k). That is, with a model specified as:

$$O_{\Phi i} = (a_M - p_M)e^{-Mt_i} + p_M + \varepsilon_i \quad (\text{A.3})$$

$$\varepsilon_i \sim N(0, \tau^2), \quad (\text{A.4})$$

where ε_i is a random normal deviate on observation i . The estimated parameters of this model are given below.

Table A.1: Estimated parameters for channel mobility

Flood Intensity	Parameter	Estimate	Standard Error
$Q_v = 1$	a_M	0.683	± 0.012
$Q_v = 1$	p_M	0.033	± 0.008
$Q_v = 1$	M	-0.05	± 0.002
$Q_v = 1$	τ	0.138	
$Q_v = 1.5$	a_M	0.476	± 0.012
$Q_v = 1.5$	p_M	0.116	± 0.008
$Q_v = 1.5$	M	-0.042	± 0.002
$Q_v = 1.5$	τ	0.161	
$Q_v = 3$	a_M	0.505	± 0.015
$Q_v = 3$	p_M	0.171	± 0.002
$Q_v = 3$	M	-0.218	± 0.007
$Q_v = 3$	τ	0.12	

A.2.2 Evaluating differences in sediment dispersal patterns

The relationship between averaging window, stratigraphic completeness, and the uniformity of sediment package thickness is described in § 3.2.4, using theoretical insights from Sadler (1981) and Jerolmack and Sadler (2018). Using measurements of stratigraphic completeness (f_c), at a range of discretization times (δt) for each level of flooding intensity (k), Equation 3.14 was fit as a mixed-effects linear model using MCMC methods with an uninformed prior and the following model specification:

$$f_{c\ i} = \alpha_{k(j)} \delta t_i^{\beta_{k(j)}} + \varepsilon_i, \quad (\text{A.5})$$

$$\alpha_{k(j)} \sim N(\mu_{\alpha(k)}, \sigma_{\alpha(k)}^2) \quad (\text{A.6})$$

$$\beta_{k(j)} \sim N(\mu_{\beta(k)}, \sigma_{\beta(k)}^2) \quad (\text{A.7})$$

$$\varepsilon_i \sim N(0, \tau^2), \quad (\text{A.8})$$

where ε_i is a random normal deviate on observation i . Completeness was evaluated at $j = 6$ radii spaced evenly from the delta apex, so to characterize the trend across the delta, the radius (r_j) was treated as a random effect on β and α . Posterior estimates of the absolute value of $\mu_{\beta\ k}$ were interpreted to determine the Sadler exponent. The posterior estimates of this model are summarized below in tabular form.

Table A.2: Posterior parameter estimates for Sadler exponent.

Parameter	Estimate	Standard Error
$\mu_\beta Q_v=1$	0.462	0.0244
$\mu_\beta Q_v=1.5$	0.507	0.0277
$\mu_\beta Q_v=3$	0.391	0.0388
$\sigma_\beta Q_v=1$	0.0515	0.0339
$\sigma_\beta Q_v=1.5$	0.0575	0.0384
$\sigma_\beta Q_v=3$	0.0735	0.0466
$\mu_\alpha Q_v=1$	0.151	0.0399
$\mu_\alpha Q_v=1.5$	0.147	0.041
$\mu_\alpha Q_v=3$	0.232	0.0645
$\sigma_\alpha Q_v=1$	0.151	0.0657
$\sigma_\alpha Q_v=1.5$	0.152	0.0765
$\sigma_\alpha Q_v=3$	0.167	0.0808
τ	0.165	8.8×10^{-4}

A.2.3 Evaluating differences in channel abundance in stratigraphy

Channel abundance, that is, the density of channel facies in the strata, is described in § 3.2.4, and shown in Figures 3.9 and 3.10. Using measurements of channel abundance ($f_{channel}$) for each level of flooding intensity (k), a fixed-effects ANOVA was fit using MCMC methods with an uninformed prior and the following model specification:

$$f_{channel\ i} = \alpha_{k(i)} + \varepsilon_i, \quad (\text{A.9})$$

$$\alpha_k \sim N(\mu_{\alpha(k)}, \sigma_{\alpha(k)}^2) \quad (\text{A.10})$$

$$\varepsilon_i \sim N(0, \tau^2), \quad (\text{A.11})$$

where ε_i is a random normal deviate on observation i , and posterior estimates of the values of $\mu_{\alpha(k)}$ were interpreted to determine differences in channel abundance between each flooding level. The posterior distributions of these parameters are summarized below in tabular form.

Table A.3: Posterior parameter estimates for channel abundance (non-dimensional).

Parameter	Estimate	Standard Error
$\mu_\alpha Q_v=1$	0.036	0.007
$\mu_\alpha Q_v=1.5$	0.032	0.006
$\mu_\alpha Q_v=3$	0.101	0.008
$\sigma_\alpha Q_v=1$	0.011	0.008
$\sigma_\alpha Q_v=1.5$	0.007	0.006
$\sigma_\alpha Q_v=3$	0.02	0.01
τ	0.021	0.003

A.2.4 Evaluating differences in floodplain relief

Floodplain roughness, calculated using the methods described in § 3.2.5, and illustrated in Figure 3.6. Using measurements of floodplain relief (\tilde{z}) at every run hour, for each level of flooding intensity (k), a fixed-effects ANOVA was fit using MCMC methods with an uninformed prior and the following model specification:

$$\tilde{z}_i = \alpha_{k(i)} + \varepsilon_i, \quad (\text{A.12})$$

$$\varepsilon_i \sim N(0, \tau^2), \quad (\text{A.13})$$

where ε_i is a random normal deviate on observation i , and posterior estimates of the values of α were interpreted to determine differences in floodplain relief between each flooding level. The posterior distributions of these parameters are summarized below in tabular form.

Table A.4: Posterior parameter estimates for floodplain relief (in mm).

Parameter	Estimate	Standard Error
$\alpha_{Q_v=1}$	4.87	0.545
$\alpha_{Q_v=1.5}$	7.47	2.86
$\alpha_{Q_v=3}$	4.83	2.59
τ	2.79	2.15

A.2.5 Evaluating differences in floodplain slope

Floodplain roughness, calculated using the methods described in § 3.2.5. Using measurements of floodplain slope ($\frac{dz}{dr}$) at every run hour, for each level of flooding intensity (k), a fixed-effects ANOVA was fit using MCMC methods with an uninformed prior and the following model specification:

$$\frac{dz}{dr}_i = \alpha_{k(i)} + \varepsilon_i, \quad (\text{A.14})$$

$$\varepsilon_i \sim N(0, \tau^2), \quad (\text{A.15})$$

where ε_i is a random normal deviate on observation i , and posterior estimates of the values of α were interpreted to determine differences in floodplain relief between each flooding level. The posterior distributions of these parameters are summarized below in tabular form.

Table A.5: Posterior parameter estimates for floodplain slope ($m/m \times 10^{-2}$).

Parameter	Estimate	Standard Error
$\alpha_{Q_v=1}$	2.92	0.0265
$\alpha_{Q_v=1.5}$	4.37	0.0585
$\alpha_{Q_v=3}$	3.67	0.0327
τ	1.07	0.0366

A.2.6 Evaluating differences in shoreline rugosity

Shoreline rugosity (R) was calculated using the methods described in § 3.2.5; Equation 3.15. Using measurements of shoreline rugosity at every run hour (i), for each level of flooding intensity (k), a fixed-effects one-way ANOVA was fit using MCMC

methods with an uninformed prior and the following model specification:

$$R_i = \alpha_{k(i)} + \varepsilon_i, \quad (\text{A.16})$$

$$\varepsilon_i \sim N(0, \tau^2), \quad (\text{A.17})$$

where ε_i is a random normal deviate on observation i , and posterior estimates of the values of α were interpreted to determine differences in shoreline rugosity between each flooding level. The posterior distributions of these parameters are summarized below in tabular form.

Table A.6: Posterior parameter estimates for shoreline rugosity (dimensionless).

Parameter	Estimate	Standard Error
$\alpha_{Q_v=1}$	0.18	0.00432
$\alpha_{Q_v=1.5}$	0.356	0.00441
$\alpha_{Q_v=3}$	0.137	0.00362
τ	0.0334	0.00216

A.2.7 Evaluating differences in channel width

Channel width (B) was calculated using the methods described in § 3.2.5, and illustrated in Figure 3.5. Using measurements of channel widths at every run hour, for each level of flooding intensity (k), a fixed-effects one-way ANOVA was fit using MCMC methods with an uninformed prior and the following model specification:

$$B_i = \alpha_{k(i)} + \varepsilon_i, \quad (\text{A.18})$$

$$\varepsilon_i \sim N(0, \tau^2), \quad (\text{A.19})$$

where ε_i is a random normal deviate on observation i , and posterior estimates of the values of α were interpreted to determine differences in channel width between each flooding level. The posterior distributions of these parameters are summarized below

in tabular form.

Table A.7: Posterior parameter estimates for channel width (in cm).

Parameter	Estimate	Standard Error
$\alpha_{Q_v=1}$	6.97	0.21
$\alpha_{Q_v=1.5}$	5.78	0.243
$\alpha_{Q_v=3}$	16.5	0.509
τ	3.28	0.126

A.2.8 Evaluating differences in channel depth

Channel depth (H) was calculated using the methods described in § 3.2.5, and illustrated in Figure 3.5. Using measurements of channel depths at every run hour, for each level of flooding intensity (k), a fixed-effects one-way ANOVA was fit using MCMC methods with an uninformed prior and the following model specification:

$$H_i = \alpha_{k(i)} + \varepsilon_i, \quad (\text{A.20})$$

$$\varepsilon_i \sim N(0, \tau^2), \quad (\text{A.21})$$

where ε_i is a random normal deviate on observation i , and posterior estimates of the values of α were interpreted to determine differences in channel depth between each flooding level. The posterior distributions of these parameters are summarized below in tabular form.

Table A.8: Posterior parameter estimates for channel depth (in mm).

Parameter	Estimate	Standard Error
$\alpha_{Q_v=1}$	10.4	0.26
$\alpha_{Q_v=1.5}$	12.5	0.402
$\alpha_{Q_v=3}$	8.89	0.283
τ	4.58	0.152

A.2.9 Evaluating differences in channel slope

Channel slope (S) was calculated using the methods described in § 3.2.5, and illustrated in Figure 3.5. Using measurements of channel depths at every run hour, for each level of flooding intensity (k), a fixed-effects one-way ANOVA was fit using MCMC methods with an uninformed prior and the following model specification:

$$S_i = \alpha_{k(i)} + \varepsilon_i, \quad (\text{A.22})$$

$$\varepsilon_i \sim N(0, \tau^2), \quad (\text{A.23})$$

where ε_i is a random normal deviate on observation i , and posterior estimates of the values of α were interpreted to determine differences in channel slope between each flooding level. The posterior distributions of these parameters are summarized below in tabular form.

Table A.9: Posterior parameter estimates for channel slope ($m/m \times 10^{-2}$).

Parameter	Estimate	Standard Error
$\alpha_{Q_v=1}$	2.66	0.014
$\alpha_{Q_v=1.5}$	1.83	0.013
$\alpha_{Q_v=3}$	2.69	0.011
τ	0.402	0.008

A.2.10 Evaluating differences in levee breach abundance

Levee breaches were identified in overhead images using the methods described in § 3.2.2, and illustrated in Figure 3.14. Using counts of levee breaches (C) at every run hour (i), for each level of flooding intensity (k), a fixed-effects one-way ANOVA was fit using MCMC methods with an uninformative prior and the following model

specification:

$$\log(\lambda_i) = \alpha_{k(i)} \quad (\text{A.24})$$

$$C_i \sim \text{Poisson}(\lambda_i), \quad (\text{A.25})$$

where λ_i is the Poisson mean, and posterior estimates of the values of e^{α_k} were interpreted to determine differences in the average number of levee breach between each flooding level. The posterior distributions of these parameters are summarized below in tabular form.

Table A.10: Posterior parameter estimates for levee breach abundance.

Parameter	Estimate	Standard Error
$e^{\alpha_{Q_v=1}}$	9.03	0.298
$e^{\alpha_{Q_v=1.5}}$	5.11	0.226
$e^{\alpha_{Q_v=3}}$	10.6	0.331

A.3 Paleoclimate Bias due to Transitions in Flooding

A.3.1 Evaluating bias in preserved transition duration

Preservation bias (T') was defined as the percent difference between the perceived event duration and the true event duration, described in § 4.2.3, and illustrated in Figure 4.2. Using measurements of T' for a set of 100 columns extracted from 4 circular sections with radius r_j through the synthetic stratigraphy for each level of flooding intensity (k), a mixed-effects one-way ANOVA was fit using MCMC methods

with an uninformed prior and the following model specification:

$$\log(T'_i + 1) = \alpha_{k(j)(i)} + \varepsilon_i, \quad (\text{A.26})$$

$$\alpha_{k(j)} \sim N(\mu_{\alpha(k)}, \sigma_{\alpha(k)}^2) \quad (\text{A.27})$$

$$\varepsilon_i \sim N(0, \tau^2), \quad (\text{A.28})$$

where ε_i is a random normal deviate on observation i , and posterior estimates of the values of $(e^\alpha - 1)$ were interpreted to determine differences in preservation bias between each flooding level. T' was translated and log-transformed because the data residuals are right-skewed and have a minimum possible value of -1. The posterior distributions of these parameters are summarized below in tabular form.

Table A.11: Posterior parameter estimates for preservation bias (dimensionless).

Transition	Parameter	Estimate	Standard Error
T_1^+	μ_α	0.1662188	0.2266888
T_1^+	σ_α	0.2907706	0.3987923
T_2^-	μ_α	-0.3977284	0.6612399
T_2^-	σ_α	3.3185332	3.374222
T_3^+	μ_α	0.1356474	1.1546591
T_3^+	σ_α	2.6567428	2.9310057
T_4^-	μ_α	-0.5866044	0.4430855
T_4^-	σ_α	2.23398	2.791491
T_5^+	μ_α	-0.4314864	0.4751559
T_5^+	σ_α	2.4780358	2.7453789
T_6^-	μ_α	-0.5040379	0.5805979
T_6^-	σ_α	2.2763896	2.7418336
T_7^+	μ_α	0.7266158	2.1744678
T_7^+	σ_α	1.5102971	2.2990009
	τ	1.0946148	0.0214806

A.3.2 Evaluating the average sediment accumulation rate during transitions

The average sediment accumulation rate (\dot{z}) was quantified for a random set of 100 stratigraphic columns extracted from each of 4 circular sections with radius r_j through the synthetic stratigraphy for each level of flooding intensity (k). A mixed-effects one-way ANOVA was fit using MCMC methods with an uninformed prior and the following model specification:

$$\dot{z}_i = \alpha_{k(j)(i)} + \varepsilon_i, \quad (\text{A.29})$$

$$\alpha_{k(j)} \sim N(\mu_{\alpha(k)}, \sigma_{\alpha(k)}^2) \quad (\text{A.30})$$

$$\varepsilon_i \sim N(0, \tau^2), \quad (\text{A.31})$$

where ε_i is a random normal deviate on observation i , and posterior estimates of the values of μ_{α} were interpreted to determine differences in average sediment accumulation rate between each flooding level. The posterior distributions of these parameters are summarized below in tabular form.

Table A.12: Posterior parameter estimates for average sediment accumulation rate (mm/hr).

Transition	Parameter	Estimate	Standard Error
T_1^+	μ_α	0.2852924	0.0478166
T_1^+	σ_α	0.0670672	0.0653351
T_2^-	μ_α	0.1091533	0.0952096
T_2^-	σ_α	0.1060489	0.1510905
T_3^+	μ_α	0.3474249	0.2919885
T_3^+	σ_α	0.4111249	0.4115844
T_4^-	μ_α	0.1037821	0.0678216
T_4^-	σ_α	0.0858945	0.0923503
T_5^+	μ_α	0.0490444	0.0333383
T_5^+	σ_α	0.0388293	0.0429609
T_6^-	μ_α	0.1215035	0.0313934
T_6^-	σ_α	0.0322284	0.0423028
T_7^+	μ_α	0.3923887	0.1556869
T_7^+	σ_α	0.2182185	0.2262839
	τ	0.231233	0.0045178

A.3.3 Evaluating the variability in sediment accumulation rate during transitions

The standard deviation of sediment accumulation rate (σ_z) was quantified for a random set of 100 stratigraphic columns extracted from each of 4 circular sections with radius r_j through the synthetic stratigraphy for each level of flooding intensity (k), a mixed-effects one-way ANOVA was fit using MCMC methods with an uninformed prior and the following model specification:

$$\sigma_z \ i = \alpha_{k(j)(i)} + \varepsilon_i, \quad (\text{A.32})$$

$$\alpha_{k(j)} \sim N(\mu_{\alpha(k)}, \sigma_{\alpha(k)}^2) \quad (\text{A.33})$$

$$\varepsilon_i \sim N(0, \tau^2), \quad (\text{A.34})$$

where ε_i is a random normal deviate on observation i , and posterior estimates of the values of μ_α were interpreted to determine differences in the standard deviation of

sediment accumulation rate between each flooding level. The posterior distributions of these parameters are summarized below in tabular form.

Table A.13: Posterior parameter estimates for the standard deviation of sediment accumulation rate (mm/hr).

Transition	Parameter	Estimate	Standard Error
T_1^+	μ_α	0.9297098	0.1374328
T_1^+	σ_α	0.1845825	0.2310501
T_2^-	μ_α	0.6698967	0.4408793
T_2^-	σ_α	0.556465	0.6205837
T_3^+	μ_α	0.9082161	0.160175
T_3^+	σ_α	0.2142157	0.216208
T_4^-	μ_α	0.5359364	0.1604378
T_4^-	σ_α	0.2094044	0.221776
T_5^+	μ_α	0.5123357	0.118453
T_5^+	σ_α	0.1565556	0.158084
T_6^-	μ_α	0.6904289	0.1605859
T_6^-	σ_α	0.2067585	0.2437022
T_7^+	μ_α	0.8194117	0.4234036
T_7^+	σ_α	0.5097912	0.6072287
	τ	0.53535	0.0108237

A.3.4 Evaluating the impact of sedimentation rate and steadiness on preservation bias

Preservation bias (T') trends with mean sedimentation rate during transitions (Figure 4.7). To test this relationship and evaluate the relative importance of the mean sedimentation rate versus its temporal variability, a mixed-effects ANCOVA was fit using MCMC methods with an uninformative prior, and the following model specifi-

cation:

$$T'_i = \beta_0 k^{(j)(i)} + \beta_1 k^{(j)(i)} \frac{dz}{dt} + \beta_2 k^{(j)(i)} \sigma \frac{dz}{dt} + \varepsilon_i, \quad (\text{A.35})$$

$$\alpha_{k^{(j)}} \sim N(\mu_{\alpha^{(k)}}, \sigma_{\alpha^{(k)}}^2) \quad (\text{A.36})$$

$$\varepsilon_i \sim N(0, \tau^2), \quad (\text{A.37})$$

where ε_i is a random normal deviate on observation i , and posterior estimates of the values of μ_{β_1} and μ_{β_2} were interpreted to determine differences in the dependence of the preservation bias on the mean sediment accumulation rate versus the temporal variability. As before, since columns were taken from $j = 4$ circular sections from the apex with radius r_j , radius is treated as a random effect.

The posterior distributions of these parameters are summarized below in tabular form.

Table A.14: Posterior parameter estimates for the influence of \dot{z} and $\sigma_{\dot{z}}$ on T' .

Transition	Parameter	Estimate	Standard Error
T_1^+	μ_{β_0}	-0.9565611	0.3366992
T_1^+	σ_{β_0}	7.5030754	4.3103485
T_1^+	μ_{β_1}	4.0821563	1.1758056
T_1^+	σ_{β_1}	7.4974326	4.3561111
T_1^+	μ_{β_2}	0.0858451	0.2950316
T_1^+	σ_{β_2}	7.5928191	4.2779287
T_2^-	μ_{β_0}	-0.4980312	0.1507681
T_2^-	σ_{β_0}	7.2889025	4.2970682
T_2^-	μ_{β_1}	1.3273231	0.6191423
T_2^-	σ_{β_1}	7.536838	4.3561666
T_2^-	μ_{β_2}	0.4652891	0.1696808
T_2^-	σ_{β_2}	7.5714047	4.3329614
T_3^+	μ_{β_0}	-0.8187876	0.221492
T_3^+	σ_{β_0}	7.4394871	4.3025846
T_3^+	μ_{β_1}	1.7312328	0.4147387
T_3^+	σ_{β_1}	7.6046504	4.3316793
T_3^+	μ_{β_2}	0.6212444	0.2669847
T_3^+	σ_{β_2}	7.44215	4.3610539
T_4^-	μ_{β_0}	-0.876776	0.2531072
T_4^-	σ_{β_0}	7.4040169	4.3114661
T_4^-	μ_{β_1}	2.4442268	0.9225951
T_4^-	σ_{β_1}	7.4799638	4.3403092
T_4^-	μ_{β_2}	0.6521291	0.5004102
T_4^-	σ_{β_2}	7.4870495	4.3305514
T_5^+	μ_{β_0}	-0.9928959	0.2130511
T_5^+	σ_{β_0}	7.4878591	4.3986413
T_5^+	μ_{β_1}	1.5012324	0.7575098
T_5^+	σ_{β_1}	7.5074451	4.2970672
T_5^+	μ_{β_2}	1.8858158	0.3855177
T_5^+	σ_{β_2}	7.5276659	4.3134271
T_6^-	μ_{β_0}	-0.2336846	0.1487343
T_6^-	σ_{β_0}	7.4911646	4.3756286
T_6^-	μ_{β_1}	0.7856335	0.4493008
T_6^-	σ_{β_1}	7.3752397	4.3788749
T_6^-	μ_{β_2}	0.9721134	0.1579422
T_6^-	σ_{β_2}	7.4868341	4.2882955
T_7^+	μ_{β_0}	0.3517287	0.1823277
T_7^+	σ_{β_0}	7.4639861	4.3460888
T_7^+	μ_{β_1}	2.2862686	0.4377769
T_7^+	σ_{β_1}	7.5218376	4.3135232
T_7^+	μ_{β_2}	-0.3504849	0.2516574
T_7^+	σ_{β_2}	7.4833048	4.3572874
	τ	1.4808621	0.029609